AD-A033 946 AUSTIN RESEARCH ASSOCIATES INC TEX F/G 20/7
CONCEPTUAL DESIGN OF AN AUTO-RESONANT ACCELERATOR EXPERIMENT.(U)
NOV 76 W E DRUMMOND, G I BOURIANOFF F29601-76-C-0046
UNCLASSIFIED ARA-224 AFWL-TR-76-152 NL

1 OF 4
AD
A033946

AFWL-TR-76-152

AFWL-TR-76-152

ADA033946

CONCEPTUAL DESIGN OF AN AUTO-RESONANT ACCELERATOR EXPERIMENT

Austin Research Associates, Inc.
Austin, TX 78758

November 1976

Final Report

Approved for public release; distribution unlimited.

JAN 3 1977
B

Prepared for
ADVANCED RESEARCH PROJECTS AGENCY
1400 Wilson Boulevard
Arlington, VA 22209

AIR FORCE WEAPONS LABORATORY
Air Force Systems Command
Kirtland Air Force Base, NM 87117

AFWL-TR-76-152

This final report was prepared by Austin Research Associates, Inc., Austin, Texas, under Contract F29601-75-C-0046, Job Order 28720401 with the Air Force Weapons Laboratory, Kirtland Air Force Base, New Mexico. Captain R. B. Miller (DYS) was the Laboratory Project Officer-in-Charge.

When US Government drawings, specifications, or other data are used for any purpose other than a definitely related Government procurement operation, the Government thereby incurs no responsibility nor any obligation whatsoever, and the fact that the Government may have formulated, furnished, or in any way supplied the said drawings, specifications, or other data is not to be regarded by implication or otherwise as in any manner licensing the holder or any other person or corporation or conveying any rights or permission to manufacture, use, or sell any patented invention that may in any way be related thereto.

This report has been reviewed by the Information Office (OI) and is releasable to the National Technical Information Service (NTIS). At NTIS, it will be available to the general public, including foreign nations.

This technical report has been reviewed and is approved for publication.

Robert B. Miller

R. B. MILLER
Captain, USAF
Project Officer

FOR THE COMMANDER

THOMAS C. MAY
Major, USAF
Chief, Advanced Concepts Research Branch

JOHN S. DEWITT
LtColonel, USAF
Chief, Technology Division

DO NOT RETURN THIS COPY. RETAIN OR DESTROY.

UNCLASSIFIED

SECURITY CLASSIFICATION OF THIS PAGE (When Data Entered)

REPORT DOCUMENTATION PAGE	READ INSTRUCTIONS BEFORE COMPLETING FORM
1. REPORT NUMBER: AFWL-TR-76-152	2. GOVT ACCESSION NO. / 3. RECIPIENT'S CATALOG NUMBER
4. TITLE (and Subtitle): CONCEPTUAL DESIGN OF AN AUTO-RESONANT ACCELERATOR EXPERIMENT.	5. TYPE OF REPORT & PERIOD COVERED: Final Report.
	6. PERFORMING ORG. REPORT NUMBER: 1-ARA-76-U-44; ARA-224
7. AUTHOR(s): William E. Drummond, George I. Bourianoff, Edward P. Cornet, David E. Hasti, William W. Rienstra, M. Lee Sloan, James R. Thompson, John R. Ugtum, and H. Vernon Wong	8. CONTRACT OR GRANT NUMBER(s): F29601-76-C-0046
9. PERFORMING ORGANIZATION NAME AND ADDRESS: Austin Research Associates, Inc. Austin, TX 78705	10. PROGRAM ELEMENT, PROJECT, TASK AREA & WORK UNIT NUMBERS: 62301E 28720401
11. CONTROLLING OFFICE NAME AND ADDRESS: Defense Advanced Research Projects Agency (ARPA) Arlington, VA 22209	12. REPORT DATE: November 1976
	13. NUMBER OF PAGES: 306
14. MONITORING AGENCY NAME & ADDRESS (if different from Controlling Office): The Air Force Weapons Laboratory Kirtland AFB, NM 87117	15. SECURITY CLASS. (of this report): UNCLASSIFIED
	15a. DECLASSIFICATION/DOWNGRADING SCHEDULE

16. DISTRIBUTION STATEMENT (of this Report)

Approved for public release; unlimited distribution.

ARA-224, I-ARA-76-U-44

17. DISTRIBUTION STATEMENT (of the abstract entered in Block 20, if different from Report)

18. SUPPLEMENTARY NOTES

19. KEY WORDS (Continue on reverse side if necessary and identify by block number)

Auto-Resonant Accelerator	Collective Acceleration	Accelerator
Relativistic Electron Beam	Cyclotron Wavegrowth	Instability
Relativistic Cyclotron Mode	Negative Energy Wave	Kink Modes
Stability of Acceleration	Magnetic Field	Ion Injection

20. ABSTRACT (Continue on reverse side if necessary and identify by block number)

Conceptual design and specifications for a proof-of-principal Auto-Resonant Accelerator have been undertaken. In particular, the pulse power source and diode configuration, the diode to waveguide transition and compression sections, magnetic field characteristics, phase locking and wavegrowth requirements, and the method of ion loading and acceleration have been examined. Specifications and conceptual designs for these five areas are presented along with several considerations of overall system requirements.

DD FORM 1 JAN 73 1473 EDITION OF 1 NOV 65 IS OBSOLETE

UNCLASSIFIED

SECURITY CLASSIFICATION OF THIS PAGE (When Data Entered)

403703 LB

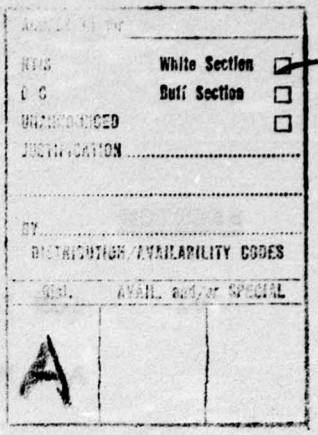

TABLE OF CONTENTS

SECTION		Page
I	INTRODUCTION.	1
II	POWER SOURCE AND DIODE.	5
	A. Pulsed Power System	5
	B. Diode Considerations.	7
III	ELECTRON BEAM CONSIDERATIONS.	9
	A. Transition Section and Beam Compression.	9
	B. Electron Beam Characterization. . . .	10
IV	MAGNETIC GUIDE FIELD CONSIDERATIONS . . .	12
V	CYCLOTRON WAVE GROWTH	14
	A. RF Exciter.	14
	B. Wave Growth Configuration	15
	C. Detailed Energy Balance	17
	D. Wave Growth Saturation and Other Nonlinear Effects	18
	E. Wave Growth Diagnostics	22

SECTION		Page
VI	ION LOADING AND ACCELERATION	25
	A. Methods of Ion Loading	25
	B. Stability of Acceleration	27
	C. Ion Diagnostics	29
VII	OVERALL SYSTEMS CONSIDERATIONS	31
	A. Operational Control System	32
	B. Waveguide Vacuum Requirements	35
	C. Beam Dump and Radiation Shielding	36

APPENDIXES

A	ELECTRON BEAM INJECTOR CONSIDERATIONS	39
B	THE EFFECTS OF VOLTAGE DROOP AND LOW FREQUENCY RIPPLE ON ACCELERATOR PHASE STABILITY	46
C	ANODE SURVIVAL SPECIFICATION	50
D	DIODE DIAGNOSTICS	53
E	TRANSITION TO BEAM EQUILIBRIUM REGION	62
F	BEAM COMPRESSION	72
G	ELECTRON BEAM DIAGNOSTICS	78

APPENDIXES

		Page
H	MAGNET DESIGN CONSIDERATIONS	81
I	NUMERICAL INVESTIGATION OF MAGNETIC GUIDE FIELD PROFILES	86
J	ESTIMATE OF MAGNETIC FIELD RIPPLE	114
K	COUPLING TO THE RELATIVISTIC CYCLOTRON EIGENMODE THROUGH AN EXTERNAL AZIMUTHAL CURRENT LOOP	120
L	SOLUTIONS TO SHEATH HELIX DISPERSION RELATION FOR m = 0, 1.	130
M	SUPPRESSION OF THE m = 1 HYDRODYNAMIC INSTABILITY FOR THE SHEATH HELIX GROWTH SECTION	148
N	TAPE HELIX DISPERSION RELATION.	152
O	A MODIFIED RESISTIVE GROWTH MECHANISM USING DISCRETE LOOP DRIVES	170
P	DETAILS OF WAVE ENERGY BALANCE IN THE AUTO-RESONANT ACCELERATOR.	184
Q	NONLINEAR FREQUENCY SHIFT OF BEAM CYCLOTRON MODE	193
R	NONLINEAR EFFECTS FOR THE ELECTRON BEAM CYCLOTRON MODE.	214
S	COMPUTER SIMULATION OF THE RESISTIVE GROWTH AND SATURATION OF THE ELECTRON CYCLOTRON MODE.	231

APPENDIXES

		Page
T	GROWTH OF THE CYCLOTRON WAVE BY AN ANISOTROPIC RESISTIVE BACKGROUND.	249
U	A MODEL OF ION PICKUP AND ACCELERATION BY A TRAVELLING WAVE.	262
V	VACUUM REQUIREMENTS	289
W	BEAM DUMP AND RADIATION SHIELDING	291

LIST OF ILLUSTRATIONS

FIGURE		Page
1	Accelerator Operation Flow Chart.	33
D-1	Diode Diagnostic Configuration.	54
D-2	Calibration System for Diode Voltage Monitor and Current Shunt	56
D-3	In SITU Calibration of Diode Voltage Monitor	59
I-1	Guide Field in Kilogauss vs. Distance in Centimeters.	100
I-2	Qualitative Plot of Patched Guide Field . .	104
K-1	Variation of Inductance (K) and Potential Ratio (ϵ) with Loop Radius.	130
L-1	Phase Velocity of Modes 0, 1 vs. Tan θ for $\Omega a/c = 1$ and $\omega_p^2 a^2/c^2 = 0.1$	143
L-2	Growth Rates of Modes 0, 1 vs. Tan θ for $\Omega a/c = 1$ and $\omega_p^2 a^2/c^2 = 0.1$	144
N-1	Geometry of Tape Helix.	154
S-1	E_x vs. x at $\tau = 3200$	237
S-2	E_x Energy vs. t	238
S-3	E_x Energy vs. Time-Run 1	241
S-4	Total Energy vs. Time	245

FIGURE		Page
S-5	E_x Energy vs. Time-Run 2	246
U-1	Potential Function of Accelerating Wave. .	267
U-2	Pickup Efficiency in a Nonaccelerating Wave	276
U-3	Adiabatic Growth and Acceleration with 100% Trapping Efficiency	285
U-4	Wave Acceleration at Constant Field Amplitude.	287

LIST OF TABLES

TABLE		Page
B-1	THE EFFECTS OF VOLTAGE DROOP AND LOW FREQUENCY RIPPLE ON ACCELERATOR PHASE STABILITY	49
I-1	LISTING OF PROGRAM BSTAB	93
I-2	CONSTANT PHASE RUN	96
I-3	FIELD RIPPLE RUNS	101
I-4	FIELD PATCHING RUN	105
I-5	FIELD PATCHING RUN	109

SECTION I

INTRODUCTION

Detailed theoretical investigation of the principle of Auto-Resonant acceleration has proceeded to the point where a detailed experimental test of this accelerator concept can be formulated. Such an experiment would have three fundamental goals:

1. Examine and verify the basic concept of Auto-Resonant acceleration.
2. Explore the nonlinear limits of operation of such an accelerator.
3. Establish the proper scaling laws of such a device to higher output values of ion current and energy.

A conceptual experiment to undertake these tasks has been devised under the following basic guidelines: First, in order to minimize technological problem areas

not directly associated with the physics of the experiment, we require that the electron beam power source be of a standard, state-of-the-art type not requiring new technological innovations, that magnetic guide fields be of reasonable values easily achievable in the laboratory, that total accelerator length be held within reasonable bounds, and that frequencies and wavelengths associated with phenomena of interest lie in a regime of easy experimental access. At the same time, the ion output energy level should be sufficiently high to discriminate against other types of collective acceleration processes. Finally, ion output current should be sufficiently flexible to allow examination of nonlinear saturation phenomena.

Using these basic guidelines and the parameter survey code developed earlier [Appendix Z, Reference 1 (Reference written as Ref. herafter)], the following accelerator parameters were selected:

---

1. W. E. Drummond, et al., "A Theoretical Investigation of the Principle of Auto-Resonant Acceleration," AFWL-TR-75-296, Air Force Weapons Laboratory, Air Force Systems Command, Kirtland Air Force Base, N.M., Nov. 1975.

Electron beam energy	3 MeV
Electron beam current	30 kA
Minimum e-beam pulse time	100 ns
Nominal ion output energy	30 MeV
Nominal ion output current	30 A
Maximum magnetic field	24 kG
Minimum magnetic field	2 kG
Wave Growth Section Length	5 m
Accelerator Length	4 m
RF liner frequency	240 MHz

In this accelerator, the relativistic e-beam is injected into the vacuum waveguide from a 3 cm radius, conventional foil diode configuration immersed in a 2.4 kG magnetic field. Following a roughly 30 cm transition region, where beam equilibrium is established, the beam is compressed in a 1 m long compression section to a 1 cm radius with a 24 kG to 2 kG magnetic field at the output.

In this technical report, the details of the conceptual design criteria and specifications for such an accelerator are presented. The requirements for the

electron beam power source and diode are discussed in Section II, with specifications and diagnostics for the propagating electron beam given in Section III. Section IV contains details of the magnetic field system and configuration. In Section V, various wave growth schemes are examined, with ion loading and acceleration discussed in Section VI. Some overall system requirements are given in Section VII.

SECTION II

POWER SOURCE AND DIODE

The nominal electron beam parameters required for a prototype Auto-Resonant Accelerator are described in the preceding section. The pulsed power system needed to produce this beam, as well as the diode itself and its associated diagnostics, is described below.

A. Pulsed Power System

Specifications for the pulsed power system are detailed in Appendix A and listed below for completeness.

Electron Injector Specification

1. Load: 100 Ω (constant impedance dummy load for tests)
2. Peak voltage (V_{pk}) into 100 Ω: 3 MeV
3. Duration: 200 ns minimum useful pulse between 0.96 V_{pk} points (± 2%)
4. Reproducibility of V_{pk} shot to shot: ± 2%
5. Rise time: ≤ 100 ns (5% to 95% of V_{pk})

6. Prepulse suppression: Maximum prepulse less than 3 % of V_{pk} (measured with no dummy load)

7. Ripple: Less than ± 1/2% high frequency ($\geq$ 10 MHz) ripple during useful pulse ($V \geq 0.96\ V_{pk}$)

8. Triggering: Command triggered with less than ± 200 ns jitter between triggering and firing

9. Pulse clipping crowbar switch to reduce energy into 100 Ω load to less than 10% of initial stored energy after 200 ns useful pulse (0 to + 50 ns jitter allowed in crowbar switch)

10. The electrical circuit driving the load should have a low internal impedance.

The voltage and current requirements (3 MeV, 30 kA) needed in the electron beam are well within the range of conventional technology, although the duration of the flat-top portion of the voltage pulse (200 ns) is longer than normally used in flash X-ray machines. However, it is certainly attainable with conventional techniques.

These specifications were submitted to two major manufacturers of pulsed power systems. Both groups

submitted machine configurations which could meet the pulsed power requirements. To confirm the suitability of each design, in particular the ripple specifications, computer generated digital voltage waveforms were submitted to Austin Research Associates by both manufacturers. These waveforms were modelled with a numerical code to study the phase stability of the Auto-Resonant Accelerator. The details of this study can be found in Appendix B. The results of this study show that both the droop and ripple from either machine were "safe" by at least a factor of 2. Thus, it appears possible to obtain a pulsed power system suitable for studying a prototype accelerator.

B. Diode Considerations

Realization of the uniform beam required for the accelerator is most easily attained using a conventional cold cathode/thin foil anode diode. Foil survival then becomes an important consideration. Detailed calculations in Appendix C show that an A-K gap spacing of about 3 cm, with a corresponding current density of 1 kA/cm^2, will ensure long anode lifetime. The large gap spacing also minimizes the diode impedance collapse due to plasma closure.

As indicated in Appendix A, final diode design will be done using a computer code. However, theoretical efforts need to be carried out to give an initial guess at the cathode shape. Initial calculations indicate that a flat cathode will cause beam pinching in the diode. To attain rectilinear flow, the diode gap spacing would have to scale as

$$d \sim e^{r^2/r_o^2}$$

where r_o is an appropriate scale length.

Such a cathode shape would likely generate a Gaussian-like current density profile. This is undesirable, and further efforts need to be given to this problem.

To characterize the beam energy and total current, the diagnostics described in Appendix D can be utilized. The capacitive voltage monitor and return current shunt are proven techniques which have a frequency response more than adequate to measure high frequency components. Gross beam characterization poses no technical problem.

SECTION III

ELECTRON BEAM CONSIDERATIONS

Once formed in the diode, the electron beam is injected into the drift tube (waveguide) section. Since the resulting 3 cm radius beam is too large for the wave growth section (a 1 cm radius is required for a manageable wave growth section length), beam compression is necessary once an equilibrium beam configuration is established. In this section, these details are considered along with techniques for measuring the beam parameters.

A. Transition Section and Beam Compression

After entering the drift tube, the beam must propagate one or two beam diameters down the tube before end effects introduced by the anode can be ignored. After this distance, a low angular rotation rigid rotor equilibrium is established. The details of these considerations can be found in Appendix E. Attainment of the desired equilibrium is intimately connected with the diode design.

More detailed work in the area is indicated to ensure transition to the appropriate equilibrium.

After an equilibrium is established, the beam must be compressed to a cross-sectional size compatible with keeping the cyclotron wave growth section length to a tractable size. The compression should be carried out over a long enough distance to minimize beam heating (introducing transverse temperature). Appendix F develops the theory of beam compression, and gives a formula for numerically calculating the amount of heating introduced by a given compression section. Initial estimates assuming an adiabatic compression indicate the amount of transverse energy to be roughly 1% of the total energy. This is sufficiently small to preclude Landau damping of the desired cyclotron wave.

B. Electron Beam Characterization

The diagnostics which would be used to characterize the electron beam at the anode and in the beam transition region are described in Appendix G. The types of measurements--calorimetry, Faraday cups, magnetic loops,

etc.--are standard. Also, X-ray techniques can provide a great deal of information on gross angular spreading of the electron beam.

SECTION IV

MAGNETIC GUIDE FIELD CONSIDERATIONS

The magnetic guide field is necessary for confining the electron beam and controlling the phase velocity of the cyclotron wave. This guide field is to be generated by a series of solenoidal windings driven by a low voltage capacitor bank. The ring-up time of the capacitor-field coil circuit should be long compared to the magnetic diffusion time through the vacuum waveguide, and the flat-top portion of the field pulse should be long compared to the 100 to 200 ns pulse length of the electron beam. A detailed discussion of the relationship of the capacitor bank-field coil parameters (Q, capacitance, resistance, field coil size and spacing) is given in Appendix H.

In the accelerator section the guide field must decrease down the length of the accelerator in order to accelerate the ions. In Ref. 1, analytical calculation showed that spatial ripple on the guide field due to discrete current loops could "detrap" the ions from the potential wells if this ripple is too severe. In Appendix

I, the results of a computer code which integrates the relativistic, one dimensional ion equation of motion are given for acceleration of ions to the 25 to 30 MeV energy range. There it is shown that stable acceleration results if the spatial ripple is kept below 5%.

In Appendix J an analytical estimate of the ripple to be expected from physically realizable coils is given. These calculations show that the ripple may be kept below 1% so that, with careful field coil design, ripple should present no problem.

An unfortunate property of the guide field which produces the shortest acceleration length for a given final energy is that it is nonadiabatic $\left(\left| \frac{c}{\Omega^2} \frac{d\Omega}{dz} \right| \sim 1 \right)$ for the first few centimeters. The effects of replacing this nonadiabatic section with an adiabatic section have been investigated. It is shown in Appendix I that this patching may be done in a phase stable way which adds only about 30 cm to the length of the accelerator section (~ 4 m).

SECTION V

CYCLOTRON WAVE GROWTH

The cyclotron wave growth section is one of the most critical components of the accelerator experiment. Here the correct negative energy cyclotron mode must be properly excited and phase locked, and then grown to the appropriate amplitude. Care must be taken so that non-axisymmetric modes are not grown to disruptive amplitudes and that nonlinear saturation phenomena do not limit the amplitude of the axisymmetric wave below that desired.

A. RF Exciter

The method of exciting and phase locking the desired cyclotron wave has been examined. It appears that a current loop drive will efficiently couple to the desired cyclotron mode if located at 0.7 to 0.8 of the wall radius, as indicated in Appendix K. Location of the loop too close to the wall results in an undesirable drop in loop impedance due to the induced shorting currents in the wall.

This method of excitation should result in a fairly pure axisymmetric standing cyclotron wave (equal mix of positive and negative energy contributions) with small nonaxisymmetric components. Subsequent growth sections will amplify the negative energy component and damp the positive energy component.

B. Wave Growth Configuration

A continuing examination of passive external liner configurations capable of growing the negative energy cyclotron wave has been maintained.

A generally accepted method reported previously (Ref. 1) is through use of a resistive liner configuration with azimuthal shorting rings. This edge ring liner has the disadvantage of fairly long growth lengths (which necessitates the 5 meter growth section in the conceptual experimental design) and attendant kink instabilities, which one must take care to avoid.

Continuing work on the use of helical slow wave structures indicates that these disadvantages may be overcome. The first helical structure examined, the sheath

helix configuration, yields very short growth lengths (~15 cm for the model accelerator parameters given in Section I); but, unfortunately, a detailed examination of this structure over a broad range of operating parameters shows that the m = 1 kink mode always grows at least slightly faster than the desired axisymmetric mode. As such, such a structure could be utilized only if the axisymmetric mode were sufficiently preferentially excited. This analysis is presented in Appendix L.

In Appendix M, a sufficient condition is derived for the suppression of the fast kinking instability of the sheath helix; namely, $\omega_p^2 < \Omega^2$, where ω_p, Ω are the relativistic plasma and cyclotron frequency of the beam, respectively.

A second helical structure, the so-called tape helix, appears to retain the good growth features of the sheath helix for the axisymmetric mode, while allowing the growth rate for the m = 1 mode to be reduced. This arises from the fact that in the tape helix, the finite spacings between the windings give rise to stop band characteristics. By locating the frequency and wavelength of the

nonaxisymmetric mode near these stop band regions, a reduction in growth rate appears feasible. Details of this analysis are given in Appendix N.

A fourth interesting wave growth configuration utilizes discrete azimuthal current loops connected to external passive RC networks. By choosing the value of C (capacitance) so that the networks are resonant with the loop inductance at the driving frequency of 240 MHz, very small growth lengths for the axisymmetric mode can be obtained. Furthermore, it appears (although it has not been conclusively shown) that the m = 1 kink modes can be suppressed by bringing the walls of the waveguide sufficiently close to the driving loops. (If the walls are brought too close, the waveguide must be slotted longitudinally to prevent shorting of the loops.) A discussion of this method of wave growth and some of the attendant problems is given in Appendix N.

C. Detailed Energy Balance

Of considerable importance in determining total energetics in the Auto-Resonant Accelerator concept is an

understanding of the detailed exchange of energy during the growth of the wave. This question is examined in detail in Appendix P. Here it is shown that energy is extracted from the beam not at the center of the beam, but near the outer edges. This is important when considering the total energy source available for growth and acceleration; particles near the center of the beam have relatively less free energy available than particles near the edge of the beam due to the virtual cathode they must traverse when leaving the anode foil. If the energy for growth of the cyclotron wave came predominately from these particles, the wave might of necessity be limited to low amplitude.

D. Wave Growth Saturation and Other Nonlinear Effects

As the cyclotron mode amplitude grows in magnitude, nonlinearities increase in importance. These nonlinearities, in addition to modifying the linear dispersive properties of the mode (nonlinear frequency shifts), will influence mode growth, and may introduce a variety of new phenomena: resonant decay instabilities, nonlinear Landau damping, wave

breaking (or particle crossing), particle heating, and "resonance broadening." The beam cyclotron modes do not appear to be subject to resonant decay instabilities (see Appendix C, Ref. 1); and for a sufficiently cold electron beam, nonlinear Landau effects can be neglected.

The task of evaluating the remaining effects of nonlinearities, understanding their relative importance. and estimating their effects, has been undertaken, with a major emphasis in determining the exact nonlinear mechanism (or mechanisms) responsible for saturation of the growth of the cyclotron wave. This question is not yet completely resolved.

Several analyses have been undertaken to examine the general question of nonlinearities and to determine at what field amplitudes saturation should occur. One such nonlinear effect is discussed in Appendix Q, where attention is focussed on the nonlinear shift $\Delta\omega$ in the wave frequency. The magnitude of $\Delta\omega$ is a measure of the nonlinear corrections to the linear dispersion relation. It is of interest to determine the magnitude of $\Delta\omega$ in terms of the mode amplitude, since such changes may affect optimum growth of

beam cyclotron modes by resistive dissipation, or, in the case of growth produced by resonant coupling to other modes of the system, may lead to mode saturation when $\Delta\omega$ is of the order of the growth rate. This investigation is not yet finished. Final conclusion on the importance of $\Delta\omega$ must await completion of the analysis.

Although the understanding of the nonlinearities is in its early stages, it is already possible to obtain rough estimates of the wave amplitude at which nonlinear effects on the electrons first become significant. A number of such effects are evaluated in Appendix R subject to several approximations which simplify the cyclotron eigenfunctions.

This analysis primarily examines a number of ways in which linear approximations lose their validity, such as when fluctuations in density or electric field amplitudes become comparable to the ambient values, when finite electron gyroradius effects become significant, or when the radial electron flow becomes nonlaminar due to radial electron crossings or overtaking. Although all of these effects are related to one another, the most sensitive nonlinear

effect of this variety is the variation in the electron cyclotron resonance $|\omega - k_z c \beta_z + \Omega|$, sometimes referred to as "resonance broadening," which occurs due to the influence of the waves on the electron quantities β_z and γ. Appendix R also contains some discussion of physical consequences which could arise from nonlinear wave amplitudes of this level, such as wall collisions of the outer electrons or field emission of electrons from the conductor walls. It appears that such effects can be controlled through the presence of the vacuum region between the beam and the wall, and through limiting the ion density to a sufficiently small fraction of the electron density.

In order to guide the analytical effort towards the relevant nonlinear saturation mechanism, computer simulation of the growth and saturation of the axisymmetric cyclotron wave in an anisotropic resistive background has been undertaken. Details are given in Appendix S. Specifically, the cyclotron wave is grown from noise with the beam initialized in an equilibrium background state. The homogeneous, anisotropic resistance is oriented in the

streaming direction (zero conductivity in the transverse directions). The computational results show a growth rate of approximately twice the growth rate predicted by linear theory for this configuration (Appendix T). Because some of the assumptions made in the theoretical derivation are not well satisfied in the simulation, this constitutes satisfactory agreement. The computer simulation shows that the instability tends to saturate when the perturbed electric field in the streaming direction reaches 10 to 20 percent of the transverse DC electric field. Although this is the approximate level where one would expect electron particle crossing to occur, one cannot justifiably infer that particle crossing is the responsible mechanism, since other nonlinear effects discussed in Appendix R are also important at these field amplitudes.

E. Wave Growth Diagnostics

Experimentally, it is necessary to monitor the wave amplitude and phase velocity of the cyclotron wave as it progresses down the wave growth section. The basic diagnostics for detecting the wave would be small electric

and magnetic probes. Since the wave electromagnetic fields extend beyond the beam to the conducting walls of the vessel, the probes can be placed outside the beam, thus preventing interference with the beam and obviating probe damage. Further, since the coupling is electromagnetic, they can be absolutely calibrated in a standard transmission line for field amplitude as a function of frequency. The electric probes measure the radial electric field at the wall and are effectively small patches isolated from the wall upon which induced charge can be measured. They are quite sensitive; their frequency response can extend from the 100 MHz of the lowest waves of interest to several GHz.

The magnetic probes are simply one or two turns of fine wire in a loop of diameter 1 to 4 mm, appropriately shielded electrostatically and connected to cable. They are placed just inside the conducting liner and aligned to measure either B_z or B_θ. Exterior to the beam, B_θ is small for the axisymmetric mode, but not for the non-axisymmetric kink and higher order modes. Hence, discrimination between the desired axisymmetric and the undesired

nonaxisymmetric cyclotron modes is available through the B_θ measurement.

For these cyclotron waves, magnetic probe sensitivity is comparable with that of electric probes. However, their frequency response is somewhat restricted, with the most sensitive probes peaking at 200 MHz. With some sacrifice in sensitivity, suitable coils can have a response extending to 1 GHz.

The probes would be arrayed in clusters at intervals ($\sim$1 m) along the drift tube. Each cluster should include electric and magnetic probes for both components of B. The azimuthal array would give unambiguous determination of structure through m = 2, and the longitudinal array determines k_z for wavelengths of 1 to 40 centimeters. Each cluster should provide complete data on the mode structure (real part of the dispersion relation). Comparison of successive clusters down the tube would determine the growth rates (imaginary part of the dispersion relation). This would provide all the essential information on wave growth.

SECTION VI

ION LOADING AND ACCELERATION

A. Methods of Ion Loading

Several analyses of the ion-wave interaction have been performed to insure that the proof-of-principle experiment on Auto-Resonant acceleration would not flounder on unanticipated difficulties with loading the ions into the cyclotron wave, or with retaining the ions in the wave troughs during the process of wave acceleration. The experimental design contemplates a puff-gas injector section (see Ref. 1, Appendix V), wherein the subject ions will be created by primary beam ionization of a neutral gas, then trapped or picked up by the preformed travelling cyclotron wave, and finally carried out of the puff-gas section into the accelerator section where the wave and ions are accelerated above the initial wave velocity.

In Ref. 1, Appendix V, conditions were presented for the choice of neutral gas density and the spatial volume of the puff-gas section, such that cascading via secondary

ionization could be avoided and the accumulation of untrapped, residual ions in the puff-gas section would not disrupt the electron beam during its pulse time. In Appendix U of this report, this question of ion loading is further explored through theoretical and computer analysis of a model of ion pickup and acceleration. It is shown that ions which are untrapped following wave amplitude growth, even if injected into the accelerator section with a finite velocity v_o, may not later be picked up solely by accelerating the wave velocity to near the injection velocity v_o. Instead it is found that the primary requirement for a high pickup efficiency of the ions into the travelling wave is that the wave must be grown to a sufficient amplitude--roughly $e\Phi \sim \frac{1}{2} M v_\phi^2$--and that such growth and trapping must occur before the wave is accelerated. Provided that there is sufficient amplitude growth of the cyclotron wave before the puff-gas section, there is no harm done in applying a small axial field to the puff-gas section to help eject the residual untrapped ions and so retard their charge accumulation.

B. Stability of Acceleration

It has been shown in a number of analyses (see for example Figure U3 and discussion thereof) that once the ions are sufficiently trapped in the wave, the wave may be accelerated without spilling them if this acceleration is sufficiently gentle. However, there has been concern that the ions might be spilled during acceleration due to spatial ripples or nonadiabatic variations in the magnetic guide field, or else due to voltage droop and ripple in time produced by the impedance variation during diode closure or by transients in the Marx circuitry.

The first question of stable ion acceleration in the presence of spatial magnetic field variations is examined in Appendix I. Computer calculations are described there for a code which integrates the one dimensional ion equation of motion for an arbitrary guide magnetic field profile. A number of runs were performed for the parameters of the proof-of-principle experiment (i.e., $\gamma_e = 7$, $B_{z\,initial} = 25$ kG, $e\Phi_o = 0.5$ MeV, $\varepsilon_{i\,initial} = 0.25$ MeV, $\varepsilon_{i\,final} = 30$ MeV, initial ion

phase = - 0.75 radian w.r.t. bottom of well). For the cases considered, spatial ripple at or below 5 percent of the guide magnetic field amplitude presents no acceleration stability problem. Furthermore, replacing the non-adiabatic portion of the theoretically ideal magnetic field profile with an easily physically realizable, adiabatic profile is found to be completely satisfactory from the viewpoint of acceleration stability, and results in a total increase of the accelerator length of less than 8 percent.

The problem of stable ion acceleration, or phase stability, in the presence of high frequency time ripples in the voltage has been examined previously (see Ref. 1, Appendixes Q, R). Although potentially more serious than spatial magnetic field rippling, due to a cumulative enhancement effect by the number of wavelengths transited by electrons, this high frequency voltage rippling was found to be acceptable if the ripple amplitude could be held below $\pm 1/2$ percent for frequencies above $\sim$ 10 MHz. Subsequent discussions with qualified vendors for such

equipment indicate that this requirement can indeed be met for discharge into a constant 100 ohm load.

For the case of a changing diode impedance, the effects of voltage droop and ripple on ion phase stability have been reevaluated in Appendix B. There it is shown that phase stability is satisfactory unless the voltage droop over the 200 ns pulse time exceeds 20 percent, or low frequency ripple exceeds 5 to 6 percent--figures which are well above the values anticipated.

C. Ion Diagnostics

A conceptual design of the experimental diagnostics required to verify the ion parameters has also been considered, and there appear to be no serious difficulties. The initial requirement of measuring the output ion current intensity may be accomplished by use of a large aperture Faraday cup which is fairly deep. Use of a positive bias voltage of several kilovolts is desirable to prevent any secondary electron emission from escaping the cup and giving an anomalously high reading.

Next, rough proton energy analysis may be accomplished with time of flight techniques. The radial profile of the proton beam current can be estimated with either segmented Faraday cups or with time integrating dosimeter measurements. Time resolved measurements of the instantaneous ion beam energy dispersion may be carried out using a magnetic spectrometer.

SECTION VII

OVERALL SYSTEMS CONSIDERATIONS

Besides the specific system subcomponents which have been treated in previous sections, consideration has also been given to three aspects of the total system. Specifically, these consist of

(1) An operational control system logic for running of the experimental accelerator.

(2) The vacuum requirements necessary in the electron beam drift tube (waveguide).

(3) Selection of a "dump" for the electron (proton) beam which minimizes radiation production, and in conjunction with this the amount of shielding necessary to protect personnel working in the general area surrounding the accelerator.

Each of these items is considered separately below.

A. Operational Control System

For purposes of control system design, the Auto-Resonant Accelerator may be divided in five logical subsystems:

Vacuum System

Magnetic Field System

Marx/Diode Electron Beam Injector

R.F. Exciter

Ion Injector

One possible flow chart of the system sequencing necessary for an experimental run is shown in Figure 1. A brief description of the logic follows.

Prior to any run, it is necessary to insure that the vacuum level in the beam-forming diode and the waveguide are in the proper pressure range. Once this is satisfied, a general visual check is made to insure that signal cables are connected, major subsystems are ready, etc. Then the main power line to the control system is energized, monitors are checked, and safety interlocks are set after insuring that all personnel are outside of the unshielded area around the accelerator. A

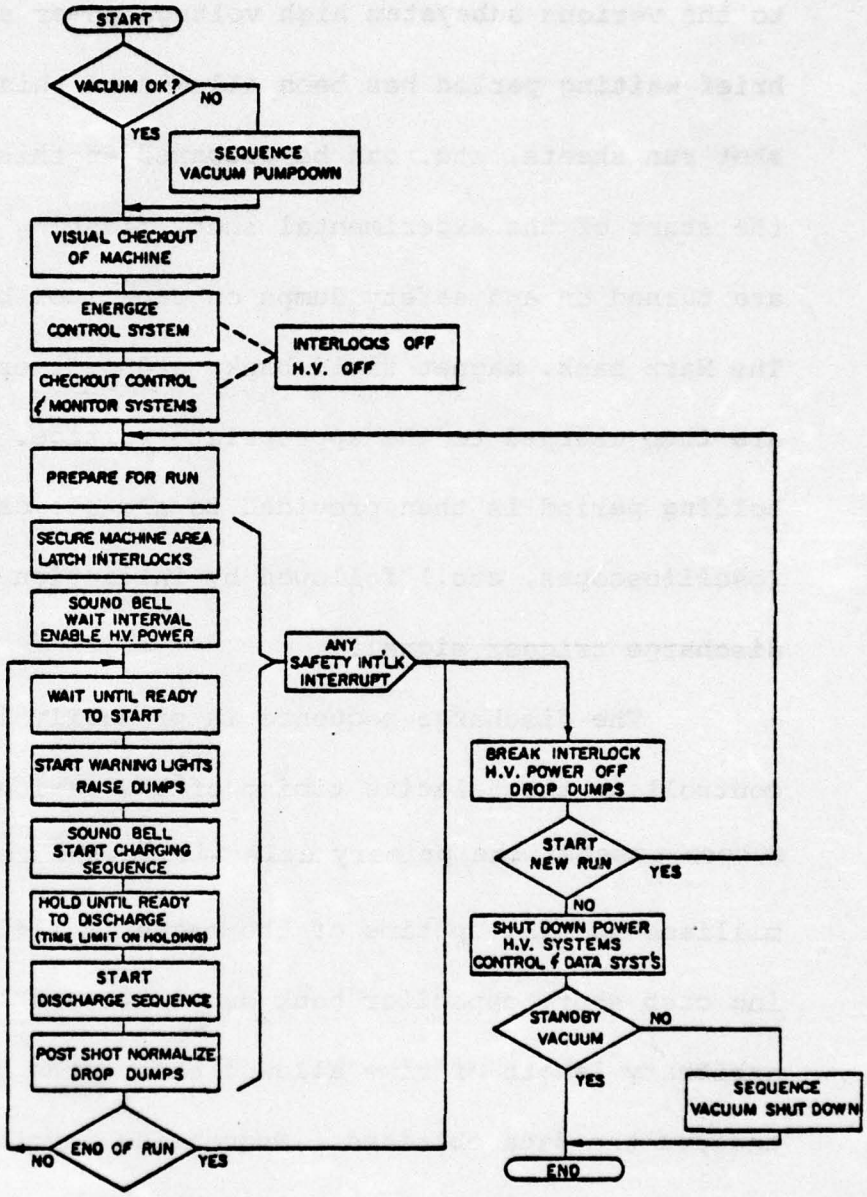

Figure 1. Accelerator Operation Flow Chart

warning bell is then sounded, and main power lines energized to the various subsystem high voltage power supplies. A brief waiting period has been allowed at this point; shot run sheets, etc. can be prepared at this time. At the start of the experimental shot, flashing warning lights are turned on and safety dumps on capacitor banks are lifted. The Marx bank, magnet field bank, and r.f. exciter supply are then charged to the appropriate voltage. A brief holding period is then provided to arm all data recorders (oscilloscopes, etc.) followed by initiation of the main discharge trigger signal.

The discharge sequence is primarily involved in controlling the relative timing of the various system subcomponents; the primary delay is in the roughly 5 millisecond ring-up time of the magnetic field. Following each shot, capacitor bank dumps are enabled and an arbitrary length of time allowed before the next shot to analyze the data obtained. Sequencing involved with any interlock interrupt, or completion of a complete experimental run, is also indicated.

The control system should be automated as much as possible to minimize operational requirements imposed upon the machine operator, and consequently maximizing the number of useful shots.

B. Waveguide Vacuum Requirements

The ambient pressure level necessary in the beam drift tube region is determined by the requirement that the amount of space charge neutralization of the electron beam caused by ionization of the ambient gas not greatly perturb the rigid rotor equilibrium of the beam. The details of the calculation can be found in Appendix V; the result is that a pressure in the 10^{-6} to 10^{-5} range is necessary.

To achieve this level with a modest sized diffusion pump (with cold trapping), the waveguide should be fabricated so that it is "clean" from a vacuum point of view. Thus, the waveguide should be fabricated from type 304 stainless steel and electro-polished. Use of conflat vacuum seals will allow waveguide bake-out to minimize the time required for water vapor pump-out.

Given these general specifications, attainment of the necessary vacuum level is not a problem.

C. Beam Dump and Radiation Shielding

Selection of the best material for stopping the electron (and/or proton) beam at the end of the accelerator is predicated on withstanding the high energy fluence in the electron beam and minimizing radiation production. As shown in Appendix W, graphite is the best selection.

Based on obtaining data at the rate of one shot every 5 minutes, Appendix W also indicates that 4 feet of concrete placed around the beam dump is necessary to reduce radiation levels to national safety levels. In addition, a wall of concrete 2 feet thick along both sides of the accelerator is required to prevent high radiation exposure on any shot in which, for whatever reason, the beam strikes the waveguide wall.

To insure proper monitoring of radiation exposure, all laboratory personnel would be required to wear a radiation film badge and have the exposure determined on a monthly basis. Pocket dosimeters placed on the

beam dump shielding, and also on the side shielding, should be checked weekly to determine if any radiation problems are occurring.

APPENDIX A

ELECTRON BEAM INJECTOR CONSIDERATIONS

Introduction

In designing an experimental program to demonstrate the feasibility of the Auto-Resonant Accelerator concept, the following parameters have been chosen for the output ion (proton) beam:

Proton Energy = 30 MeV

Proton Current = 30 amps

Pulse Duration $\geq$ 100 ns

The peak power in the ion beam is then 9×10^8 watts, and this should represent a small fraction of the accelerating media (electron beam) peak power level. Thus, we require

$$9 \times 10^8 \ll V_e I_e$$

To be conservative, the following values were chosen:

V_e = 3.0 MeV

I_e = 30 kA

τ_e = 200 ns pulse width

ion beam power is then 1% of that available in the electron beam.

In the remainder of this appendix consideration is given to specifying the electron beam injector, based upon these nominal characteristics.

Time Varying Diode Impedance

For real cold cathode diode systems, the electron source is a plasma sheath formed on the cathode surface. This plasma has a high thermal temperature and expands ballistically with a velocity of 2 to 3 cm/μs. This produces a continuously decreasing gap spacing in the diode, and causes the effective diode impedance (Z_L) to decrease with time.

If one assumes that the electrical network feeding the diode can be represented by a battery and an effective

internal impedance (Z_I), then the load voltage will scale as

$$V_L \sim \frac{Z_L}{Z_L + Z_I} \tag{A1}$$

The change in load voltage introduced by the time dependence of Z_L is then

$$\frac{\Delta V_L}{V_L} = \left(\frac{Z_I}{Z_L + Z_I} \right) \frac{\Delta Z_L}{Z_L} \tag{A2}$$

while the change in load current is given by

$$\frac{\Delta I_L}{I_1} = - \left(\frac{Z_L}{Z_L + Z_I} \right) \frac{\Delta Z_L}{Z_L} \tag{A3}$$

Since the local phase velocity of the accelerating wave is

$$v_\phi = \frac{\omega_o}{\omega_o + \Omega} \sim V_L \tag{A4}$$

then the change in local phase velocity is

$$\frac{\Delta V_\phi}{V_\phi} = \frac{\Delta V_L}{V_L} \qquad \text{(A5)}$$

To insure that the ion energy does not change appreciably throughout the pulse length, Equation (A5) (Equation written as Eq. hereafter) should be as small as possible. From Eq. (A2) this implies that the electron accelerator internal impedance be small compared to 100 ohms. Thus, in evaluating a machine design we want

$$Z_I < Z_L \ (\simeq 100 \text{ ohms}) \qquad \text{(A6)}$$

High Frequency Ripple

As discussed (Ref. 1, Appendixes Q and R), high frequency voltage ripple (superimposed on a slow voltage droop) can produce phase shifts which de-trap ions and terminate the collective acceleration process. Filter elements are therefore probably required between the high voltage source and the electron beam diode load. Also, since the magnitude of voltage ripple generated by inductive components in the system scales like dI/dt, a slow pulse rise time is desirable.

Both analytic and computer studies of the effect of high frequency ripple indicate that in the frequency range from 10 MHz up the amplitude should be kept at 0.5% or less. This has been incorporated in the injector specifications.

Electron Injector Specification

The following specifications have tentatively been chosen for the electron beam injection source:

1. Load: 100 Ω (constant impedance dummy load for tests)
2. Peak voltage (V_{pk}) into 100 Ω: 3 MeV
3. Duration: 200 ns minimum useful pulse between 0.96 V_{pk} points (± 2%)
4. Reproducibility of V_{pk} shot to shot: ± 2%
5. Rise time: ≤ 100 ns (5% to 95% of V_{pk})
6. Prepulse suppression: Maximum prepulse less than 3% of V_{pk} (measured with no dummy load)
7. Ripple: Less than ± 1/2% high frequency (≥ 10 MHz) ripple during useful pulse ($V \geq 0.96\ V_{pk}$)

8. Triggering: Command triggered with less than ± 200 ns jitter between triggering and firing
9. Pulse clipping crowbar switch to reduce energy into 100 Ω load to less than 10% of initial stored energy after 200 ns useful pulse (0 to + 50 ns jitter allowed in crowbar switch)
10. The electrical circuit driving the load should have a low internal impedance.

The prepulse suppression criterion was added to eliminate cathode turn-on prior to arrival of the main voltage pulse. The slow rise time requirement will hopefully minimize ripple generated by inductive components. The addition of a crowbar to eliminate any late-time energy flow in the diode is meant to protect the diode anode. This is discussed in another appendix.

Finally, it is worth noting that the testing of the injector is done using a 100 ohm dummy load. This was felt to be necessary since at this time the actual diode has not been designed, and therefore its time behavior cannot be predicted. However, it is anticipated that

any injector design selected will be analyzed numerically to determine its sensitivity to a time varying load.

Diode Design Considerations

Design of the conventional diode which will be used for initial experimentation, as well as foilless diode design, will be made using a computer code (Ref. 2) similar to that developed at Sandia (Ref. 3). This self-consistent code is relativistically correct, and includes the beams self-magnetic field as well as an externally applied field.

---

2. "Research on Beam Stopping Due to Self-Magnetic Compression," DASA 2167, Ion Physics Corp., Nov. 1968.

3. Boers, J. E., "Digital Computer Simulation of High Current, Relativistic, and Field Emission Electron Tubes," Proc. of 11th Symp. on Electron, Ion, and Laser Beam Technology, 1972.

APPENDIX B

THE EFFECTS OF VOLTAGE DROOP AND LOW FREQUENCY RIPPLE ON ACCELERATOR PHASE STABILITY

Introduction

Specifications of the Marx generator and diode assembly electron beam source detailed in Appendix B were quoted for output into a constant 100 ohm load. Subsequent discussions with qualified vendors of such assemblies showed that the ripple suppression circuits envisioned are tuned to this constant 100 ohm load impedance to provide the proper low frequency voltage waveshape.

An actual diode will of course undergo closure during the 200 ns pulse time at a rate of roughly 1 to 2 cm/μs, resulting in estimated 40 percent droop in load impedance; i.e. from 100 ohms to 60 ohms. The question of the effect of such a changing load impedance was subsequently brought to the attention of the vendors. Two general conclusions were deduced:

1. Such a changing load impedance will have a negligible effect on the ability of the circuits to effectively suppress high frequency ripple.

2. Such a changing impedance will, however, affect significantly the overall output voltage waveform, resulting in a significantly increased voltage droop and the introduction of low frequency ripple components associated with the pulse forming networks.

In order to ascertain the effect of such droop and low frequency ripple, an updated version of the phase stability code was run with a voltage wave form modelling increasingly larger amounts of droop and low frequency ripple. Specifically, the low frequency ripple was assumed to correspond to roughly 8 MHz at levels of 1, 2, 3, 4, 6, 8, and 10 percent with voltage droop of 10, 20, 30, 40, and 50 percent over the 200 ns pulse time.

Accelerator parameters were chosen for an output of 30 MeV ions from an initial injection energy of 250 keV, using a cyclotron wave amplitude of 500 keV. Two specific accelerator configurations were considered.

In the first, a short accelerator with a low safety factor of only 1.5 (high fraction of total electric field available used for acceleration), was considered. Results show that phase stability was maintained for voltage droops of 20% or less or for ripple level at 6% or lower.

For the second, more conservatively designed accelerator with a safety factor of 2.0 (i.e. utilizing only half of the total electric field for acceleration), phase stability was again maintained at voltage droops of 20 percent or less but the ripple amplitude was here required to be less than the 6 percent figure for the first case.

A tabulation of the results of this series of runs is given in Table B1.

TABLE B1

THE EFFECTS OF VOLTAGE DROOP AND LOW FREQUENCY RIPPLE ON ACCELERATOR PHASE STABILITY

Safety Factor	Droop (Percent)	Ripple @ 8 MHz (Percent)	Acceleration Time (ns)
1.5	10%	1%	70
1.5	10	2	93
1.5	10	3	98
1.5	10	4	101
1.5	10	6	106
1.5	10	8	phase stability lost
1.5	10	10	phase stability lost
1.5	20	1	106
1.5	30	1	phase stability lost
1.5	40	1	phase atability lost
1.5	50	1	phase stability lost
2.0	10	1	100+
2.0	10	2	105
2.0	10	3	106
2.0	10	4	107
2.0	10	6	phase stability lost
2.0	10	8	phase stability lost
2.0	10	10	phase stability lost
2.0	20	1	132
2.0	30	1	phase stability lost
2.0	40	1	phase stability lost
2.0	50	1	phase stability lost

APPENDIX C

ANODE SURVIVAL SPECIFICATION

Using a real diode, that is a cold plasma cathode, the current density as a function of time can be written

$$j(t) = \frac{f(V(t))}{d_o^2 (1 - t/\tau)^2}$$

with $f(V)$ the functional dependence of current density on diode voltage and d_o the initial gap spacing;

$$\tau = \frac{d_o}{v_o}$$

where

v_o = plasma closure velocity

$\approx 2.5 \times 10^{-3}$ cm/ns

For voltages greater than 200 keV, and assuming a 0.001 inch titanium anode, the dose delivered to the anode is

$$\int j(t) \frac{dE}{dx} dt$$

where

dE/dx = ionization energy loss by the primary beam in volt. cm^2/gm

If time is measured in nanoseconds, then in this range one can use the approximation

$$\frac{f(V)}{d_o^2}\frac{dE}{dx}(v) * 10^{-9}\ \text{sec} = \frac{0.693}{d_o^2} V_{MV}^{1.274} \qquad \text{(C1)}$$

where V is measured in units of 10^6 volts.

For energies of 70 keV and lower, the electron beam is totally stopped in the anode and the dose delivered is higher than that given by the above expression. Between 70 keV and 200 keV there is a smooth transition to the above formula.

At time $t = t_o$, the diode voltage pulse is over and no more energy is delivered to the foil. Thus, neglecting the enhanced dose below 200 keV, the foil dose is roughly

$$D \simeq \frac{0.693}{d_o^2} \int_o^{t_o} \frac{V_{MV}^{1.274}}{(1 - t/\tau)^2}\, dt \quad \frac{cal}{gm} \qquad \text{(C2)}$$

For titanium, the dose required to raise it to the melt temperature is $\approx$ 200 cal/gm. Thus, it is required that

$$\frac{1}{d_o^2} \int_o^{t_o} \frac{V^{1.274}}{(1 - t/\tau)^2}\, dt < 289 \qquad \text{(C3)}$$

As an example, assume

$V = 3.0$ MeV

$t_o = 200$ ns

then the left hand side of Eq. (C3) gives

$$\frac{811}{d_o^2} \frac{\tau}{\tau - 200} = \frac{811}{d_o(d_o - 0.5)} \qquad \text{(C4)}$$

Setting

$d_o \simeq 3$ cm.

which corresponds to a 1 kA/cm^2 current density then Eq. (C4) becomes numerically equal to 108. Thus, the inequality of Eq. (C3) is well satisfied and one can anticipate foil survival and multishot capability.

APPENDIX D

DIODE DIAGNOSTICS

A knowledge of the injected beam parameters--energy and current--is essential for interpreting experimental measurements made in the development of the Auto-Resonant Accelerator. While the manufacturer of the pulsed accelerator used to form the electron beam will provide diagnostics to measure the capacitively graded tube voltage, inductive corrections of relatively large magnitude must be made to infer the actual diode gap voltage from this type of data. To eliminate this, the diagnostic configuration shown in Figure D1 is deemed necessary for diode characterization. The probes consist of a capacitive voltage divider to measure the shank voltage very near the cathode, and a resistive current shunt to measure the wall return current driven by the B_θ field generated by the beam current.

The resistive current shunt consists of a dielectric break in the wall return path shunted by a low impedance band of parallel (carbon composition) resistors. This provides a low impedance voltage source for driving a 50 ohm signal cable. The resistor band structure has an

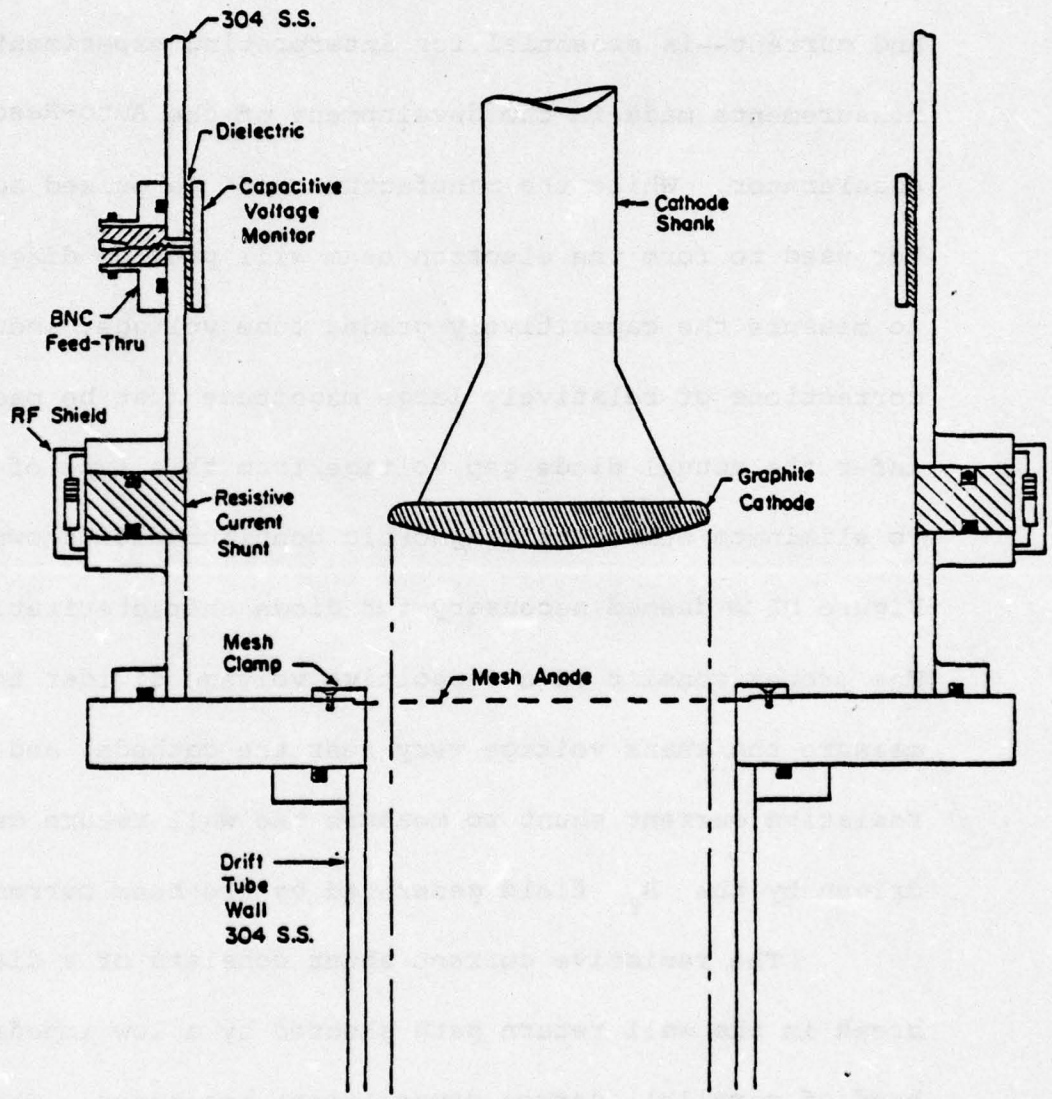

Figure D1. Diode Diagnostic Configuration

intrinsically low self-inductance, and a subnanosecond rise time is obtained. This is more than adequate for the anticipated slow current rise time of the pulsed accelerator. Calibration of the shunt can be accomplished using the 50 ohm transmission line structure, easily fabricated out of sheet metal, shown in Figure D2. A transmission line pulser launches a square voltage wave onto a 50 ohm cable; the cable feeds through a GR connector onto a 50 ohm biconic line which matches into a 50 ohm coaxial line. The current shunt is located in the middle of this line. A second biconic line/GR connector feeds the output cable (50 ohm) which goes to a matched termination oscilloscope preamp input. The continuity of the 50 ohm wave impedance along this structure ensures that no reflections will occur, and the measured voltage amplitude at the oscilloscope (V_2) is actually the voltage driving current in the shunt. Thus, the shunt current is simply

$$I_s = \frac{V_2}{50} \qquad \text{(D1)}$$

A second oscilloscope measures the output voltage of the current shunt (V_1). The resistive shunt calibration is then obtained:

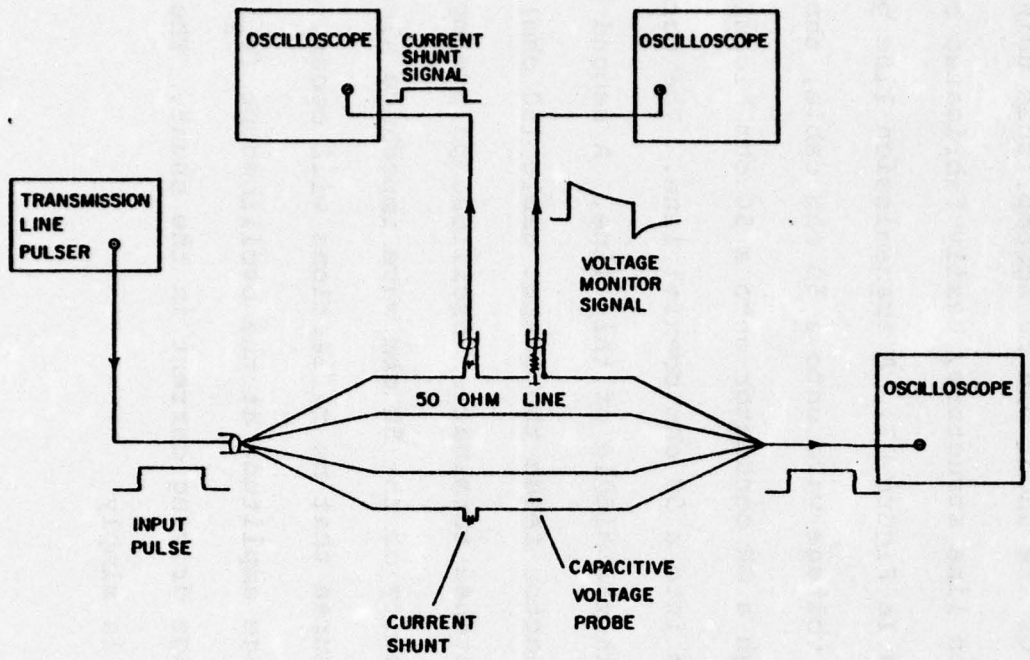

FIGURE D2: CALIBRATION SYSTEM FOR DIODE VOLTAGE MONITOR AND CURRENT SHUNT

$$G_I = \frac{I_s}{V_1} \qquad \frac{\text{amps}}{\text{volt}} \tag{D2}$$

= inverse of shunt resistance

It should also be noted that the transmission line structure can be used to calibrate $\dot{B}$ and B loops, as well as E-field probes.

The cathode voltage monitor depends on the capacitive division of the total voltage $(V_o(t))$ between the shank/monitor band capacitance (C_1) and the monitor band/ground capacitance (C_2). A resistor (R) feeds the band signal $(V_M(t))$ onto a coaxial transmission line of wave impedance Z. The relationship between V_o and V_M is given by:

$$V_o(t) = G_v \left\{ V_M(t) + \frac{1}{\tau} \int_o^t V_M(t')\, dt' \right\} \tag{D3}$$

where

$$G_v = \frac{(R+Z)(C_1+C_2)}{ZC_1} \tag{D4}$$

and

$$\tau = (R+Z)(C_1+C_2) \tag{D5}$$

For reference, the inverse relation is

$$V_M(t) = \frac{1}{G_v} e^{-t/\tau} \int_0^t \frac{dV_o(t')}{dt} e^{t'/\tau} dt' \qquad (D6)$$

From Eq. (D3) it can be seen that over most of the pulse the integral correction can be made small if the time constant, τ, is large compared to the pulse length. The major correction will be at late time, low voltage levels when the correction can be large. This will not be a problem during the major flat top portion of the pulse when the main Auto-Resonant acceleration is occurring.

Calibration of the monitor requires a determination of G_v and τ. This can be done in situ using the technique shown in Figure D3. A transmission line pulser generates a square pulse which is split by an unmatched tee. One leg of the tee goes directly to the cathode shank, and quickly charges up the tube/diode stray capacitance to a voltage V_{max}. The other leg goes to an oscilloscope which records V_{max}. The voltage probe output, V_M, is recorded on another oscilloscope. From Eq. (D6), assuming V_{max} is a step function, there obtains

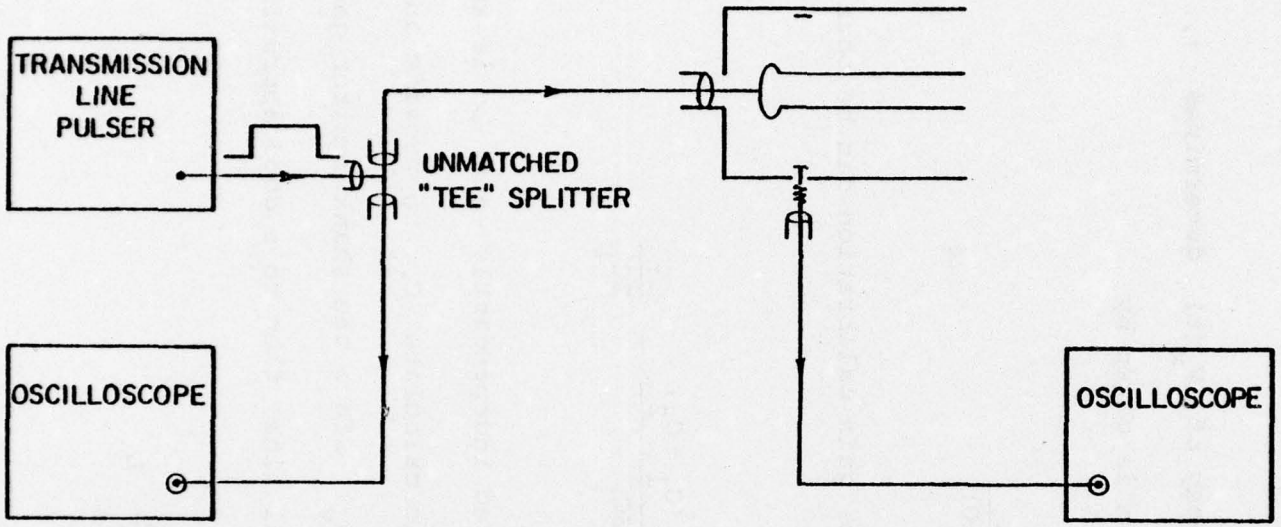

FIGURE D3: IN SITU CALIBRATION OF
DIODE VOLTAGE MONITOR

$$V_M(t) = \frac{V_{max}}{G_v} \; e^{-t/\tau} \qquad \text{(D7)}$$

The slope of the decay of $V_M(t)$ determines τ, while the gain calibration is given by

$$G_v = \frac{V_{max}}{V_M(t=0)} \qquad \text{(D8)}$$

A cross-check on the gain calibration can be obtained by noting that

$$G_v = \frac{(R+Z)(C_1+C_2)}{ZC_1} = \frac{\tau}{ZC_1} \qquad \text{(D9)}$$

Since τ is measured independently and Z is known, it is only necessary to calculate C_1 to provide another determination of G_v. Since the shank/monitor geometry is that of a coaxial line, then to a good approximation

$$C_1 = \frac{2\pi \; \varepsilon_o}{\ell n \; r_M/r_s} \; L \qquad \text{(D10)}$$

where

r_M = monitor radius

r_s = shank radius

L = length of monitor band

Previous experience has shown that these two methods of determining G_v give good agreement.

APPENDIX E

TRANSITION TO BEAM EQUILIBRIUM REGION

Since the electron beam is injected into the drift tube region through a conducting anode foil which is at the same (ground) potential as the drift tube (waveguide) wall, there is a transition region near the anode where the radial electric fields are small and the axial electric field dominates. In what follows the extent of the transition region is estimated, and comments are made on the beam equilibrium.

Assume that an equilibrium exists, and that the beam density is uniform ($= n_o$) at all points. The potential distribution is defined by

$$\nabla^2\varphi = \frac{1}{R}\frac{\partial}{\partial R}\left(R\frac{\partial\varphi}{\partial R}\right) + \frac{\partial^2\varphi}{\partial Z^2} = \left(\frac{\omega_{po}^2\, a^2}{c^2}\right) V_e \qquad \text{(E1)}$$

where

$$\omega_{po} = \left(\frac{e^2\, n_o}{m_o\, \epsilon_o}\right)^{1/2} = \text{nonrelativistic beam plasma frequency}$$

a = inner radius of drift tube (also assumed equal to the electron beam radius)

$V_e = m_o c^2/e = 511$ keV

$R = r/a$

$Z = z/a$

Setting

$$\varphi(R,Z) = \varphi_1(R) + \varphi_2(R,Z) \tag{E2}$$

and

$$\nabla^2\varphi_1 = \left(\frac{\omega_{po}^2 a^2}{c^2} \right) V_e \tag{E3}$$

$$\nabla^2\varphi_2 = 0 \tag{E4}$$

with the boundary conditions

$$\varphi(R = a, Z) = \varphi(R, Z = 0) = 0 \tag{E5}$$

then it is easy to show that

$$\varphi_1(R) = -1/4 \left(\frac{\omega_{po}^2 a^2}{c^2} \right) V_e (1 - R^2) \tag{E6}$$

and

$$\varphi_2(R,Z) = 1/4 \left(\frac{\omega_{po}^2 a^2}{c^2} \right) V_e \sum_{n=1}^{\infty} \frac{c_n}{J_1^2(\lambda_n)} J_o(\lambda_n R) \times e^{-\lambda_n Z} \tag{E7}$$

where

$$c_n = \int_o^1 (1 - x^2)\ J_o(\lambda_n x)\ d(x^2) \tag{E8}$$

$$\lambda_n = n^{th} \text{ value of } x \text{ for which } J_o(x) = 0 \tag{E9}$$

Generally, φ_2 is dominated by the $n = 1$ term; this will be negligibly small when

$$e^{-\lambda_1 Z_o} \ll 1 \tag{E10}$$

This will be true when

$$Z_o = \frac{\ell}{a} \geq 2 \qquad (e^{-\lambda_1 Z_o} < 10^{-2}) \tag{E11}$$

or, in other words, the transition region length required

to eliminate any z-dependence in the potential is roughly one drift tube diameter.

The cold fluid Lorentz force equation yields the following equations of motion:

$$\frac{d}{dt}(\gamma v_r) = \frac{\gamma v_\theta^2}{r} - \frac{|e|}{m_o} v_\theta B_z + \frac{|e|}{m_o}\left(\frac{\partial \varphi}{\partial r} + v_z B_\theta\right) \tag{E12}$$

$$\frac{d}{dt}(\gamma r^2 \dot{\theta}) = -\frac{|e|}{m_o} r\left(v_z B_r - v_r B_z\right) \tag{E13}$$

$$\frac{d}{dt}(\gamma v_z) = -\frac{|e|}{m_o}\left(-\frac{\partial \varphi}{\partial z} + v_r B_\theta - v_\theta B_r\right) \tag{E14}$$

where

B_z = externally generated solenoidal guide field

B_θ = beam generated magnetic field

$v_\theta = r\dot{\theta}$

$\beta = \left(v_r^2 + v_\theta^2 + v_z^2\right)^{1/2}/c$

$$\gamma = (1 - \beta^2)^{-1/2}$$

Assuming axisymmetric $(\partial/\partial\theta = 0)$, time independent $(\partial/\partial t = 0)$ motion, the relevant Maxwell equation is

$$\vec{\nabla} \times \vec{B} = \mu_o \vec{j} = - |e| n_o \mu_o \vec{v} \tag{E15}$$

Consider now the beam equilibrium beyond the transition region; it is required that

$$v_r = 0 \tag{E16}$$

and

$$\frac{d}{dt} (\gamma v_r) = 0 \tag{E17}$$

We assume

$$B_z = B_o = \text{constant} \tag{E18}$$

$$m_o c^2 (\gamma_o - 1) = \text{injection energy of electrons at the anode} \tag{E19}$$

From Eq. (E15),

$$B_\theta = - |e| \, n_o \, \mu_o \, \frac{1}{r} \int_o^r v_z(r') \, r' \, dr' \tag{E20}$$

and if

$$v_z(r') \simeq v_z = \text{constant} \tag{E21}$$

then

$$B_\theta = - \left(\frac{\omega_{po}^2 \, a^2}{c^2} \right) V_e \, \frac{\beta_z}{c} \, \frac{r}{2a^2} \tag{E22}$$

Then Eq. (E12) becomes

$$\frac{\gamma v_\theta^2}{r} - \Omega_o \, v_\theta + \frac{|e|}{m_o} \left(\frac{\omega_{po}^2 \, a^2}{c^2} \right) V_e \, (1 - \beta_z^2) \, \frac{r}{2a^2} = 0 \tag{E23}$$

where

$$\Omega_o = \frac{|e| B_o}{m_o}$$

while energy conservation gives

$$\gamma(r) = \gamma_o \left(1 - \frac{\omega_p^2 a^2}{4c^2} (1 - r^2/a^2)\right) \qquad \text{(E24)}$$

(Note:

$\omega_p = \omega_{po}/\gamma_o^{1/2}$ = relativistic beam plasma frequency

and in terms of conventional beam terminology

$$\frac{\omega_p^2 a^2}{4c^2} = \frac{\nu}{\gamma} = \frac{I_B}{17 \beta \gamma_o}$$

where

I_B = total beam current in kA)

The two solutions to Eq. (E23) are

$$v_\theta = r \dot{\theta} = \frac{\Omega_o r}{2\gamma} \left\{1 \pm \sqrt{1 - 2 \frac{\omega_{po}^2}{\Omega_o^2} \gamma (1 - \beta_z^2)}\right\} \qquad \text{(E25)}$$

If

$$\frac{2 \omega_{po}^2 \gamma(1 - \beta_z^2)}{\Omega_o^2} \ll 1 \qquad \text{(E26)}$$

then Eq. (E26) has solutions given by:

$$(v_\theta)_1 \simeq \frac{\Omega_o r}{\gamma} \tag{E27}$$

and

$$(v_\theta)_2 \simeq \frac{\omega_{po}^2 (1 - \beta_z^2)}{2 \Omega_o} r \tag{E28}$$

Note that

$$(v_\theta)_2 \simeq \frac{1}{4} \left(\frac{2 \omega_{po}^2 \gamma (1 - \beta_z^2)}{\Omega_o^2} \right) (v_\theta)_1 \ll (v_\theta)_1 \tag{E29}$$

from Eq. (E26). In general, it is assumed that one operates with the slow rotational equilibrium

$$\beta_\theta = \frac{(v_\theta)_2}{c} \ll \beta_z \tag{E30}$$

so that

$$(1 - \beta_z^2) \simeq \frac{1}{\gamma^2} \tag{E31}$$

and

$$\dot{\theta} \simeq \frac{\omega_{po}^2}{2\,\Omega_o\,\gamma^2} \tag{E32}$$

The slow rotation of the beam generates a diamagnetic field, ΔB_z, which tends to cancel the main guide field B_o. The maximum cancellation can be shown to be

$$\frac{-\Delta B_z}{B_o} = \frac{\omega_{po}^2}{\Omega_o^2\,\gamma^2}\left(\frac{\omega_p^2\,a^2}{c^2}\right) \ll 1 \tag{E33}$$

so that diamagnetic effects can be ignored.

If the beam is immersed in a uniform magnetic field, then Eq. (E13) can be re-written as

$$\frac{d}{dt}\left(\gamma\, r^2\,\dot{\theta} - \frac{|e|}{m}\,\frac{r^2}{2}B_z\right) = 0 \tag{E34}$$

If

r_o = initial radius at the cathode

and assuming

$\dot{\theta} = 0$ at the cathode

then

$$r\dot{\theta} = \frac{|e|B_z}{2m}\left(1 - r_o^2/r^2\right) = \frac{\Omega_o}{2}\left(1 - r_o^2/r^2\right) \qquad \text{(E35)}$$

Using Eq. (E32), there obtains

$$\left(1 - r_o^2/r^2\right) = \frac{\omega_{po}^2}{\Omega_o^2 \gamma} \leq 1 \qquad \text{(E36)}$$

Note also that achievement of the slow rotational equilibrium requires immersing the diode in the magnetic field.

APPENDIX F

BEAM COMPRESSION

The magnetic compression of the initial rigid rotor equilibrium of the beam to a smaller radius is to be carried out in such a way that miminal heating of the beam occurs. The following analysis assumes:

(1) The compression is carried out over a distance-Δz--which is large so that E_z force effects can be neglected. The space charge electric field is all radial.

(2) Diamagnetic effects are ignored.

(3) The centrifugal term is negligible.

(4) The beam orbits follow equipotential surfaces. This is achieved by shaping of the waveguide wall. Then the γ factor remains constant.

(5) Time derivatives are replaced with axial derivatives, that is,

$$\frac{d}{dt} = \vec{v} \cdot \vec{\nabla} \simeq v_z \frac{d}{dz} \simeq c \frac{d}{dz}$$

(6) The axial magnetic field, $B_z(r=0,z) = B_o(z)$, is assumed given.

(7) $\frac{\omega_p^2}{\gamma^2\Omega^2} \ll 1$ at all points.

Within these approximations, the radial force equation can be written as

$$\gamma c \frac{dv_r}{dz} = \left[\frac{\omega_p^2 r^2}{2\gamma} - \gamma r^2 \dot{\theta} \left(\frac{|e|}{m\gamma} B_z (r,z) \right) \right] \frac{1}{r} \qquad \text{(F1)}$$

while conservation of canonical angular momentum gives

$$-\gamma r^2 \dot{\theta} = \frac{\gamma \Omega_i r_i^2}{2} \left(1 - \frac{\omega_{pi}^2}{\gamma^2 \Omega_i^2} \right) - \frac{|e|}{m} A_\theta (r,z) \qquad \text{(F2)}$$

where

$$B_z(r,z) = \frac{1}{r} \frac{\partial}{\partial r} (rA_\theta) = B_o(z) - \frac{1}{4} r^2 \frac{d^2 B_o}{dz^2} + \ldots \qquad \text{(F3)}$$

Defining

$$\Omega(z) = \frac{|e|}{m\gamma} B_o(z)$$

then

$$\gamma c \frac{dv_r}{dz} = -\left\{ \frac{\gamma \Omega r^2}{2} \left(1 - \frac{\omega_p^2}{\gamma^2 \Omega^2} \right) - \frac{\gamma \Omega_i r_i^2}{2} \left(1 - \frac{\omega_{pi}^2}{\gamma^2 \Omega_i^2} \right) \right\} \frac{\Omega}{r}$$

$$+ \frac{1}{4} r \frac{d^2 \Omega}{dz^2} \left\{ \frac{\gamma \Omega r^2}{2} \left(1 - \frac{\omega_p^2}{\gamma^2 \Omega^2} \right) - \frac{\gamma \Omega_i r_i^2}{2} \left(1 - \frac{\omega_{pi}^2}{\gamma \Omega_i^2} \right) \right.$$

$$\left. + \frac{\omega_p^2 r^2}{2\gamma\Omega} \right\} + \frac{1}{16} \gamma r^3 \Omega \frac{d^2 \Omega}{dz^2} + \ldots \qquad \text{(F4)}$$

To lowest order, the equilibrium orbit is defined by the relation

$$\Omega r_o^2 \left(1 - \frac{\omega_p^2}{r^2\Omega^2}\right) = \Omega_i r_i \left(1 - \frac{\omega_{pi}^2}{\gamma^2\Omega_i^2}\right) \tag{F5}$$

or, given assumption (7),

$$\Omega r_o^2 = \Omega_i r_i^2 \tag{F6}$$

Now set

$$r = r_o + \delta r = r_o + \epsilon r_o \tag{F7}$$

where

$$\epsilon = \frac{\delta r}{r_o} \ll 1 \tag{F8}$$

Then

$$v_r = c \frac{dr_o}{dz} + c \frac{d}{dz}(\epsilon r_o) \tag{F9}$$

$$= c \frac{dr_o}{dz} + c \frac{\delta v_r}{c}$$

and to first order

$$\frac{d}{dz}\left(\frac{\delta v_r}{c}\right) = \frac{1}{16}\left(\frac{\Omega_i r_i^2}{c^2}\right) r_o \frac{d^2\Omega}{dz^2} - \frac{d^2 r_o}{dz^2}$$

$$- \left(\frac{\Omega_i r_i^2}{c^2}\right)\left(\frac{\Omega}{r_o} - \frac{7}{16} r_o \frac{d^2\Omega}{dz^2}\right)\epsilon \tag{F10}$$

Assuming that

$$\frac{7}{16}\ \frac{r_o^2}{\Omega}\ \frac{d^2\Omega}{dz^2} \ll 1$$

and using the following normalized units

$$f = \Omega/\Omega_i$$

$$x = z/\Delta z$$

then

$$\frac{d}{dx}\left(\frac{\delta v_r}{c}\right) = \frac{r_i}{\Delta z}\left\{-\frac{d^2 f^{-1/2}}{dx^2} + \frac{1}{16}\left(\frac{\Omega_i r_i}{c}\right)^2 \frac{1}{f^{1/2}}\frac{d^2 f}{dx^2}\right.$$

$$\left. - \left(\frac{\Omega_i \Delta z}{c}\right)^2 f^{3/2}\ \epsilon\right\} \qquad \text{(F11)}$$

Assuming

$$\frac{df}{dx}\ (x=0) = 0$$

then Eq. (F11) can be integrated once to give

$$\frac{\delta v_r}{c} = \frac{r_i}{\Delta z}\frac{d}{dx}\left(\frac{\epsilon}{f^{1/2}}\right)$$

$$= \frac{r_i}{\Delta z}\left\{-\frac{df^{-1/2}}{dx} + \frac{1}{8}\left(\frac{\Omega_i r_i}{c}\right)^2 \frac{df^{1/2}}{dx}\right.$$

$$+ \frac{1}{2} \left(\frac{\Omega_i r_i}{c}\right)^2 \int_o^x \left(\frac{df^{1/4}}{dx}\right)^2 dx'$$

$$- \left(\frac{\Omega_i \Delta z}{c}\right)^2 \int_o^x f^{3/2} \epsilon \, dx' \Bigg\} \qquad \text{(F12)}$$

This equation can then be integrated to give an integral equation solution for ϵ.

Alternatively, one can note that

$$\frac{r_i}{\Delta z} \ll 1$$

so that keeping $\delta v_r/c$ small requires only that

$$\frac{d}{dx}\left(\frac{\epsilon}{f^{1/2}}\right) = g(x) < 1 \qquad \text{(F13)}$$

Then setting

$$g(x) = C_o f^n \frac{df}{dx}, \text{ where } C_o \text{ is a constant,} \qquad \text{(F14)}$$

gives a unique relation between ϵ and f. Inserting this relation into Eq. (F12), a differential equation for f is obtained which can be integrated numerically to give the field profile. Finally, an alternate approach is to define

$$h(x) = \frac{\epsilon}{f^{1/2}} \tag{F15}$$

so that

$$\frac{d^2h}{dx^2} + \left(\frac{\Omega_i \Delta z}{c}\right)^2 f^2 h = -\frac{d^2 f^{-1/2}}{dx^2}$$

$$+ \frac{1}{8}\left(\frac{\Omega_i r_i}{c}\right)^2 \left\{\frac{d^2 f^{1/2}}{dx^2} + 4\left(\frac{df^{1/4}}{dx}\right)^2\right\} \tag{F16}$$

which, given a specified $f(x)$, can be used to determine $\epsilon(x)$ and $\delta v_r/c$.

APPENDIX G

ELECTRON BEAM DIAGNOSTICS

The types of diagnostics which will be used for electron beam characterization are quite standard. Because of the current densities and pulse length involved, thin film dosimeters are excluded. Specific pieces of apparatus will include

A. Total Stopping Graphite Calorimeters

The incident beam energy,

$$E = \int VI \, dt$$

is converted to thermal energy in the graphite. Its temperature rise

$$\int_{T_o}^{T} Cp(t) \, dT = E$$

is monitored with a thermocouple and read out on a slow scope trace.

B. Segmented Calorimeters

A segmented graphite array is used to collect and measure instantaneous average current density over selected segments of the beam.

C. Current Shunts

Return current shunts will be used to measure transmitted current efficiency. These consist of parallel bands of carbon resistors selected to give a total shunt resistance of about 10 milliohms. By tapping off the shunt signal at various azimuthal positions it is possible to infer the centering of the beam in the wave guide.

D. Diamagnetic Loops

These single turn loops encircling the beam generate an output signal which is a measure of the average transverse energy (Ref. 4).

E. X-ray Diagnostics

Using a total stopping bremsstrahlung target, it is possible to infer anode information using pinhole

---

4. Hammer, D.A., "Pressure Balance in Pulsed Plasmas with Large Self-Fields," Phys. Fluids 11, #6, pp. 1260 (June 1974).

photography, and near- and far-field radiation profiles measured with dosimeters.

F. Magnetic Loops

Both B and $\dot{B}$ loops can often be used to infer structure in the electron beam current. Care must be exercised in shielding these probes from electrostatic fields.

G. Segmented Faraday Cups

These devices can be used to measure the radial current density profile, and are described in Ref. 5.

---

5. Schuch, R.L., et al., "A Compact Faraday Cup Array for Measurement of Current Distribution from Pulsed Electron Beams," Rev. Sci. Instr., 43, #8, pp. 1097 (1972).

APPENDIX H

MAGNET DESIGN CONSIDERATIONS

The magnetic field necessary for confining the electron beam and controlling the cyclotron wave phase velocity will be generated by a solenoid-type structure. It will be driven by a low voltage capacitor bank, so that the whole system can be treated as a series RLC circuit. Assuming the circuit is under-damped, the winding current is

$$I = \frac{V_o}{\omega_o L}\left(\frac{Q}{\sqrt{Q^2 - 1}}\right) \exp\left(-\omega_o t/Q\right) \sin \omega_o t \sqrt{1 - 1/Q^2} \qquad \text{(H1)}$$

where

L = solenoid inductance

C = capacitance of driver bank

V_o = initial capacitor voltage

R = total series resistance

$$\omega_o = 1/\sqrt{LC}$$

$$Q = \frac{2\sqrt{L/C}}{R}$$

Peak current occurs at

$$t_o = \frac{Q}{\omega_o} \quad \frac{\tan^{-1}\sqrt{Q^2 - 1}}{\sqrt{Q^2 - 1}} \tag{H2}$$

and has amplitude

$$\frac{I_{max}}{\left(\frac{V_o}{\omega_o L}\right)} = \exp\left(-\frac{\tan^{-1}\sqrt{Q^2 - 1}}{\sqrt{Q^2 - 1}}\right) \tag{H3}$$

The conversion efficiency from initially stored capacitor energy to magnetic field energy is

$$\eta = \frac{1/2\ L\ I^2_{max}}{1/2\ C\ V_o^2} = \exp\left(-\ 2\ \frac{\tan^{-1}\sqrt{Q^2 - 1}}{\sqrt{Q^2 - 1}}\right) \tag{H4}$$

The ring-up time to peak current, t_o, should be chosen to be several times the magnetic diffusion time, τ, through

the walls of the vacuum waveguide;

$$\tau = \frac{\mu_o}{\rho} (\Delta t)^2 \tag{H5}$$

where

ρ = electrical resistivity of waveguide material

Δt = wall thickness of waveguide

The intrinsic Q of the solenoid can be estimated from the expression

$$Q_I = 2 \omega_o \frac{(L/\ell)}{(R/\ell)} \tag{H6}$$

where the solenoid is assumed to be made up of (n/ℓ) windings per unit length; each winding has width w and extends from r = a to r = b. The gap between windings is assumed to be negligible. Then

$$\left(\frac{R}{\ell}\right) \simeq \frac{\pi \rho' (b + a)}{w(b - a)} \left(\frac{n}{\ell}\right) \tag{H7}$$

and

$$\left(\frac{L}{\ell}\right) \simeq \pi \mu_o \left(\frac{n}{\ell}\right)^2 a^2 \left\{1 + \frac{1}{2} \frac{(b - a)}{a^2} (a + 1/3\, b)\right\} \tag{H8}$$

where

ρ' = electrical resistivity of winding material.

This gives

$$Q_I \simeq 2\omega_o \frac{\mu_o a^2}{\rho'} w \left(\frac{n}{\ell}\right) \left(\frac{b-a}{b+a}\right)\left\{1+\frac{1}{2}\frac{(b-a)}{a^2}(a+1/3\,b)\right\} \tag{H9}$$

Since

$$\left(\frac{n}{\ell}\right) \simeq \frac{1}{w} \quad . \tag{H10}$$

then finally

$$f = \frac{Q_I}{\left(2\omega_o \frac{\mu_o}{\rho'} a^2\right)} \simeq \left(\frac{x-1}{x+1}\right)\left(1+1/2\,(x-1)\,(x/3+1)\right) \tag{H11}$$

where

$$x = \frac{b}{a} \tag{H12}$$

Assuming

$$x = 1 + \delta \tag{H13}$$

and

$$\delta \ll 1 \tag{H14}$$

then

$$f \simeq \frac{\delta}{2} \tag{H15}$$

and

$$Q_I \simeq \omega_o \frac{\mu_o}{\rho'} a(b-a) \tag{H16}$$

If we set $t_o = 5\tau$, then from Eq. (H2) we have

$$\omega_o \simeq \frac{Q_I}{5 \frac{\mu_o}{\rho} (\Delta t)^2} \quad \frac{\tan^{-1} \sqrt{Q_I^2 - 1}}{\sqrt{Q_I^2 - 1}} \tag{H17}$$

and using Eq. (H16) one obtains

$$\frac{\tan^{-1} \sqrt{Q_I - 1}}{\sqrt{Q_I^2 - 1}} \simeq 5 \frac{\rho'}{\rho} \frac{\Delta t^2}{a(b-a)} \tag{H18}$$

Having chosen a value for Q_I (for example from Eq. (H4)), then Eq. (H18) can be used to size the solenoid.

APPENDIX I

NUMERICAL INVESTIGATION OF MAGNETIC GUIDE FIELD PROFILES

In the Auto-Resonant Accelerator, the phase velocity of the cyclotron wave is determined by the value of the local guide magnetic field. For ions trapped in the wave it is the spatial change in the guide field which thus governs the acceleration process. In this appendix we examine by means of a computer code the effects of various guide field profiles on the ion acceleration process.

Ion Equations of Motion

In Ref. 1 the one dimensional, relativistic ion equations of motion for the test ion (constant wave potential) case have been derived and are given by

$$\frac{1}{c}\frac{du}{dt} = -\frac{e\varphi_o}{mc^2}\gamma^{-3}\,\Omega\sin\psi \qquad (I1)$$

where

$$\psi \equiv \psi_o + \frac{1}{c}\int_o^z \Omega(z')dz' + \frac{\omega}{c}(z - ct) \qquad (I2)$$

is the phase of the wave relative to the ion. In these equations,

$$\gamma \equiv \frac{1}{\sqrt{1 - u^2/c^2}}$$

$$\Omega(z) \equiv \frac{eB(z)}{\gamma_e m_e c}$$ is the electron gyrofrequency

and ω is the angular frequency of the cyclotron wave; φ_o is the (constant) wave potential, e is the unit of electronic charge, and m and m_e are the ion and electron rest masses respectively.

From Eq. (I2) it follows that the wave phase velocity is given by

$$v_\varphi = \frac{\omega}{\omega + \Omega(z)}\,c \qquad (I3)$$

Setting $u = v_\varphi$ so that the ion sits at a constant phase point of the wave (and thus experiences a constant

AD-A033 946 AUSTIN RESEARCH ASSOCIATES INC TEX F/G 20/7
CONCEPTUAL DESIGN OF AN AUTO-RESONANT ACCELERATOR EXPERIMENT.(U)
NOV 76 W E DRUMMOND, G I BOURIANOFF F29601-76-C-0046
UNCLASSIFIED ARA-224 AFWL-TR-76-152 NL

2 OF 4
AD
A033946

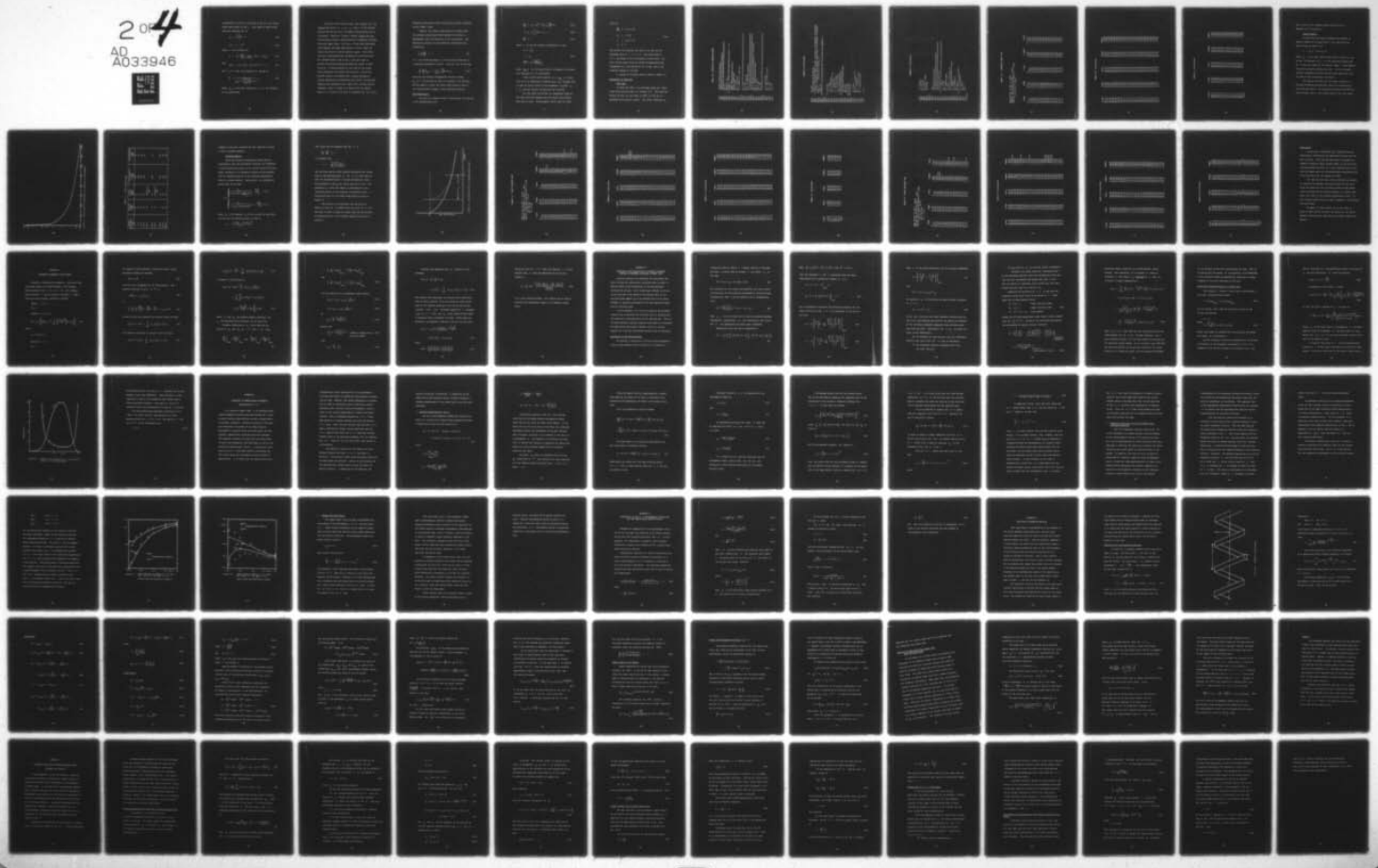

acceleration) yields as a solution of Eq. (I1) the "ideal" guide field given in Ref. 1. This field is again given here for reference and is

$$\Omega_o = \frac{1 - v_\varphi}{v_\varphi} \omega \tag{I4}$$

$$v_\varphi^2 \equiv 1 - x^{-2} \tag{I5}$$

where x is a solution of

$$z = -\frac{c}{\omega}\left(\frac{mc^2}{e\varphi_o}\right)\frac{1}{\sin\psi_o}\left[f(x) - f(x_o)\right] \tag{I6}$$

with

$$f(x) \equiv 2/3 + \frac{1}{3}x^3 + \frac{1}{3}(x^2-1)^{3/2} - x \tag{I7}$$

For $v_\varphi \ll 1$, Eqs. (I4) through (I7) reduce to

$$\frac{\Omega}{\omega} = \frac{1}{v_{\varphi o}\left[1 - \frac{3\alpha \sin\psi_o}{c(v_{\varphi o}/c)^3} z\omega\right]^{1/3}} \tag{I8}$$

where $v_{\varphi o}$ is the wave velocity at $z = 0$, the entrance to the accelerator.

The guide field given by Eqs. (I4) through (I7), for appropriate values of φ_o, ψ_o, v_o, and ω, is the desired profile and the one which the magnet design should strive to achieve. There are, however, several reasons why the field profile actually obtainable may be expected to differ from this ideal field. The first is that since the guide field magnets are made from discrete current loops, we expect the field to exhibit spatial ripple. This effect has been investigated both theoretically and numerically for nonrelativistic ions in Ref. 1 and was found to present no serious problem providing the ripple is kept below 5%. A second problem is just that of the actual coils producing the "wrong" field profile. While this problem could be considered just a ripple problem by fourier analyzing the difference guide field, the previous analysis has considered only ripple with a single fourier component; also, in order to interact with the magnet design it is useful to be able to integrate Eq. (I1) for an

arbitrarily specified guide field profile without reference to the "ideal" field.

Finally, the actual guide field will differ from the constant acceleration field because the latter is nonadiabatic near the beginning of the accelerator. The theoretical analysis on Auto-Resonant acceleration has assumed that

$$\left| \frac{c}{\Omega^2} \frac{d\Omega}{dz} \right| \ll 1 \qquad \text{(I9)}$$

i.e., the fractional change in the cyclotron frequency in a cyclotron wavelength is small. From Eq. (I8) we see that

$$\frac{c}{\Omega^2} \frac{d\Omega}{dz} \bigg|_{z=0} \cong \left(\frac{c}{v_{\varphi o}}\right)^2 \frac{e\varphi_o}{mc^2} \sin \psi_o \ . \qquad \text{(I10)}$$

Since for the usually contemplated injection scheme $v_{\varphi o} \ll c$ we see that Eq. (I9) is violated at the entrance. We thus expect to patch the ideal guide field to that in the linear section through a short adiabatic section.

Code Description

For use in a computer code we rewrite Eqs. (I1) and (I2) in the dimensionless form

$$\frac{du}{dt} = -\left[1 - u^2\right]^{3/2} \frac{\Omega}{\omega}(y) \frac{e\varphi_o}{mc^2} \sin\psi \qquad \text{(I11)}$$

$$\psi = \psi_o + \int_o^y \frac{\Omega}{\omega} dy' + y - \tau \qquad \text{(I12)}$$

$$\frac{dy}{d\tau} = u \qquad \text{(I13)}$$

where u is the ion velocity normalized to c and

$$y \equiv z \frac{\omega}{c}$$

$$\tau \equiv \omega t \qquad \text{(I14)}$$

$$\frac{\Omega(y)}{\omega} = \frac{c}{\omega} \frac{B_{KG}(z)}{(1.707)\gamma_e}$$

where $B_{KG}(z)$ is the guide field in kilogauss to be given as a function of z in centimeters.

Given a guide field profile (i.e., B_{KG} as a function of z) we numerically integrate Eqs. (I11) through (I13) in time for given values of the parameters $e\varphi_o/mc^2$, ψ_o, ω, γ_e and the initial ion position and velocity.

For the cases run we kept all parameters fixed at the same value and changed only the guide field profile from case to case. The parameter values used for those

runs are

$$\frac{e\varphi}{mc^2} = 5.33 \times 10^{-4}$$

$$\psi_o = -0.75 \qquad \text{(I15)}$$

$$\omega = 1.48 \times 10^{9}$$

$$\gamma_e = 7$$

The initial ion velocity was taken to be that of the cyclotron wave at $\tau = 0$, $z = 0$. The guide field at $z = 0$ was taken to be 25 kilogauss in every case. For this initial guide field the choice of parameters used corresponds to a wave potential of 0.5 MeV, and an ion injection energy of 0.25 MeV.

A listing of the basic code is given in table I-1.

Discussion of Cases Run

Test Case

To check the code, a run was made using the "ideal" guide field given by Eqs. (I4) through (I7). The numerical results of this run are shown in table I-2 and are in agreement with analytic theory. For future reference we

TABLE I-1 LISTING OF PROGRAM BSTAB

```
100=       PROGRAM BSTAB(INPUT,OUTPUT)
110=       COMMON/Z101/PHSI0,COW,GAMMA,Z1,ALPHA
120=       COMMON/Z777/FP1,FP2,FP3,FP4,FP5,FP6,FP7,FP8,FP9
130=       KP = 0
140=       GAMMA = 7.0
150=    11 FORMAT( * ENTER EPHI,EION,PHSI0,TL,EF,H * ,//)
160=       PRINT 11
170=       READ *,EPHI,E,PHSI0,TL,EF,H
180=       ALPHA = EPHI/938.
190=       A1 = PHSI0
200=       G0 = 1.+E/938.
210=       U0 = SQRT(1.-1./(G0**2))
220=C
230=C      ***********************************************************
240=       B0 = 25.
250=       U1 = (1.-U0)/U0
260=       COW = (1.707)*GAMMA*U1/B0
270=C      ***********************************************************
280=C      ***********************************************************
390=       FP1 = (G0**3.)/3.+(1./3.)*(G0*G0-1.)**(1.5)-G0
392=       FP2 = -COW/ALPHA/SIN(PHSI0)
394=       FP3 = 1./U1
396=       FP4 = B0
398=       G1 = G0
400=C      ***********************************************************
410=C
420=       NP = 30./H/COW
430=       Z1 = COW/(1.707)/GAMMA
440=       TT = 0.0
450=       X = 0.0
460=       X0 = X
```

TABLE I-1 (Continued)

```
470=       U = UO
480=       PRINT 1,EPHI,E,PHSI0,COW
490=     1 FORMAT(/,5X,*WAVE ENERGY IN MEV = *,G10.4,/,5X,*INITIAL ION ENERGY
500=      1 IN MEV = *,G10.4,/,5X,*INITIAL PHASE ANGLE IN RADIANS = *,G10.4,/
510=      2,5X,*        C/W IN CM = *,G10.4,//)
520=       PRINT 88
530=    88 FORMAT(//,7X,*Z*,14X,*B*,14X,*T*,14X,*E*,14X,*PHASE*,/)
540=C
550=C
560=    50 CONTINUE
570=       Z = X*COW
580=       CALL BZ(Z,B,G1)
590=       IF(KP.NE.0)GO TO 35
600=       T = TT*COW/30.
610=       E = SQRT(1.-U*U)
620=       E = (1./E-1.)*938.
630=       PRINT 10,Z,B,T,E,A1
640=    10 FORMAT(4X,5(G10.4,5X))
650=       IF(E.GT.EF.OR.T.GT.TL)STOP
660=       KP = NP
670=       GO TO 40
680=    35 KP = KP-1
690=    40 CONTINUE
700=C
710=       W = B*Z1
720=       DPHSI = (1.+W)*H*U -H
730=       GF = -W*SIN(A1)
740=       B1 = (1.-U*U)**(1.5)
750=       C1 = H*B1*GF*ALPHA
760=C
770=       XO = X
```

TABLE I-1 (Continued)

```
780=       X = XO+U*H
790=       U = U + C1
800=       TT = TT+H
810=       A1 = A1 + DPHSI
820=       GO TO 50
830=C
840=C
850=       END
860=       SUBROUTINE BZ(Z,B,G1)
870=       COMMON/Z101/PHSI0,COW,GAMMA,Z1,ALPHA
880=       COMMON/Z777/FP1,FP2,FP3,FP4,FP5,FP6,FP7,FP8,FP9
881=       IF(Z.EQ.0.)GO TO 10
890=     5 F = (G1**3.)/3.+(1./3.)*(G1*G1-1.)**(1.5)-G1-FP1
892=       F = F*FP2
894=       DEL = Z-F
896=       D = SQRT(DEL*DEL)
897=       D = D/Z
898=       IF(D.LT.1.E-4)GO TO 10
900=       G = G1*G1+SQRT(G1*G1-1.)*G1-1
902=       G = G*FP2
904=       G1 = G1+DEL/G
906=       GO TO 5
908=    10 U = SQRT(1.-1./(G1*G1))
910=       B = (1.-U)*FP3/U
912=       B = B*FP4
950=       RETURN
960=       END
961=*END
```

TABLE I-2 CONSTANT PHASE RUN

WAVE ENERGY IN MEV = .5000
INITIAL ION ENERGY IN MEV = .2500
INITIAL PHASE ANGLE IN RADIANS = -.7500
C/W IN CM = 20.23

Z (cm)	B (KG)	T (ns)	E (MeV)	PHASE
0.	25.00	0.	.2500	-.7500
.9647	14.29	1.001	.7396	-.7499
2.333	10.99	2.001	1.222	-.7497
4.005	9.235	3.002	1.700	-.7497
5.930	8.102	4.002	2.173	-.7497
8.076	7.295	5.003	2.643	-.7497
10.42	6.683	6.004	3.109	-.7498
12.95	6.197	7.004	3.572	-.7499
15.64	5.800	8.005	4.032	-.7499
18.49	5.468	9.005	4.490	-.7500
21.49	5.185	10.01	4.945	-.7500
24.63	4.939	11.01	5.398	-.7501
27.90	4.724	12.01	5.849	-.7501
31.30	4.533	13.01	6.297	-.7501
34.82	4.362	14.01	6.744	-.7501
38.46	4.208	15.01	7.188	-.7501
42.21	4.069	16.01	7.631	-.7501
46.07	3.941	17.01	8.072	-.7500
50.04	3.824	18.01	8.511	-.7500
54.10	3.717	19.01	8.948	-.7500
58.27	3.617	20.01	9.384	-.7500

TABLE I-2 (Continued)

Z(cm)	B(KG)	T(ns)	E(MeV)	PHASE
62.53	3.524	21.01	9.817	-.7500
66.89	3.438	22.01	10.25	-.7499
71.33	3.357	23.01	10.68	-.7499
75.87	3.281	24.01	11.11	-.7499
80.49	3.210	25.02	11.54	-.7499
85.20	3.143	26.02	11.96	-.7498
89.99	3.080	27.02	12.39	-.7498
94.86	3.020	28.02	12.81	-.7498
99.81	2.963	29.02	13.24	-.7498
104.8	2.909	30.02	13.66	-.7498
109.9	2.857	31.02	14.08	-.7498
115.1	2.808	32.02	14.49	-.7498
120.4	2.762	33.02	14.91	-.7498
125.7	2.717	34.02	15.33	-.7498
131.1	2.674	35.02	15.74	-.7498
136.6	2.633	36.02	16.16	-.7499
142.1	2.594	37.02	16.57	-.7499
147.7	2.556	38.02	16.98	-.7499
153.4	2.520	39.02	17.39	-.7499
159.1	2.484	40.02	17.80	-.7499
164.9	2.451	41.03	18.21	-.7499
170.8	2.418	42.03	18.61	-.7499
176.7	2.387	43.03	19.02	-.7500
182.7	2.357	44.03	19.42	-.7500
188.7	2.327	45.03	19.83	-.7500
194.8	2.299	46.03	20.23	-.7500
201.0	2.272	47.03	20.63	-.7500
207.2	2.245	48.03	21.03	-.7500
213.5	2.220	49.03	21.43	-.7500
219.8	2.195	50.03	21.83	-.7500
226.2	2.170	51.03	22.23	-.7500
232.7	2.147	52.03	22.63	-.7501

TABLE I-2 (Continued)

Z(cm)	B(KG)	T(ns)	E(MeV)	PHASE
239.2	2.124	53.03	23.02	-.7501
245.7	2.102	54.03	23.42	-.7501
252.4	2.080	55.03	23.81	-.7501
259.0	2.059	56.03	24.21	-.7501
265.7	2.039	57.03	24.60	-.7501
272.5	2.019	58.04	24.99	-.7501
279.3	2.000	59.04	25.38	-.7501
286.2	1.981	60.04	25.77	-.7500
293.1	1.962	61.04	26.16	-.7500
300.1	1.944	62.04	26.55	-.7500
307.1	1.927	63.04	26.94	-.7500
314.2	1.910	64.04	27.33	-.7500
321.3	1.893	65.04	27.71	-.7500
328.4	1.877	66.04	28.10	-.7500
335.7	1.861	67.04	28.48	-.7500
342.9	1.845	68.04	28.86	-.7500
350.2	1.830	69.04	29.25	-.7500
357.6	1.815	70.04	29.63	-.7499
365.0	1.800	71.04	30.01	-.7499

STOP

give a plot of the constant phase guide field as a function of z in Figure I1.

Ripple Effects

Several runs were made to examine the effects of spatial ripple on the guide field. For these runs the guide field was taken to be

$$B = B_o(1 + f \sin \xi_o z)$$

where B_o is the ideal guide field given in Figure I1 (or by Eqs. (I4) through (I7)), f is the fractional ripple and ξ_o is the wave number of the spatial ripple. These effects have been analyzed previously in Ref. [1] for the nonrelativistic equations of motion and were done again here just to check on the relativistic correction.

The results of these runs are shown in Table I-3. Although differing qualitatively from the nonrelativistic runs done previously, the qualitative features of stability are the same; that is, for ripple below 5% the ions remain

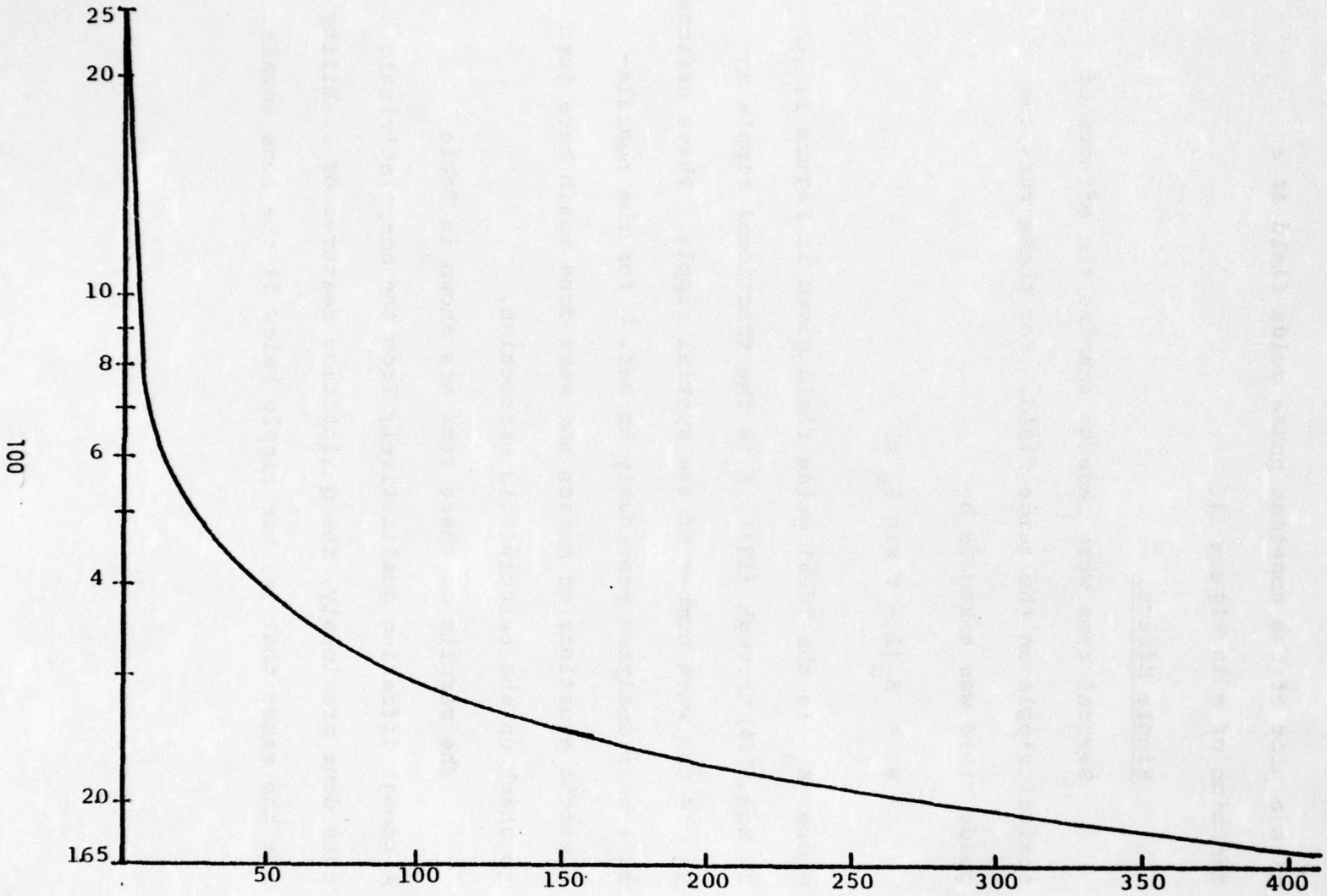

Figure 11. Guide Field in Kilogauss vs. Distance in Centimeters

TABLE I-3. FIELD RIPPLE RUNS

Ripple Wavelength (cm)	Percent Ripple (%)	Final Energy (MeV)	Acceleration Length (cm)	Acceleration Time (ns)
0.3	10	30	365	71
3.0	10	30	365	71
30.0	10	30	347	69
60.0	10	30	396	76
150.0	10	Stability lost		
150.0	5	30	406	77
300.0	10	Stability lost		
300.0	5	30	315	65
600.0	10	30	376	76
1500.0	10	30	473	89

trapped in the wave, although the time required to reach 30 MeV is somewhat greater.

Patching Effects

Since the constant acceleration guide field is nonadiabatic near the accelerator entrance, we considered a guide field which starts at the initial value of 25 kilogauss, decreases in an adiabatic manner and then patches onto an adiabatic portion of the constant acceleration field in a smooth manner. Specifically, we considered a guide field of the form

$$B = \begin{cases} \dfrac{B_o}{(1-u_o)\left[1+\frac{1}{3}\alpha\dfrac{z}{(1+\alpha z_1)^{2/3}}\right]} - \dfrac{B_o u_o}{1-u_o} & z \le \hat{z} \\ \dfrac{B_o}{(1-u_o)\left[1+\alpha z_1+\alpha(z-\hat{z})\right]^{1/3}} - \dfrac{B_o u_o}{1-u_o} & z \ge \hat{z} \end{cases}$$

where B_o = 25 kilogauss, u_o is the initial ion (and wave) velocity and the patching point is given by

$$\hat{z} = \frac{1 + \alpha z_1 - (1 + \alpha z_1)^{2/3}}{1/3\ \alpha}$$

This field has the property that for $z \leq \hat{z}$

$$\frac{c}{\Omega^2} \frac{d\Omega}{dz} \equiv \epsilon$$

is constant with

$$\epsilon = - \frac{(1.707)\ \gamma_e\ \alpha}{3B_o\ (1 + \alpha z_1)^{2/3}}$$

and the field and its first spatial derivation are continuous at the patching point $\hat{z}$. For $z > \hat{z}$, this field is just the (nonrelativistic) constant acceleration field. The parameters α and z_1 are varied from run to run. The parameter z_1 is just the length in centimeters of the truncated portion of the constant acceleration field. A qualitative plot of this model guide field is given in Figure I2 .

The results of the patching runs are given in tables I-4 and I-5. In these runs, the value of $\alpha = 3.35$ was used in order to match the model field at 365 cm from the patching point to the constant phase field given in Figure I1.

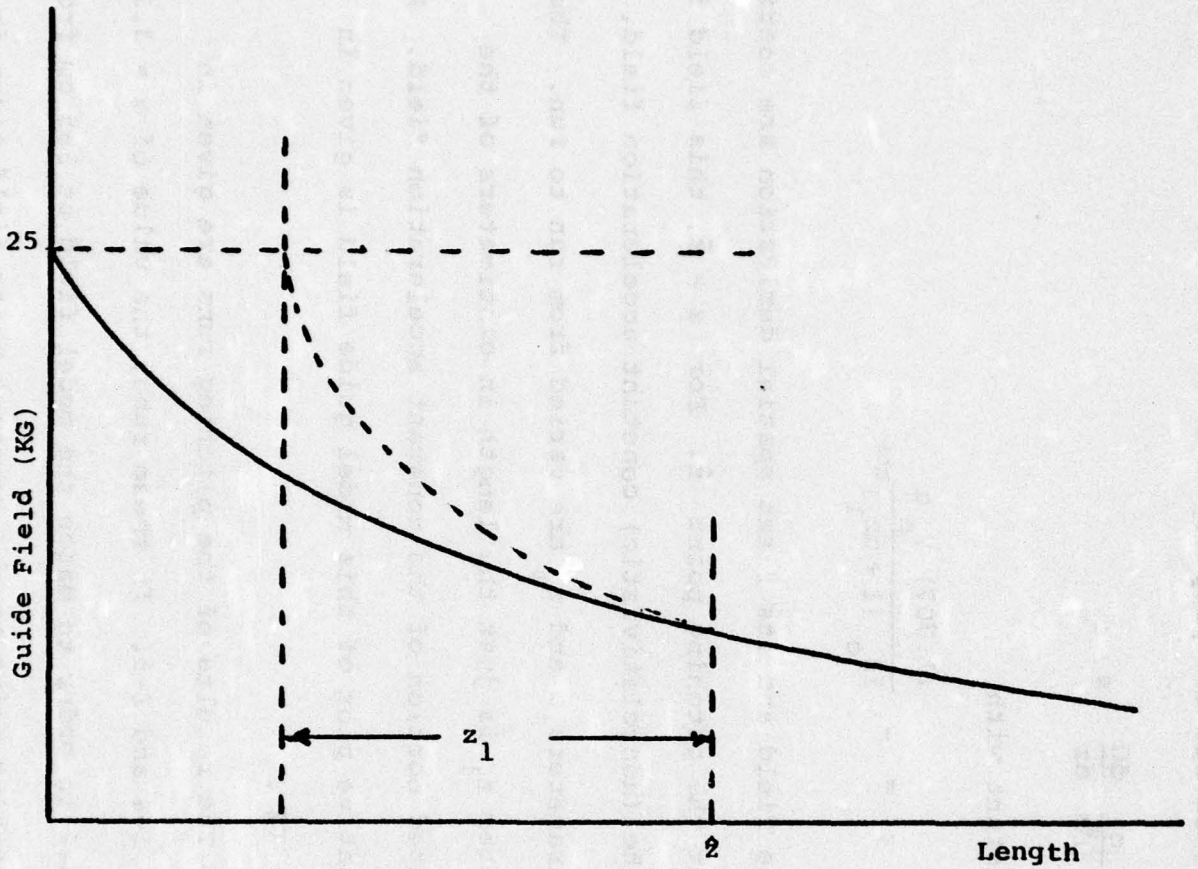

Figure I2. Qualitative Plot of Patched Guide Field

TABLE I-4 FIELD PATCHING RUN

WAVE ENERGY IN MEV = .5000
INITIAL ION ENERGY IN MEV = .2500
INITIAL PHASE ANGLE IN RADIANS = -.7500
C/W IN CM = 20.23
Z1 = 20 cm
α = 3.35

Z (cm)	B (KG)	T (ns)	E (MeV)	PHASE
0.	25.00	0.	.2500	-.7500
.9873	23.41	1.001	.7442	-.1865
2.137	21.79	2.001	.5155	.5590
2.988	20.85	3.002	.1430	.4523
3.319	20.34	4.002	.9924E-01	-.2690
3.935	19.66	5.003	.3711	-.6908
5.012	18.56	6.004	.8474	-.3989
6.359	17.35	7.004	.9418	.2059
7.587	16.37	8.005	.6104	.5154
8.517	15.70	9.005	.3318	.3253
9.262	15.20	10.01	.2859	-.1598
10.09	14.67	11.01	.4823	-.5612
11.22	14.01	12.01	.8812	-.6339
12.67	13.25	13.01	1.299	-.3933
14.32	12.47	14.01	1.482	-.2399E-01
15.99	11.76	15.01	1.373	.2616
17.54	11.17	16.01	1.139	.3435
18.95	10.68	17.01	.9502	.2173
20.27	10.26	18.01	.8953	-.4405E-01
21.61	9.861	19.01	1.002	-.3346
23.07	9.458	20.01	1.263	-.5618
24.74	9.037	21.01	1.642	-.6769

TABLE I-4 (Continued)

Z(cm)	B(KG)	T(ns)	E(MeV)	PHASE
26.62	8.600	22.01	2.083	-.6760
28.72	8.158	23.01	2.520	-.5848
31.00	7.724	24.01	2.893	-.4431
33.41	7.309	25.02	3.165	-.2928
35.91	6.921	26.02	3.332	-.1687
38.45	6.563	27.02	3.423	-.9312E-01
41.02	6.235	28.02	3.477	-.7548E-01
43.60	5.933	29.02	3.537	-.1144
46.22	5.654	30.02	3.634	-.2014
48.88	5.406	31.02	3.792	-.3232
51.61	5.188	32.02	4.023	-.4632
54.43	4.992	33.02	4.329	-.6067
57.36	4.814	34.02	4.704	-.7426
60.42	4.650	35.02	5.141	-.8631
63.63	4.499	36.02	5.626	-.9638
66.97	4.357	37.02	6.149	-1.043
70.47	4.225	38.02	6.700	-1.099
74.11	4.101	39.02	7.271	-1.134
77.90	3.985	40.02	7.854	-1.149
81.83	3.876	41.03	8.444	-1.146
85.90	3.773	42.03	9.035	-1.127
90.10	3.676	43.03	9.622	-1.094
94.43	3.584	44.03	10.20	-1.049
98.88	3.498	45.03	10.76	-.9943
103.4	3.416	46.03	11.30	-.9324
108.1	3.339	47.03	11.82	-.8655
112.9	3.266	48.03	12.31	-.7959
117.7	3.197	49.03	12.76	-.7258
122.7	3.132	50.03	13.18	-.6572
127.7	3.069	51.03	13.56	-.5922
132.8	3.011	52.03	13.90	-.5335
137.9	2.955	53.03	14.21	-.4795

TABLE I-4 (Continued)

Z (cm)	B (KG)	T (ns)	E (MeV)	PHASE
143.1	2.902	54.03	14.49	-.4345
148.3	2.851	55.03	14.75	-.3983
153.6	2.803	56.03	14.98	-.3716
159.0	2.758	57.03	15.20	-.3545
164.3	2.714	58.04	15.41	-.3472
169.7	2.672	59.04	15.62	-.3492
175.1	2.632	60.04	15.83	-.3602
180.6	2.594	61.04	16.04	-.3795
186.1	2.557	62.04	16.27	-.4061
191.6	2.522	63.04	16.51	-.4393
197.2	2.487	64.04	16.77	-.4780
202.9	2.454	65.04	17.05	-.5212
208.5	2.423	66.04	17.35	-.5678
214.2	2.392	67.04	17.67	-.6168
220.0	2.362	68.04	18.01	-.6673
225.8	2.333	69.04	18.38	-.7183
231.7	2.305	70.04	18.76	-.7690
237.7	2.278	71.04	19.17	-.8188
243.7	2.251	72.04	19.60	-.8669
249.7	2.225	73.04	20.04	-.9130
255.9	2.200	74.05	20.49	-.9564
262.1	2.175	75.05	20.97	-.9969
268.4	2.151	76.05	21.45	-1.034
274.7	2.128	77.05	21.94	-1.068
281.1	2.105	78.05	22.44	-1.099
287.6	2.082	79.05	22.95	-1.126
294.2	2.060	80.05	23.47	-1.149
300.8	2.039	81.05	23.99	-1.169
307.5	2.018	82.05	24.51	-1.185
314.3	1.997	83.05	25.04	-1.197
321.1	1.977	84.05	25.57	-1.207
328.0	1.958	85.05	26.10	-1.213

TABLE I-4 (Continued)

Z(cm)	B(KG)	T(ns)	E(MeV)	PHASE
335.0	1.938	86.05	26.64	-1.215
342.0	1.919	87.05	27.17	-1.215
349.1	1.901	88.05	27.70	-1.212
356.3	1.883	89.05	28.23	-1.206
363.5	1.865	90.05	28.76	-1.198
370.9	1.847	91.06	29.29	-1.187
378.2	1.830	92.06	29.81	-1.174
385.6	1.814	93.06	30.33	-1.159
STOP				

TABLE I-5 FIELD PATCHING RUN

WAVE ENERGY IN MEV = .5000
INITIAL ION ENERGY IN MEV = .2500
INITIAL PHASE ANGLE IN RADIANS = -.7500
C/W IN CM = 20.23
Z1 = 40.0 cm
α = 3.35

Z(cm)	B(KG)	T(ns)	E (MeV)	PHASE
0.	25.00	0.	.2500	-.7500
.9876	23.97	1.001	.7414	-.1620
2.114	22.89	2.001	.4625	.6192
2.783	22.30	3.002	.9236E-01	.4317
3.131	22.00	4.002	.8252E-01	-.3899
3.764	21.48	5.003	.4246	-.6916
4.891	20.60	6.004	.8512	-.1351
6.124	19.72	7.004	.6319	.5213
7.009	19.13	8.005	.2345	.5201
7.550	18.79	9.005	.1230	-.7850E-01
8.143	18.43	10.01	.3009	-.6110
9.124	17.86	11.01	.7430	-.5573
10.45	17.14	12.01	1.034	-.2565E-01
11.81	16.46	13.01	.8125	.4613
12.90	15.95	14.01	.4436	.5050
13.70	15.59	15.01	.2662	.1149
14.43	15.28	16.01	.3352	-.3859
15.38	14.90	17.01	.6442	-.6273
16.66	14.40	18.01	1.074	-.4782
18.19	13.85	19.01	1.327	-.7309E-01
19.77	13.33	20.01	1.211	.3134

TABLE I-5 (Continued)

Z(cm)	B(KG)	T(ns)	E(MeV)	PHASE
21.19	12.88	21.01	.8999	.4618
22.40	12.53	22.01	.6416	.3196
23.45	12.24	23.01	.5531	-.1796E-01
24.52	11.95	24.01	.6613	-.3720
25.75	11.64	25.02	.9496	-.5798
27.23	11.28	26.02	1.347	-.5723
28.95	10.89	27.02	1.718	-.3779
30.82	10.50	28.02	1.915	-.9123E-01
32.74	10.12	29.02	1.877	.1710
34.59	9.780	30.02	1.683	.3192
36.32	9.480	31.02	1.456	.3171
37.94	9.215	32.02	1.294	.1790
39.49	8.973	33.02	1.251	-.4461E-01
41.06	8.741	34.02	1.348	-.2864
42.73	8.506	35.02	1.577	-.4843
44.56	8.262	36.02	1.911	-.5987
46.56	8.009	37.02	2.306	-.6170
48.75	7.748	38.02	2.707	-.5487
51.10	7.486	39.02	3.058	-.4187
53.57	7.227	40.02	3.311	-.2597
56.12	6.978	41.03	3.447	-.1056
58.69	6.741	42.03	3.478	.1555E-01
61.27	6.518	43.03	3.439	.8554E-01
63.82	6.311	44.03	3.373	.9709E-01
66.35	6.117	45.03	3.321	.5259E-01
68.86	5.934	46.03	3.314	-.3836E-01
71.39	5.761	47.03	3.374	-.1616
73.95	5.594	48.03	3.513	-.3015
76.58	5.431	49.03	3.734	-.4431
79.30	5.272	50.03	4.031	-.5743
82.13	5.115	51.03	4.395	-.6868
85.09	4.959	52.03	4.813	-.7760

TABLE I-5 (Continued)

Z (cm)	B (KG)	T (ns)	E (MeV)	PHASE
88.19	4.806	53.03	5.271	-.8408
91.43	4.654	54.03	5.759	-.8824
94.81	4.504	55.03	6.264	-.9036
98.34	4.357	56.03	6.778	-.9084
102.0	4.219	57.03	7.294	-.9001
105.8	4.091	58.04	7.806	-.8808
109.7	3.972	59.04	8.308	-.8529
113.7	3.862	60.04	8.798	-.8182
117.8	3.758	61.04	9.270	-.7790
122.1	3.662	62.04	9.723	-.7373
126.4	3.571	63.04	10.15	-.6950
130.9	3.486	64.04	10.56	-.6538
135.4	3.407	65.04	10.95	-.6151
139.9	3.332	66.04	11.31	-.5804
144.6	3.261	67.04	11.65	-.5505
149.3	3.194	68.04	11.98	-.5263
154.1	3.131	69.04	12.29	-.5083
158.9	3.071	70.04	12.59	-.4966
163.8	3.014	71.04	12.89	-.4914
168.8	2.960	72.04	13.18	-.4925
173.8	2.908	73.04	13.47	-.4995
178.9	2.859	74.05	13.77	-.5119
184.0	2.812	75.05	14.07	-.5293
189.1	2.767	76.05	14.38	-.5509
194.4	2.724	77.05	14.70	-.5760
199.7	2.683	78.05	15.03	-.6038
205.0	2.643	79.05	15.38	-.6338
210.4	2.604	80.05	15.74	-.6651
215.9	2.567	81.05	16.11	-.6972
221.4	2.532	82.05	16.50	-.7293
227.0	2.497	83.05	16.89	-.7610
232.6	2.463	84.05	17.31	-.7917

TABLE I-5 (Continued)

Z (cm)	B (KG)	T (ns)	E (MeV)	PHASE
238.3	2.431	85.05	17.73	-.8212
244.1	2.400	86.05	18.16	-.8489
250.0	2.369	87.05	18.61	-.8746
255.9	2.339	88.05	19.06	-.8981
261.9	2.310	89.05	19.52	-.9193
268.0	2.282	90.05	19.99	-.9380
274.1	2.255	91.06	20.46	-.9541
280.3	2.228	92.06	20.93	-.9676
286.6	2.202	93.06	21.42	-.9785
292.9	2.177	94.06	21.90	-.9869
299.3	2.153	95.06	22.38	-.9929
305.8	2.129	96.06	22.87	-.9964
312.4	2.105	97.06	23.36	-.9976
319.0	2.082	98.06	23.84	-.9967
325.6	2.060	99.06	24.33	-.9938
332.4	2.038	100.1	24.81	-.9890
339.2	2.017	101.1	25.29	-.9825
346.0	1.996	102.1	25.77	-.9744
353.00	1.976	103.1	26.25	-.9650
360.0	1.956	104.1	26.72	-.9543
367.0	1.936	105.1	27.18	-.9427
374.1	1.917	106.1	27.65	-.9301
381.3	1.899	107.1	28.10	-.9170
388.5	1.881	108.1	28.55	-.9033
395.8	1.863	109.1	29.00	-.8893
403.1	1.845	110.1	29.44	-.8752
410.4	1.828	111.1	29.87	-.8611
417.9	1.812	112.1	30.29	-.8472
STOP				

Conclusions

We now have a code which will integrate the one dimensional, relativistic ion equations of motion for the test ion case. This code has been used to evaluate the effects of spatial ripple (single modes) on the ion acceleration process and shows (as in the nonrelativistic case) that for ripple below 5%, we obtain stable acceleration up to the desired final ion energy of 30 MeV.

The code has also been used to evaluate the effects of inserting an adiabatic patching section in the guide field and shows that for the models tested we may obtain stable acceleration by patching smoothly to a guide field which lies close to the constant acceleration field. In all of these cases there is a small increase in acceleration time and length.

We expect to make further use of this code in order to more closely evaluate the effects of the actual magnetic field profile supplied by the magnet vendors and designs.

APPENDIX J

ESTIMATE OF MAGNETIC FIELD RIPPLE

Consider a cylindrically symmetric, infinitely long solenoidal magnet with hoop windings. The windings extend radially from $r = a$ to $r = b$; the windings have thickness w and are spaced a distance δ apart. There are three regions, defined as follows:

Region I $\quad r \leq a$

$$\vec{J} = 0$$

Region II $\quad a \leq r \leq b$

$$\vec{J} = J_o \hat{\theta} \left\{ \frac{w}{w+\delta} + \frac{2}{\pi} \sum_{n=1}^{\infty} \left(\frac{\sin k_n \frac{w}{2}}{n} \right) \cos k_n Z \right\} \qquad (J1)$$

where

$$k_n = 2\pi n/(w+\delta)$$

Region III $\quad r \geq b$

$$\vec{J} = 0$$

The magnetic field produced is derivable from a vector potential through the equation

$$\vec{B} = \vec{\nabla} \times \vec{A} \tag{J2}$$

with only the θ-component of $\vec{A}$ being nonzero. The equation relating $A_\theta(r,z)$ to $\vec{J}$ is

$$(\nabla^2 \vec{A})_\theta = - \mu_o J_\theta(r,z) \tag{J3}$$

or

$$\frac{1}{r} \frac{\partial}{\partial r} \left(r \frac{\partial A_\theta}{\partial r} \right) + \frac{\partial^2 A_\theta}{\partial z^2} - \frac{A_\theta}{r^2} = - \mu_o J_\theta(r,z) \tag{J4}$$

In each of the three regions the solution takes the form

$$A_\theta(r,z) = f(r) + \sum_{n=1}^{\infty} a_n g_n(k_n r) \cos k_n z \tag{J5}$$

with specific solutions in regions I and III being

$$A_I(r,z) = A_o r + \sum_{n=1}^{\infty} A_n I_1(k_n r) \cos k_n z \tag{J6}$$

$$A_{III}(r,z) = \frac{D_o}{r} + \sum_{n=1}^{\infty} D_n K_1(k_n r) \cos k_n z \qquad (J7)$$

In region II the solution is

$$A_{II}(r,z) = B_o r + \frac{C_o}{r} - \frac{1}{3} \mu_o J_o \frac{w}{w+\delta} r^2$$

$$+ \sum_{n=1}^{\infty} \left\{ B_n I_1(k_n r) + C_n K_1(k_n r) \right.$$

$$\left. - \mu_o J_o \frac{\sin k_n \frac{w}{2}}{n k_n^2} L_1(k_n r) \right\} \cos k_n z \qquad (J8)$$

where I_1 and K_1 are modified Bessel functions, and L_1 the modified Struve function, all of order one.

Boundary conditions on A_θ arise from the continuity of B_r and B_z at $r = a$ and $r = b$. Thus,

$$\left.\frac{\partial A_I}{\partial z}\right|_{r=a} = \left.\frac{\partial A_{II}}{\partial z}\right|_{r=a} \quad \text{and} \quad \left.\frac{\partial A_{II}}{\partial z}\right|_{r=b} = \left.\frac{\partial A_{III}}{\partial z}\right|_{r=b} \qquad (J9)$$

$$\frac{1}{r}\ \frac{\partial}{\partial r}\ (r\ A_I)\Big|_{r=a} = \frac{1}{r}\ \frac{\partial}{\partial r}\ (r\ A_{II})\Big|_{r=b}$$

and

$$\frac{1}{r}\ \frac{\partial}{\partial r}\ (r\ A_{II})\Big|_{r=b} = \frac{1}{r}\ \frac{\partial}{\partial r}\ (r\ A_{III})\Big|_{r=b} \tag{J10}$$

For the terms with no z-dependence there obtains

$$2\ A_o = 2\ B_o - \mu_o\ J_o\ \frac{w}{w+\delta}\ a \tag{J11}$$

$$0 = 2\ B_o - \mu_o\ J_o\ \frac{w}{w+\delta}\ b \tag{J12}$$

or

$$A_o = \frac{\mu_o}{2}\ \frac{J_o\ w(b-a)}{w+\delta} \tag{J13}$$

Noting that

$$\left(\frac{I}{\ell}\right) = \frac{J_o\ w(b-a)}{w+\delta} = \text{number of ampere turns per unit length} \tag{J14}$$

then

$$A_o = \frac{\mu_o}{2}\ \left(\frac{I}{\ell}\right) \tag{J15}$$

Consider the expression for B_z interior to the windings:

$$B_I(r,z) = \frac{1}{r} \frac{\partial}{\partial r} (r A_I)$$

$$= \mu_o \left(\frac{I}{\ell}\right) + \sum_{n=1}^{\infty} k_n A_n I_o(k_n r) \cos k_n z \quad \text{(J16)}$$

The leading term represents the uniform field associated with an ideal solenoid, while the remaining terms correspond to the rippling produced by the finite gap between windings. Also, $I_o(x)$ increases rapidly as x increases ($I_o(x=o) = 1$). Thus, the A_n terms should be kept small to minimize ripple throughout the beam. These terms are defined by the boundary conditions, and one can show that

$$k_n A_n = \mu_o \left(\frac{I}{\ell}\right) \frac{(w+\delta)^2}{2\pi\, w(b-a)} \frac{\sin k_n \frac{w}{2}}{n^2}$$

$$\times \left(F(x = k_n b) - F(x = k_n a)\right) \quad \text{(J17)}$$

where

$$F(x) = \frac{L_o(x)\, K_1(x) - L_1(x)\, K_o(x)}{I_o(x)\, K_1(x) - I_1(x)\, K_o(x)} \quad \text{(J18)}$$

Retaining only the $n = 1$ term, and assuming δ is much smaller than w, then the amplitude of the on-axis ripple is

$$A_o \simeq \frac{1}{2} (\delta/w) \quad \frac{\left\{ F\left(2\pi \frac{b}{w+\delta}\right) - F\left(2\pi \frac{a}{w+\delta}\right) \right\}}{\left(\frac{b-a}{w+\delta}\right)} \qquad \text{(J19)}$$

For a given solenoid design, this formula can be used to calculate the percentage ripple in the magnetic guide field.

APPENDIX K

COUPLING TO THE RELATIVISTIC CYCLOTRON EIGENMODE THROUGH AN EXTERNAL AZIMUTHAL CURRENT LOOP

Previous analysis has indicated the requirement for phase locking the relativistic cyclotron mode in order to prevent phase jitter deleterious to the Auto-Resonant acceleration process. More conventional methods of utilizing RF cavities to HF modulate the electron beam in the cyclotron mode appear not to be feasible due to the large mismatch in parallel wavelength of the free space RF signal and the cyclotron mode.

In this appendix, the use of an external HF azimuthal current loop to generate the cyclotron wave is examined and the electrical characteristics of the loop derived. The use of other possible coupling elements which might be convenient for specialized wave-growth regions--such as a helical coupler for a helical wave-growth section--was not examined.

Derivation of the Beam Response

We consider a relativistic cyclotron beam propagating along a guide magnetic field interior to a cylindrical

conducting guide of radius a. Assume interior to the guide and beam, a current loop of current I and radius r_o of the form

$$\vec{J} = \hat{\theta}\ I\delta(r - r_o)\ \delta(z)\ \exp(-i\omega t) \tag{K1}$$

The inclusion of this source term modifies the usual governing equations for the electron beam-magnetic field-wave guide configuration (Ref. 1) by the addition of an inhomogeneous term:

$$\Box\psi^{\pm} = \frac{\omega_p^2\ (k - \omega)}{k - \omega \pm \Omega}\ \psi^{\pm} \pm 2\pi i\ I\ \delta(r - r_o) \tag{K2}$$

Here ω_p, Ω are the relativistic electron plasma and cyclotron frequencies, respectively; k, the longitudinal wave vector, and $\psi^{\pm}$, the appropriate cyclotron wave eigenmodes.

Appropriate solutions may be expressed as

$$\psi^{\pm} = -\frac{\pi}{2}\left[J_1^{\pm}\int_r^a r' Y_1^{\pm'}\ Q^{\pm'}\ dr' - Y_1^{\pm}\int_o^r r' J_1^{\pm'}\ Q^{\pm'}\ dr'\right] + \left(\frac{\alpha}{\beta}\right) J_1^{\pm} \tag{K3}$$

where $J_1^{\pm} \equiv J_1(\xi^{\pm} r)$; $Y_1^{\pm} \equiv Y_1(\xi^{\pm} r)$ and $Q^{\pm} \equiv \pm 2\pi i I$,

with the constants α and β determined from the usual requirements of a conducting boundary at $r = a$:

$$E_\theta = 0 \Rightarrow \psi^+ - \psi^- \Big|_{r=a} = 0$$

$$E_z = 0 \Rightarrow \frac{1}{r} \partial_r \left[r(\psi^+ + \psi^-) \right] \Big|_{r=a} = 0 \qquad \text{(K4)}$$

Use of appropriate recursion and Wronskian relations for the Bessel functions allow α, β to be expressed in the following form:

$$\alpha = -\frac{\pi}{2} \left[\frac{P^+ Y_1^+}{J_1^+} + \frac{2}{\pi a} \frac{\left(\frac{P^+}{J_1^+} - \frac{P^-}{J_1^-} \right)}{J_1^+ D} \right] \Bigg|_{r=a} \qquad \text{(K5)}$$

$$\beta = -\frac{\pi}{2} \left[-\frac{P^- Y_1^-}{J_1^-} + \frac{2}{\pi a} \frac{\left(\frac{P^+}{J_1^+} - \frac{P^-}{J_1^-} \right)}{J_1^- D} \right] \Bigg|_{r=a} \qquad \text{(K6)}$$

Here D is the usual determinant of the cyclotron eigenmodes:

$$D = \left[\frac{\xi^+ J_o^+}{J_1^+} + \frac{\xi^- J_o^-}{J_1^-} \right] \Bigg|_{r=a} \tag{K7}$$

and

$$P^{\pm} = i\, 2\pi\, I\, r_o\, J_1(\xi^{\pm} r_o)$$

The quantity A_θ is found from the usual Fourier inversion of ψ^+, ψ^-:

$$A_\theta = - i\, \psi^+ + i\, \psi^- \tag{K8}$$

In Eq. (K3), the first two terms represent contributions to the local loop response and hence do not affect the structure of the cyclotron eigenmode propagated down the wave guide away from the loop. Furthermore, for $r = r_o$, the first two terms vanish identically.

For our purposes we need evaluate only the contribution from the last term of Eq. (K3) in order to determine:

(1) The eigenmode response propagated away from the loop, and also

(2) The value of A_θ at the loop (which is required to determine the loop's electrical characteristics).

In the following analysis, only the contributions from this last term are considered--the reader must bear in mind that the result is rigorously valid either only well downstream from the loop or at radius $r = r_o$.

Examining the structure of α, β, we see that the eigenvalue poles arise solely from zeroes of D. These modes are of three general types:

$$\begin{aligned} &(1)\quad \xi^+ a \sim 0 && \text{(Lower cyclotron mode)} \\ &(2)\quad \xi^- a \sim 0 && \text{(Upper cyclotron mode)} \\ &(3)\quad \xi^+ a \sim \xi^- a \equiv \xi a && \text{(Light modes)} \end{aligned} \tag{K9}$$

Making use of these approximate modes (which clearly separate only for $\omega_p^2 < k^2 c^2$), we obtain the following prescription for performing the spatial Fourier inversion:

$$A_\theta = \frac{i}{a}\left(\frac{P^+}{J_1^+(a)} - \frac{P^-}{J_1^-(a)}\right)\left(\frac{J_1^+(r)}{J_1^+(a)} - \frac{J_1^-(r)}{J_1^-(a)}\right)\frac{1}{D}\Bigg|_{\substack{\text{cyclotron} \\ \text{poles of } D}}$$

$$+ \pi i \left.\frac{J_1(\xi r)\, PY_1(\xi a)}{J_1(\xi a)}\right|_{\substack{\xi^+ = \xi^- \equiv \xi \\ \text{light modes of } J_1(\xi a)}} \tag{K10}$$

Performing these inversions is straightforward, albeit tedious. More generally, if we consider N loops at locations z and current I_n upstream of z, then A_θ is found by simple superposition:

$$A_\theta(r) = \sum_{n=0}^{N} \frac{4\pi}{c} I_n \left(t - \frac{z - z_n}{c}\right) \frac{r_o}{a} \left[1.6\, J_1(3.8\, r/a)\right.$$

$$\times J_1(3.8\, r_o/a)\, \exp\left(-3.8\, |z - z_n|/a\right)$$

$$+ \frac{\omega_p^2\, c^2}{(k_\perp^2 c^2 + \omega_p^2)^2\, a^2} \frac{\Omega a}{c} \left(\frac{r_o}{a} - \frac{J_1(2.9\, r_o/a)}{0.357}\right)$$

$$\left. \times \left(\frac{r}{a} - \frac{J_1(2.9\, r/a)}{0.357}\right) \sin \Omega(z - z_n)/c \right] \qquad \text{(K11)}$$

where $k_\perp a = 2.9$. Note that only the contribution from the lowest Bessel root of $J_1(\xi a)$ has been retained. For a more accurate solution, all the roots should be retained and the resultant series summed. Such a solution would then yield the exact calculation of vacuum self inductance of a loop interior to a conducting guide, and the response would depend

on the diameter of the wire constituting the loop. Here, by utilizing only the lowest ξa contribution, we are restricted to the situation where the geometrical inductance is large compared to the self inductance of the wire.

Electrical Characteristics of a Single Loop

The voltage V around a single loop is calculated in the usual straightforward manner:

$$V = 2\pi r_o E_\theta \Big|_{z=o} = 2\pi\, i r_o \frac{\omega}{c} A_\theta \Big|_{z=o} \tag{K12}$$

We see from Eq. (K11) that the solution is given by the vacuum contribution.

$$V \cong L \dot{I}$$

where

$$L \cong \frac{8\pi^2 r_o^2}{c^2 a} \left[1.6\, J_1^2(3.8\, r_o/a)\right] \tag{K13}$$

Again, the reader is reminded that this solution only retains the lowest ξa contribution.

Another important electrical characteristic is the value of potential of the eigenmode (evaluated at $z = 0$, $r = 0$) compared to the driving voltage in the current loop. This

may be calculated in a straightforward manner by solving for A_r and then evaluating $|\varphi|$ from the relation:

$$i(k_z c - \omega)\ \varphi = -\frac{\partial A_r}{\partial r} \tag{K14}$$

Proceeding in this manner, we find:

$$|\varphi(r = z = 0)| \cong \frac{32\pi}{c}\ I\ \frac{r_o}{a}\ \frac{\omega_p^2\ c^2}{(k_\perp^2 c^2 + \omega_p^2)^2\ a^2}\left(\frac{r_o}{a} - \frac{J_1(2.9 r_o/a)}{0.357}\right) \tag{K15}$$

so that this ratio, denoted by ϵ, is given by:

$$\epsilon \equiv \frac{|\varphi|}{V} \cong 5 \times 10^{-3}\ \frac{I_e}{Ba}\ \frac{c}{v_\varphi}\left|\frac{\frac{r_o}{a} - J_1(2.9\ r_o/a)/0.357}{\left(\frac{r_o}{a}\right)^2 J_1^2(3.8\ r_o/a)}\right| \tag{K16}$$

where I_e is the beam current in kiloamperes; B, the guide magnetic field in kilogauss; a, the beam radius in centimeters and $v_\varphi/c \equiv \omega/\Omega$ is the ratio of phase velocity of the wave to the speed of light.

In Figure K1 the value of ϵ and the characteristic inductance L of the loop is plotted as a function of loop radius. It will be noted that as the loop is taken close to

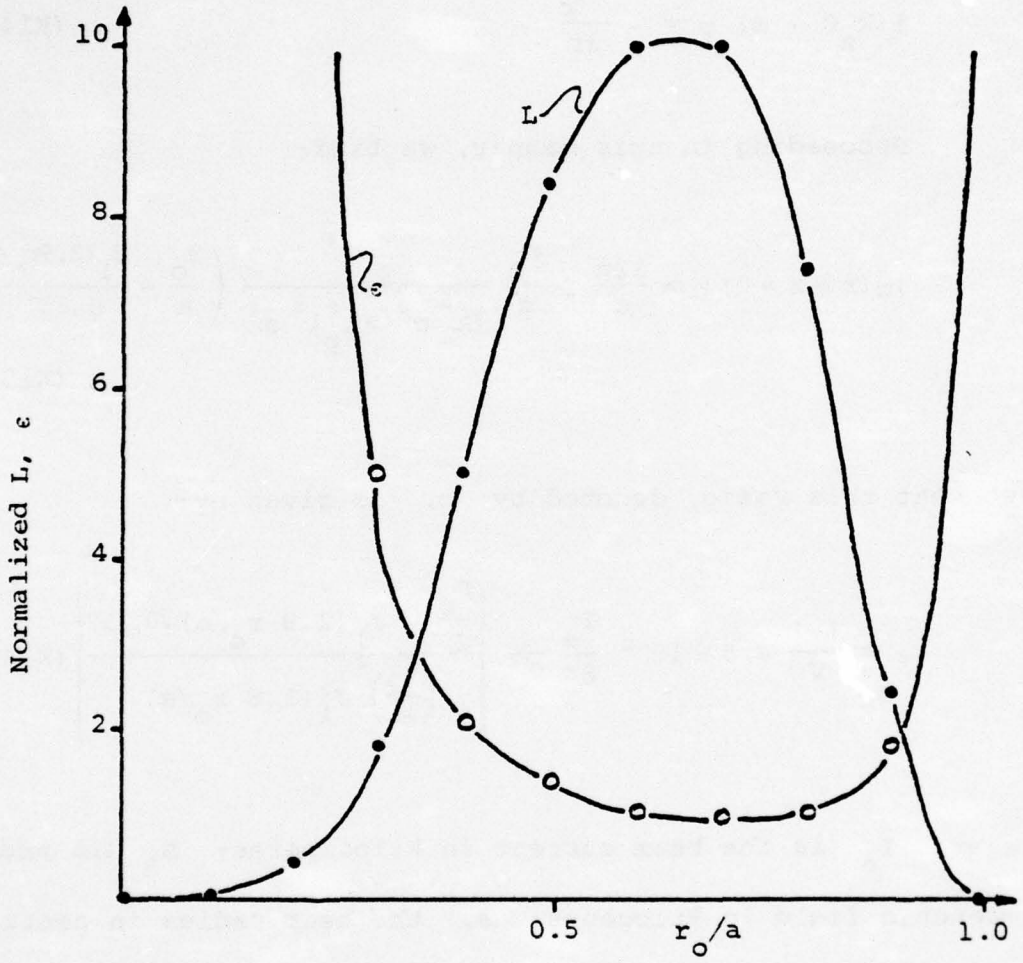

Figure K1: Variation of Inductance (K) and Potential Ratio (ε) with Loop Radius

the conducting wall, the ratio of ϵ improves, but at the expense of the loop inductance. (This decrease in loop inductance is due to the conducting wall acting like a shorter secondary winding.) The value of $r_o/a \cong 0.7$ maximizes total loop inductance at a value of $L = 13a$ nh.

For the proposed ARA experiment utilizing a 30 kA 3 MeV, 1 cm radius electron beam machine in a 24 kG magnetic field with $\omega \cong 1.5 \times 10^9$, the value of ϵ for $r_o/a \cong 0.7$ can be calculated to be

$$\epsilon = 2.2 \tag{K17}$$

APPENDIX L

SOLUTIONS TO SHEATH HELIX DISPERSION RELATION FOR m = 0, 1

In a previous report (Ref. 1) the arbitrary mode number dispersion relation has been derived for a relativistic electron beam drifting through a sheath helix cylindrical conductor. Analytic solutions to the relation describing the growth of low phase velocity axisymmetric cyclotron waves have been found, and preliminary computational solutions have been reported. This appendix presents the analytical solutions found for both the axisymmetric and kink modes as well as the confirming computational results. A stabilizing influence on the m = 1 kink mode caused by increasing the helix pitch angle and the magnetic field strength is demonstrated. It is shown that the sheath helix liner

configuration allows rapid growth of the axisymmetric cyclotron wave which is needed for Auto-Resonant acceleration of ions. However, this growth mechanism is suitable only if used in conjunction with an additional active mechanism which initially excites axisymmetric oscillations in the electron beam before it enters the growth section. This is necessary because the $m = 1$ "kink" mode grows at a slightly greater rate than the desired $m = 0$ mode. Thus, the wave exciter must give the $m = 0$ mode a sufficiently larger initial amplitude than the $m = 1$ mode so that after the $m = 0$ mode has e-folded several times to the amplitude necessary for ion trapping, the $m = 1$ mode will not yet have grown large enough to be disruptive.

The analytic solutions to the sheath helix dispersion relation for modes $m = 0, 1$ are given in Section A. The relative growth rates and phase velocities of these modes are examined. Section B gives details of the computational methods used to solve the exact dispersion relation. A comparison of the numerical and

analytic solutions is presented. A comparison of the sheath helix and resistive liners is made in Section C. Possible improvements of the sheath helix liner are also discussed.

A. Analytic Solutions for $qa > 1$

The full electromagnetic dispersion relation for waves in a relativistic electron beam propagating inside a sheath helix liner has been shown to be

$$(\psi^+ - \psi^-)\,[K^{+2}\,\omega^2 - (mk/qa + q\tan\theta)^2] + 2\,qa\,K^+[\omega^2 + \omega\beta(\psi^+ + \psi^-) + \beta^2\,\psi^+\,\psi^-] = 0 \tag{L1}$$

where

$$\psi^{\pm} = \frac{\xi^{\pm} a\, J_m(\xi^{\pm} a)}{J_{m\pm1}(\xi^{\pm} a)}$$

$$K^+ = \frac{K_{m+1}(qa) + K_{m-1}(qa)}{2\,K_m(qa)}$$

$$\beta = \frac{m(k+\omega)}{q^2a^2} + \frac{\tan\theta}{a}$$

$$q^2 = k^2 - \omega^2 \; ; \quad \xi^{\pm 2} = -q^2 + \frac{\omega_p^2 (k-\omega)}{\omega - k \mp \Omega}$$

Preliminary analysis of Eq. (L1) has revealed solutions for low phase velocity axisymmetric waves. These results are valid for small pitch angles. It was shown that as the pitch angle of the helix was increased the phase velocity and wavenumber of the most unstable wave increased, resulting in an increase in the value of the parameter q, the argument of the Bessel functions. Thus, to extend this analysis to moderate and large pitch angles the large argument expansions of the Bessel functions are taken.

The small ω_p^2 case is considered such that the ω_p^2 corrections to $\xi^{\pm 2}$ are retained only near resonance with the negative energy cyclotron wave, $\omega = kc - \Omega + \epsilon$, where $\epsilon \ll \Omega$.

Using the Bessel function approximations a simplified equation for waves on the helix is obtained with a correction term describing the effect of the beam on the wave.

Thus, the dispersion relation becomes

$$\frac{4q}{\cos^2\theta}\left[\omega^2 - k^2\sin^2\theta - \frac{m\cos^2\theta}{2}\left(1 + \frac{k^2}{q^2} + 4k\tan\theta\right)\right]$$

$$+ \frac{\omega_p^2\,\Omega}{2q\epsilon}\left[-\left(\omega^2 - (mk/q + q\tan\theta)^2\right) + 2q\omega\beta + 2q^2\beta^2\right] = 0 \qquad \text{(L2)}$$

The free modes on the helix are described by the zero beam density dispersion relation

$$\omega^2 = k^2\sin^2\theta + \frac{m\cos^2\theta}{2}\left(1 + k^2/q^2 + 4k\tan\theta\right) \qquad \text{(L3)}$$

These modes can couple with the beam cyclotron modes, $\omega \cong k - \Omega$, only in those regions where the ω, k for the two modes coincide.

The exact values of ω, k at resonance for the axisymmetric mode are

$$\omega = k \sin\theta \tag{L4}$$

and

$$k = \frac{\Omega}{1 - \sin\theta} \tag{L5}$$

An approximate solution for higher m modes may be obtained for $m/2q^2a^2 \ll 1$ and $\cos^2\theta/2 \ll 1$, where one finds

$$\omega_m = \frac{\Omega \sin\theta + m\cos\theta}{(1 - \sin\theta)} \tag{L6}$$

$$k_m = \frac{\Omega + m\cos\theta}{1 - \sin\theta} \tag{L7}$$

It is noted that the crossing conditions for the axisymmetric mode, given by Eqs. (L4) and (L5), are identical to those obtained previously for low phase velocity waves.

The maximum growth rate for the unstable waves may now be obtained by examining the imaginary part of the correction to the cyclotron resonance condition for $\omega = k - \Omega$. In this case one obtains

$$\Gamma_m = \left(\frac{\omega_p^2 \, \Omega \cos^2 \theta [\omega_m + q_m (\tan \theta + mc/\Omega a)^2]}{16 \, q_m^2 \, \omega_m} \right)^{1/2} \qquad \text{(L8)}$$

where ω_m k_m are given by Eqs. (L6) and (L7) and q_m is given by

$$q_m^2 = \frac{\Omega}{1 - \sin \theta} \left[\Omega (1 + \sin \theta) + 2m \cos \theta \right] \qquad \text{(L9)}$$

For the axisymmetric mode, Eq. (L8) reduces to

$$\Gamma_o = \left(\frac{\omega_p^2}{4} \sin \theta \, (1 - \sin \theta) \right)^{1/2} \qquad \text{(L10)}$$

Thus, the growth rate for the axisymmetric mode is independent of magnetic field strength; it increases as the square root of the beam density, and has a maximum for $\sin \theta = 0.5$,

i.e., $\theta = 30°$. It is also noted that this mode becomes stable for $\sin\theta < 0$. It can be shown that the cyclotron mode is unstable only when the helicity of the helix and of the electron trajectories has the opposite sense.

It is now desired to examine the $m = 1$ growth rate for comparison with that of $m = 0$. Equation (L3) may be rewritten to obtain

$$\omega_m^2 = q^2 \tan^2\theta + \frac{m}{2}\left(1 + \frac{k^2}{q^2} + 4k \tan\theta\right) \qquad \text{(L11)}$$

In order to effect a simple comparison with the $m = 0$ growth rate given by Eq. (L10), an underestimation of the $m = 1$ growth rate is made by replacing ω_m in the numerator of Eq. (L3) by $q \tan\theta$.

Then the $m = 1$ growth rate may be put in the form

$$\Gamma_1 \simeq \left(\frac{\omega_p^2}{4} \sin\theta\ (1 - \sin\theta)\ (1 + \eta)\right)^{1/2} \qquad \text{(L12)}$$

where

$$\eta = \frac{1}{[4(\Omega a/c)^2 \tan\theta\ (\tan\theta + c/\Omega a)]} \qquad \text{(L13)}$$

A comparison of Eqs. (L10) and (L12) shows that $m = 1$ grows faster than $m = 0$ for all values of Ω and $\tan\theta$. Indeed it is seen that

$$\frac{\Gamma_1}{\Gamma_0} = (1 + \eta)^{1/2} > 1 \qquad \text{(L14)}$$

since η is always greater than zero for positive pitch angles. It is evident from Eq. (L13), however, that the ratio of $m = 0$ to $m = 1$ growth rates is reduced by increasing either the gyrofrequency or the pitch angle. Although the desired mode never grows faster than the kink mode, the two growth rates can be brought fairly close at reasonable values of pitch angle and magnetic field strength. A wave initiator can be used to preferentially excite the $m = 0$ mode before the wave enters the growth sector, after which this liner could be used to safely grow the axisymmetric wave. Of course,

the $m = 1$ wave would be growing at a slightly greater rate but its initial amplitude would be that of the thermal noise in the beam while the initial amplitude of the $m = 0$ would be that generated by an external driver. Thus the $m = 0$ mode could probably be grown to sufficient amplitude for ion trapping before the kink mode could disrupt the beam.

B. Numerical Solutions of the Full Sheath Helix Dispersion Relation

The full dispersion relation given by Eq. (L1) is not tractable to an exact analytic solution because of the transcendental nature of the Bessel functions. As a result approximations to these functions have been employed in obtaining the analytical relations for phase velocities and growth rates of cyclotron waves in the system. In addition, the analytic work is generally restricted to a specific range of values of parameter space in order for these approximations to remain valid. Despite these limitations the analytic approach to a solution to the dispersion relation is most important because it gives results that allow a qualitative

understanding of the processes involved and directly yields the scaling of the frequencies and growth rates with the physical parameters of the problem. This approach also yields approximate quantitative results which are accurate to the degree that the approximations used are correct representations of the actual functions.

Once the analytic results are obtained it is desirable to check them using a computer program to solve the exact dispersion relation. This has been done for the sheath helix dispersion relation using the dispersion solver described in Ref. 1. This solver employs the full dispersion relation, Eq. (L1), and calculates the required Bessel functions of complex argument from their integral definitions. A modified Newton-Raphson iteration procedure is followed with the complex frequency as the iteration variable. Basically, the program computes the value of the dispersion function ϵ, the left hand side of Eq. (L1), for a fixed real k and an initial guess for ω. Then $\Delta\epsilon/\Delta\omega$ is computed and ω is stepped to bring the value of ϵ to zero. The result is considered to be converged when the incremental change in ω necessary to further

reduce the value of ϵ is below some predetermined limit.

An additional facility of the computer dispersion solver is that, besides allowing confirmation of wave growth due to the mode crossings studied analytically, it allows investigation of other areas of ω, k space for possible unstable waves. Two such unstable $m = 1$ modes have been found in past liner studies. Both have subsequently been examined theoretically in Ref. 1 and in Appendix M of this report, and were found to be stabilized for ω_p^2/Ω^2 less than about 1/4. This was then verified numerically.

The present computational study has involved an extensive examination of parameter space for the sheath helix-electron beam system. The $m = 0, 1$ wave growth has been examined for parameters in the following ranges:

$\tan\theta$	0.01	→	3.0
$\Omega a/c$	0.5	→	7.0
ω_p^2/Ω^2	0.01	→	0.4

All the qualitative features of the analytic solutions have been confirmed. There is also excellent quantitative agreement between the ω, k position of maximum wave growth given by Eqs. (L6) and (L7) and the computer results. In Figure L1 the phase velocity of the most unstable wave versus $\tan\theta$ is presented for constant $\Omega a/c = 1$. The solid lines are the theoretical predictions for $m = 0, 1$, and the data points represent the computational results. The growth rates of the waves found from the computer solutions to the dispersion relation are also in good agreement with the theory, Eq. (L8). The $m = 0$ and $m = 1$ growth rates are shown in Figure L2 for $\Omega a/c = 1$ and plotted versus $\tan\theta$. Again the solid lines are the theoretical predictions from Eq. (L8) and the data points are the computational results.

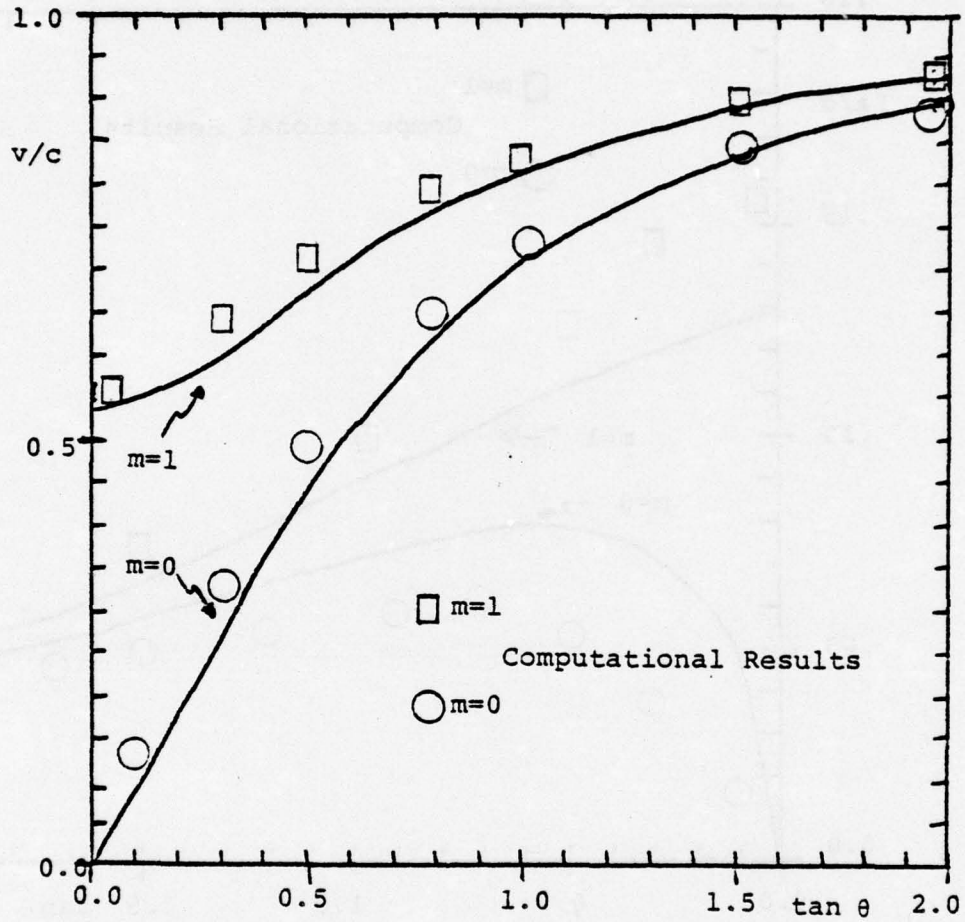

Figure L1. Phase Velocity of Modes 0, 1 vs. Tan θ for $\Omega a/c = 1$ and $\omega_p^2 a^2/c^2 = 0.1$.

Solid lines are analytical results.

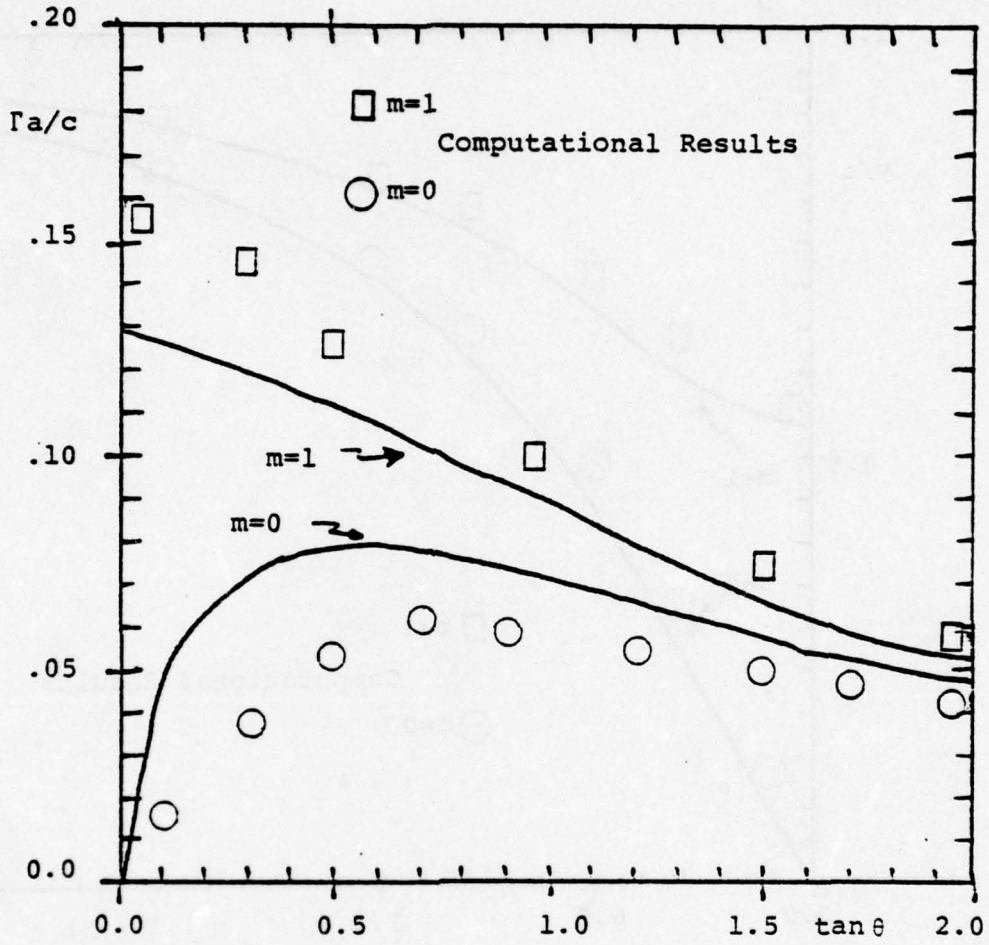

Figure L2. Growth Rates of Modes 0, 1 vs. Tan θ for $\Omega a/c = 1$ and $\omega_p^2 a^2/c^2 = 0.1$.

Solid lines are analytical results.

C. Summary and Conclusions

The sheath helix liner has been investigated for wave growth of the axisymmetric, $m = 0$, and the "kink," $m = 1$, modes through interaction of the negative energy beam cyclotron mode with positive energy modes associated with the helical structure. The axisymmetric mode has a phase velocity given by

$$v_p/c = \sin\theta \tag{L15}$$

and a growth rate given by

$$\frac{\Gamma_o a}{c} = \left(\frac{\omega_p^2 a^2}{4 c^2} \sin\theta \ (1 - \sin\theta) \right)^{1/2} \tag{L16}$$

The disruptive "kink" mode has been shown to grow faster than the $m = 0$ mode for all values of pitch angle and magnetic field strength, although it has been demonstrated that increasing the pitch angle and/or the field strength has a stabilizing influence on the $m = 1$ mode. In fact for $\Omega a/c \tan\theta \geq 2.4$ the $m = 0$ growth rate is at least 80 percent of the $m = 1$ rate.

This work shows that in this parameter regime such a configuration could be a useful wave growth structure provided a wave initiator can be used prior to the growth section to generate axisymmetric perturbations in the electron beam. Such a "tickler" would also serve to select a dominant single frequency component in the wave. This frequency component would then have a much larger initial amplitude upon entering the growth region and would thus be the major component in the large amplitude wave grown there.

A comparison of the sheath helix liner with the previously studied resistive liner shows that the maximum growth rates for the helix liner are at least 3.5 times greater than those for the resistive liner, for wave phase velocities corresponding to 250 keV ion injection energies. If higher injector energies are allowed, or if the wave may be slowed down after growth but prior to ion injection, then even faster growth rates and thus shorter liners are obtainable.

Future efforts need to be directed toward a study of the finite geometrical effects associated with a

physical helix, including finite spacing between the wires. Special consideration should be given to a search for a structure that could be prejudiced against the ubiquitous $m = 1$ disturbance without a significant reduction in the growth rate of the desired axisymmetric mode.

APPENDIX M

SUPPRESSION OF THE m = 1 HYDRODYNAMIC INSTABILITY FOR THE SHEATH HELIX GROWTH SECTION

Methods for suppression of the hydrodynamic instability for the edge ring resistive liner growth configuration have been reported previously (Ref. 1). In this appendix, the requirement on magnetic field strength sufficient to quench this instability for a sheath helix growth section is derived.

Computational analysis of a helical travelling wave reactive growth structure indicates the presence of a strong nonaxisymmetric (m = 1) instability occurring at very long parallel wavelength. The governing dispersion relation has been derived previously and is here re-stated for completeness:

$$\frac{\psi^+ - \psi^-}{(1+\beta\psi^+)(1+\beta\psi^-)} + \frac{2\,qa\,\omega^2\,K^+}{K^{+2}(k^2-q^2)-\alpha^2 k^2} = 0 \qquad \text{(M1a)}$$

where

$$\alpha \equiv \frac{m}{qa} + \frac{q}{k}\tan\theta \qquad \text{(M1b)}$$

$$\beta \equiv \frac{m}{\omega a(k-\omega)} + \frac{\tan\theta}{\omega} \tag{M1c}$$

$$K^{+} \equiv \frac{K_{m+1}(qa) + K_{m-1}(qa)}{2\,K_{m}(qa)} \tag{M1d}$$

and

$$q \equiv \sqrt{k^2 - \omega^2} \tag{M1e}$$

Here ω, k are the frequency and parallel wave number of the wave, respectively; m, the azimuthal mode number; θ, the pitch angle of the helix and a, the radius of the helical wave guide. Moreover

$$\psi^{\pm} \equiv \xi^{\pm}\, J_m(\xi^{\pm}a)/J_{m\pm1}(\xi^{\pm}a) \tag{M1f}$$

where

$$\xi^{\pm} \equiv \left(\omega^2 - k^2 - \frac{\omega_p^2(k-\omega)}{k-\omega\pm\Omega}\right)^{1/2} \tag{M1g}$$

Here ω_p is the relativistic beam plasma frequency and Ω, the relativistic cyclotron gyrofrequency.

We now consider the $m = 1$ kinking instability for the low k limit.

For $k \to 0$ and $\xi^{\pm} a$ small, the functions K^+, $\psi^{\pm}$ assume the following limits:

$$\psi^+ \to 4 \tag{M2}$$

$$\psi^- \to \frac{1}{2} (\xi^- a)^2 \tag{M3}$$

and with the further assumption that $\beta\psi^+ > 1$, the dispersion relation assumes the following simple form:

$$\frac{\omega_p^2}{\omega(\omega + \Omega)} + 1 + h^{-1}(qa) = 0 \tag{M4}$$

where $h(qa)$ is given by

$$h(qa) = \frac{2 K^+(qa)}{qa(K^{+2}(qa) + \tan^2 \theta)} \tag{M5}$$

The function $h(qa)$ is monotonic decreasing in qa, from a maximum value of 2. Utilizing this upper bound on $h(qa)$ in Eq.(M4), we obtain as a sufficient condition for stability

$$\omega_p^2 < \frac{3}{8}\,\Omega^2 \qquad \text{(M6)}$$

Note that this stability condition is independent of the pitch of the helical structure and only depends on beam-magnetic field parameters.

APPENDIX N

TAPE HELIX DISPERSION RELATION

This work begins a consideration of the effects of the finite geometry associated with a helical liner structure made with wires of finite size and with finite spacing between the wires. Previous analysis, Appendix L of this report, has dealt with the sheath helix model, a physically smooth conducting sheet at the outer boundary of the electron beam with perfect conductivity in a direction oblique to the beam. Such a liner could be made by winding many fine wires to form a helical solenoid. For wavelengths much larger than either the wire thickness or the spacing between the wire, this should compare favorably to the mathematical model of the sheath helix. The present model is the tape helix wound with a single tape of width δ and turn to turn spacing d.

The dispersion relation for waves in the tape helix-electron beam system is derived and the normal modes of this system analyzed and compared with those of the sheath helix. The dispersion relation for these normal modes in

the absence of the beam is examined. Coupling of these helix modes with the beam cyclotron mode is considered under certain restrictions, and growth rates are obtained. It is shown that for mode coupling in certain regions of ω,k space the physics of the interaction is only slightly modified from the sheath helix results by the finite geometry of the tape.

Derivation of the Dispersion Relation

In Figure N1 a schematic drawing of the tape helix model is shown. The tape width δ, the turn to turn spacing d, and the radius of the winding a, specify the physical system. The pitch angle θ is related to these parameters by $\cot\theta \equiv \frac{2\pi d}{a}$. The mathematical model for the tape conductivity is

$$\sigma(r,\theta,z) = \sum_n \frac{d}{4a\delta R} H\left(\frac{2\pi}{d}(z+\delta/2) - (\theta+2\pi n)\right)$$

$$\times \left\{1 - H\left(\frac{2\pi}{d}(z-\delta/2) - (\theta+2\pi n)\right)\right\} \cdot \delta(r-a) \qquad (N1)$$

where R is the resistivity per unit length and the H functions are the Heaviside or step functions with the

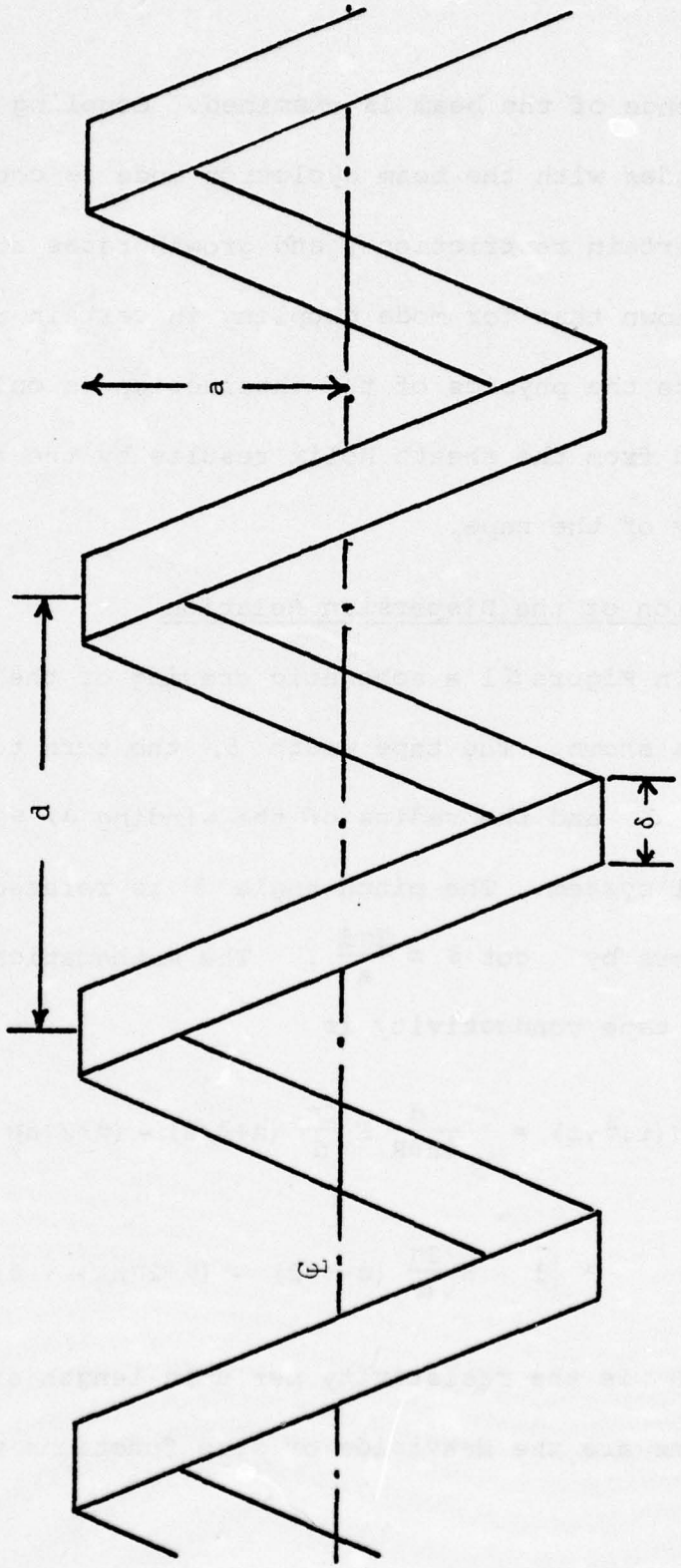

Figure N1. Geometry of Tape Helix

properties:

$$H(x) = 0 \quad \text{for} \quad x < 0$$

and $$H(x) = 1 \quad \text{for} \quad x \geq 0$$

Since this is a periodic structure in z and θ, the conductivity may be expanded in a Fourier series of the form:

$$\sigma = \sum_{n=-\infty}^{\infty} \frac{1}{8aR} \frac{\sin(n\pi\delta/d)}{(n\pi\delta/d)} e^{in\left(\frac{2\pi z}{d} - \theta\right)} \tag{N2}$$

The field quantities in the system are expressed in an appropriate basis function expansion, as follows:

$$F(r,\theta,z) = \int_{-\pi/d}^{\pi/d} d\beta \; e^{i\beta z} \sum_{\ell} e^{i\ell\frac{2\pi}{d}} \sum_{m} e^{im\theta} F_{K,m}(r) \tag{N3}$$

where the effective longitudinal wave vector k is expressed $k = \beta + 2\pi\ell/d$.

The Fourier components $F_{K,m}(r)$ are now found from Maxwell's equations solved in the beam region and outside the beam. These are as follows.

Beam region

$$E_z = \alpha_{k,m}\,\psi^+ + \beta_{k,m}\,\psi^- \tag{N4}$$

$$E_\theta = \alpha_{k,m}\left(\omega + \frac{m}{(k-\omega)}\,\psi^+\right) - \beta\left(\omega - \frac{m}{(k-\omega)}\,\psi^-\right) \tag{N5}$$

$$E_r = -i\alpha_{k,m}\left(k - \frac{\omega_p^2}{\omega - k - \Omega} + \frac{m}{(k-\omega)}\,\psi^+\right)$$

$$- i\beta_{k,m}\left(k - \frac{\omega_p^2}{\omega - k + \Omega} - \frac{m}{(k-\omega)}\,\psi^-\right) \tag{N6}$$

$$B_z = - i\alpha_{k,m}\,\psi^+ + i\beta_{k,m}\,\psi^- \tag{N7}$$

$$B_\theta = - i\alpha_{k,m}\left(\omega - \frac{\omega_p^2}{\omega - k - \Omega} + \frac{m}{(k-\omega)}\,\psi^+\right)$$

$$- i\beta_{k,m}\left(\omega - \frac{\omega_p^2}{\omega-k+\Omega} - \frac{m}{(k-\omega)}\,\psi^-\right) \tag{N8}$$

$$B_r = \alpha_{k,m}\left(k - \frac{m}{k-\omega}\,\psi^+\right) - \beta_{k,m}\left(k + \frac{m}{(k-\omega)}\,\psi^-\right) \qquad (N9)$$

where

$$\psi^{\pm} = \frac{q^{\pm}\, I_m(q^{\pm})}{I_{m\pm1}(q^{\pm})} \qquad (N10)$$

$$q_{\pm}^2 = k^2 - \omega^2 - \frac{\omega_p^2\,(k-\omega)}{\omega - k + \Omega} \qquad (N11)$$

Liner Region

$$E_z = \alpha'_{k,m}\, qK \qquad (N12)$$

$$E_\theta = \alpha'_{k,m}\,\frac{mk}{q}\,K - \beta'_{k,m}\,\omega \qquad (N13)$$

$$E_r = -\,i\alpha'_{k,m}\,k + i\beta'_{k,m}\,\frac{m\omega}{q}\,K \qquad (N14)$$

$$B_z = i\beta'_{k,m}\, qK \qquad (N15)$$

$$B_\theta = -\,i\alpha'_{k,m}\,\omega + i\beta'_{k,m}\,\frac{mk}{q}\,K \qquad (N16)$$

$$B_r = -\alpha'_{k,m} \frac{m\omega}{q} K + \beta' k \tag{N17}$$

where $$K = \frac{\kappa_m(q)}{\kappa'_m(q)} \tag{N18}$$

and $$q^2 = k^2 - \omega^2 \tag{N19}$$

where $\kappa_m(z)$ and $I_m(z)$ are modified Bessel functions of order m and argument z.

Applying Maxwell's equations to the boundary region provides a set of matching conditions sufficient to specify the four sets of undetermined coefficients, $\alpha_{k,m}$, $\beta_{k,m}$, $\alpha'_{k,m}$, and $\beta'_{k,m}$.

Three of the "jump" conditions, governing the tangential electric field components and the components of magnetic field parallel to the tape direction, are satisfied for each Fourier component separately:

$$\begin{aligned}
&(1)\quad E_\theta^{k,m}\ (\text{beam}) - E_\theta^{k,m}\ (\text{liner}) = 0 \\
&(2)\quad B_z^{k,m}\ (\text{beam}) - B_z^{k,m}\ (\text{liner}) = 0 \\
&(3)\quad B_\parallel^{k,m}\ (\text{beam}) - B_\parallel^{k,m}\ (\text{liner}) = 4\pi J_\parallel^{k,m}(\text{beam})
\end{aligned} \tag{N20}$$

The fourth matching condition relates the magnetic field components perpendicular to the tape to the tape current

and the parallel beam current. This condition couples all the Fourier modes. It is

$$(4)\quad B_{\perp}^{k,m}\,(\text{beam}) - B_{\perp}^{k,m}(\text{liner}) = 4\pi J_{\perp}^{k,m}(\text{beam}) + 4\pi \sum_{k'} \sigma_{k-k',m-m'}\, E_{\parallel}^{k',m'}(\text{liner}) \qquad (N21)$$

Using these conditions it is possible to solve for the coefficients $\alpha'_{k,m}$, $\beta'_{k,m}$, and $\beta_{k,m}$ in terms of the coefficient $\alpha_{k,m}$ and, after considerable algebra, obtain the following governing equation for the system:

$$\alpha_{k,m}\,\mathcal{E}_m(k_n) = \sum_r \frac{\pi}{2aR}\,\frac{\sin(r\pi/d)}{(r\pi/d)}\,\alpha_{k',m+r}\,\epsilon_{m+r}(k'_{n-r}) \qquad (N22)$$

where

$$k_n = \beta + 2\pi n/d\ . \qquad (N23)$$

Here $\mathcal{E}_m(k_n)$ is the dispersion function for Fourier modes of order m and wavenumber k_n in a beam vacuum system, given by

$$\mathcal{E}_m(k_n) = \left(\psi^{+}\left(\frac{mk}{q}K + \omega\right) - \beta^{+}qK\right) \times \left(\psi^{-}\left(\frac{mk}{q}K - \omega\right) + \beta^{-}qK\right) \qquad (N24)$$

where $\psi^{\pm}$ and K are as previously defined and

$$\beta^{\pm} = \left(\omega^{\pm} \frac{m}{(k-\omega)} \psi^{\pm}\right) \quad .$$

The function $\epsilon_m(k_n)$ is the sheath helix dispersion function for Fourier modes of order m and wavenumber k_n (see Appendix L) and is given by

$$\epsilon_m(k_n) = \omega \ (\psi^+ + \psi^-)\left(\omega^2 \cos^2\theta - \left(\frac{mk}{q}\cos\theta + q\sin\theta\right)^2 K^2\right)$$

$$+ 2qK\left(\omega\cos\theta + \left[\frac{m\cos\theta}{(k-\omega)} + \sin\theta\right]\psi^+\right)\left(\omega\cos\theta - \left[\frac{m\cos\theta}{(k-\omega)} + \sin\theta\right]\psi^-\right) \tag{N25}$$

If the helical conductor fills the entire boundary region at $r = a$, i.e., $\delta/d = 1$, then the weight function $\frac{\sin(r\pi\delta/d)}{(r\pi\delta/d)}$ is nonzero only for $r = 0$, and Eq. (N22) reduces to the form

$$\alpha_{\beta,\ell,m}\left\{\epsilon_m\left(\beta + \frac{2\pi\ell}{d}\right) - \frac{\pi}{2aR}\epsilon_m\left(\beta + \frac{2\pi\ell}{d}\right)\right\} = 0 \tag{N26}$$

for each α coefficient.

In this case each angular mode number satisfies a separate dispersion relation independently of the other angular modes. Eq. (N26) is the sheath helix dispersion

relation for finite resistance in the helical conductor. For $R = 0$ this becomes the perfectly conducting sheath helix liner described in Appendix L of this report.

On the other hand, when the tape width is reduced so that there is space between turns of the tape then combinations of angular modes are necessary to satisfy the boundary conditions. If the tape width δ is reduced such that $\delta/d \ll 1$ then each angular mode is weighted approximately equal in the solution to Eq. (N22) and this equation becomes

$$\alpha_{\beta,\ell,m}\,\mathcal{E}_m\left(\beta+\frac{2\pi\ell}{d}\right)=\frac{\pi}{2aR}\sum_r\alpha_{\beta,\ell-r,m+r}\,\epsilon_{m+r}\left(\beta+\frac{2\pi(\ell-r)}{d}\right) \tag{N27}$$

It can be shown that the right-hand side of Eq. (N27) is independent of ℓ or m for all ℓ and m such that $\ell+m$ = constant. A recursion relation for the α's thus obtains

$$\alpha_{\beta,\ell,m}\,\mathcal{E}_m\left(\beta+\frac{2\pi\ell}{d}\right)=\alpha_{\beta,N,0}\,\mathcal{E}_0\left(\beta+\frac{2\pi N}{d}\right) \tag{N28}$$

For the case where the wire resistance $R \to 0$, the following dispersion relation for modes of index N is obtained, using the recursion relation Eq. (N28):

$$\sum_n \frac{\epsilon_n\,(\beta + 2\pi(N-m)/d)}{\epsilon_n\,(\beta + 2\pi\,(N-m)/d)} = 0 \qquad \text{(N29)}$$

Normal Modes in the System

Before examining the narrow tape helix dispersion relation, Eq. (N29), it will be of some benefit to consider the normal mode structure in this system. A normal mode is characterized by a parameter N and contains contributions from all angular modes such that $m + \ell = N$. Thus a normal mode may be written in the form

$$E_N = \sum_m \alpha_{N-m,m}\, e^{iz(\beta+2\pi(N-m)/d)}\, e^{im\theta} \qquad \text{(N30)}$$

The recursion relation, Eq. (N28), allows a calculation of the relative amplitudes of these components to obtain

$$E_N = \alpha_{N,o} \sum_m \frac{\epsilon_o\left(\beta + \frac{2\pi N}{d}\right)}{\epsilon_m(\beta+2\pi(N-m)/d)} \exp i\left[m\theta + z\left(\beta + \frac{2\pi}{d}(N-m)\right)\right] \qquad \text{(N31)}$$

Normal Mode Dispersion Relation ($\omega_p^2 = 0$)

The general dispersion relation for the narrow tape helix, Eq. (N29), may be simplified in the limit of zero beam density, where the expression reduces to

$$0 = \sum_m K_m'(q_m) I_m'(q_m) \left(\omega^2 I_m'(q_m) K_m'(q_m) + \left(\frac{mk}{q} + q\tan\theta \right)^2 I_m(q) \; K_m \right) \tag{N32}$$

Now if none of the q_m's approach zero the large argument expansion of the Bessel functions may be used to obtain an approximate dispersion relation

$$0 \approx \left(\omega^2 - q_N^2 \tan^2\theta \right) \sum_m \frac{1}{q_m^2} \tag{N33}$$

The factor $\omega^2 - q_N^2 \tan^2\theta$ is common to each term in the sum, and thus setting this factor to zero provides a solution to Eq. (N33). From the definition of q_N this may be written in a simplified form

$$\frac{\omega a}{c} = \beta a \sin\theta + N \cos\theta \tag{N34}$$

This is formally the same dispersion relation found for the sheath helix liner for a mode of order N and wavenumber β. However, the present relation characterizes the ω,β dependence of a normal mode of parameter N which is comprised of a combination of angular modes with different wavenumbers $k = \beta + 2\pi(N-m)/d$.

To examine this normal mode structure, we note that

$$\mathcal{E}_m(\beta+2\pi(N-m)/d) = \omega^2/(K_m'^2(q) I_{m+1}(q)\ I_{m-1}(q)) \qquad (N35)$$

for $\omega_p^2 \to 0$; and for $q^2a^2 > 1$,

$$\mathcal{E}_m(k_m) \cong q_m^2\ \omega^2/4 \qquad (N36)$$

Thus the contribution of the angular components to the normal mode is weighted by the relative value of the parameter $q_m = (k_m^2 - \omega^2)^{1/2}$, so that the normal mode can be written

$$E_N = \sum_m \alpha_{N,o}\ (q_o^2/q_m^2)\ \exp i\,(m\theta + k_m z) \qquad (N37)$$

where again $k_m = (\beta + 2\pi(N-m)/d)$.

Since the parameter β is variable only over the range $-\pi/d < \beta < \pi/d$, it is seen that the $m = N$

component has the largest amplitude of any component and thus dominates the normal mode.

Coupling of Tape Helix Free Modes with Beam Cyclotron Mode

In the region of ω,k space where the frequency and wavenumber of the negative energy beam cyclotron mode coincide with those of a positive energy helix mode, the resonant transfer of energy may occur causing growth of both waves. The tape helix normal modes consist of a collection of angular modes that have a common frequency but different wavelengths. These modes obey the dispersion relation given by Eq. (N34) provided none of the q's of any of the angular components are small. At a fixed frequency it is only possible for the cyclotron mode to couple with a single angular component of a helix normal mode. Since all the angular components of a normal mode maintain fixed relative amplitudes to satisfy the boundary conditions, the energy transferred from the cyclotron mode to a single component of the helical mode must be shared by all the components. The transfer of energy between

components of the helix modes occurs by means of currents generated in the tape.

The growth rate of a normal mode may be found by Taylor expanding the general dispersion relation, Eq. (N29), about $\omega_p^2 = 0$ and keeping the ω_p^2 correction only for the term whose ω, k approximately satisfy the beam cyclotron dispersion relation

$$\omega \approx k - \Omega \approx \beta + 2\pi(N-m)/d - \Omega \tag{N38}$$

The peak growth occurs at the $\beta_o a$ such that

$$\beta_o a = (\Omega + N \cos\theta)/(1-\cos\theta) - (N-m)\cot\theta \tag{N39}$$

Since the parameter βa is defined only in the range $-\frac{\cot\theta}{2} < \beta a < \frac{\cot\theta}{2}$ the above condition implies a restriction on the angular components of a given normal mode that can couple to the cyclotron mode.

The peak growth rate under these assumptions is

$$\Gamma_{N,n} = \left(\frac{\omega_p^2 \Omega \cos^2\theta \,(\omega_n + q_n(\tan\theta + \frac{n}{\Omega}))^2}{16\, q_n^2\, \omega_n} \;\; \frac{1/q_n^2}{\sum_m 1/q_m^2} \right)^{1/2} \tag{N40}$$

where ω_n is found from Eq. (N38) for $\beta = \beta_o$. This growth rate has been written in form that allows simple comparison with the sheath helix results in Appendix L of this report. In fact, the ratio of the growth rates may be written

$$\frac{\Gamma_{N,n}\ \text{tape}}{\Gamma_n\ \text{sheath}} = \left(\frac{1/q_n^2}{\sum_m 1/q_m^2} \right)^{1/2} \tag{N41}$$

Thus the tape helix growth rate is always less than that of a sheath helix with equal pitch angle. Since

$$q_\ell^2 \equiv (\beta + 2\pi(N-\ell)/d)\,\ell - \omega^2$$

it is seen that the growth rate will be a maximum for a normal mode if the cyclotron mode couples with the dominant, angular component of the mode, $N = m$. In the limit $\beta \ll \pi/d$ the fundamental component is much larger than any other component and the infinite sum $\sum_m 1/q_m^2$ is approximately equal to $1/q_N^2$. Only in

this limit does the tape helix growth approach that of the sheath. The lower growth rates for the tape helix may be thought of in terms of an increased "inertia" provided by the other angular components of the normal mode which do not couple to the cyclotron mode.

Thus it is possible to arrange the crossing of the cyclotron mode with the $N = 0$ normal mode in a region of ω, k space where the normal mode is predominantly axisymmetric. At the same time, the $N = 1$, $m = 1$ crossing can be avoided entirely and the $N = 2$, $m = 1$ normal mode crossing occurs in a region where the $m = 2$ component is dominant, Eq. (N41), thus indicating a reduced growth rate for $m = 1$. This can occur if $\Omega a/c$ is in the range

$$\frac{\cot\theta}{2}(1-\sin\theta) > \frac{\Omega a}{c} > \left[\frac{\cot\theta}{2}(1-3\sin\theta), 0\right] \text{ largest} \qquad \text{(N42)}$$

For such a case the axisymmetric growth rate will be approximately that obtained for the sheath helix while the nonaxisymmetric growth will be reduced from the sheath helix growth by a factor $((1/q_1^2)/\sum_m (1/q_m^2))$.

Summary

The preceding analysis has shown that the tape helix couples less effectively to the beam cyclotron mode than does the sheath helix. In addition, the wave grown in the beam, since it is a normal mode of the system, contains all angular modes. However, it appears possible to grow an almost pure axisymmetric mode in the beam by arranging the crossing with the cyclotron mode to occur at small values of the parameter β. This also allows the tape helix growth rate to approach that of the sheath helix. Thus it does appear possible to grow the desired mode with such a liner structure.

Analysis also indicates that the $m = 1$ "kink" instability in the beam will have a growth rate reduced from that for a sheath helix liner under certain conditions. In this case the relative growth rates of the $m = 0$ and $m = 1$ waves in the beam have a more favorable value than for the sheath helix.

APPENDIX O

A MODIFIED RESISTIVE GROWTH MECHANISM USING DISCRETE LOOP DRIVES

In this appendix, the use of discrete, uncoupled loop drives connected to external RC lumped circuits is examined for growth of the axisymmetric, low frequency cyclotron mode. It is shown that a considerable improvement in growth rate over the usual resistive type growth mechanisms can be achieved if the value of capacitance is chosen to be resonance with the inductance of the loops at the driving frequency. Operation at frequencies well removed from resonance reduces the growth rate (or, more precisely, increases the growth length) to a value comparable to the resistive liner configurations discussed in Ref. 1.

Arguments are presented for achievement of a system which is relatively stable to the $m = 1$ kinking type mode.

Voltage handling capability is also investigated. It may be required to either detune the rings for the final tens of centimeters of growth to avoid power handling problems (thereby resulting in an increased growth length), or to include more rings. This second possibility, if carried to the limit, would result in a simple modification of the usual edge ring liner configuration in that, rather than utilizing shorted rings, the rings would be connected to a distributed capacitive-resistive network. The consequences of such a configuration have not yet been investigated. Here we restrict our attention to discrete loop drives.

Governing Equations for Discrete, Uncoupled Loop Drives

In Appendix K, the amplitude of the cyclotron eigenmode established by a series of loop drives is derived. For loops located at monotonically ordered positions z_n, of current I_n and voltage V_n, the relevant equations may be put in the following tractable form:

For each loop, the loop voltage is given by

$$V_N = L\,\dot{I}_N + \alpha \sum_{n=0}^{N} \dot{I}_n \sin \Omega\,(z_N - z_n)/c + \frac{2\pi a}{c}\,\dot{A}_{\theta o} \qquad (01)$$

with the θ component of vector potential between the N^{TH} and $N + 1^{ST}$ loops given by

$$A_\theta = \frac{\alpha}{2\pi a} \sum_{n=0}^{N} I_n \sin \Omega(z - z_n)/c + A_{\theta o} \qquad (02)$$

The principle of superposition has been used to include the effects of an incident wave of amplitude $A_{\theta o}$. Here L is the inductance of the loop; Ω the relativistic cyclotron frequency; a, the beam radius; and α, a coupling coefficient of the loop drive to the wave given by

$$\alpha = 8\pi^2 a\,\frac{\omega_p^2}{(k^2c^2 + \omega_p^2)^2}\,\frac{\Omega a}{c} \times \left\{ \begin{array}{c} \text{geometrical} \\ \text{factors} \end{array} \right\} \qquad (03)$$

Here ω_p is the relativistic electron plasma frequency and k, the total wave vector of the wave.

The current I_n is strictly evaluated at the retarded time: $t - (z - z_n)/c$. However, for low frequency drives, the retardation factor can be neglected. This requires that the region $z - z_n$ be limited to

$$(z - z_n) < 2\pi c/\omega_o \tag{04}$$

where ω_o is the driving frequency.

We note two interesting features of these equations:

(1) All circuits upstream of the N^{TH} loop contribute to V_N through the cyclotron wave coupling coefficient α, while the current in the N^{TH} loop only contributes through the loop inductance L.

(2) Each loop propagates downstream a standing cyclotron wave contribution.

It is thus obvious that at least two loops are required, properly phased, in order to generate a travelling cyclotron wave by an appropriate phasing of these two standing waves.

We thus turn our attention to a specific configuration of two loops which are connected to external RC circuits. Let these loops be located at

$$z_o = 0$$

$$z_1 = d \tag{05}$$

with an incident wave given by

$$A_{\theta o} = \exp\ (i\omega t - i\Omega z) \tag{06}$$

The steady state equations governing V_o, V_1 and $A_\theta (z > d)$ are found from Eqs. (01) and (02):

$$V_o = i\omega L\ I_o + i2\pi a\ \omega/c \tag{07}$$

$$V_1 = i\omega L\ I_1 + i\omega\alpha\ \sin\ \Omega\ d/c + \frac{i2\pi a\omega}{c}\ e^{-i\Omega\ d/c} \tag{08}$$

$$2\pi a\ A_\theta (z > d) = \alpha\ I_o\ \sin\ \Omega z/c + \alpha\ I_1\ \sin\ \frac{\Omega}{c}\ (z - d)$$

$$+ 2\pi a\ \exp\ - i\Omega z/c \tag{09}$$

Let Z_o and Z_1 be the impedance of the external RC circuit elements attached across loop $N = 0$ and $N = 1$, respectively, so that:

$$V_o + Z_o\ I_o = 0 \tag{010a}$$

$$V_1 + Z_1\ I_1 = 0 \tag{010b}$$

Using Eqs. (07) through (010b), we inquire of the choice of parameters Z_o, Z_1, and d to achieve both amplification of the incident wave and suppression of any standing wave components downstream of the two loops. To achieve the second objective we demand that

$$A_\theta(z > d) \propto \exp - i\Omega z/c \tag{011}$$

which requires

$$I_o + I_1 \exp(- i\Omega d/c) = 0 \tag{012}$$

with the resultant expression for A_θ:

$$A_\theta(z > d) = \exp\ (- i\Omega z/c) \left[1 - \frac{\alpha\ I_o}{4\pi i a} \left(1 - \exp(2i\Omega d/c)\right)\right] \tag{013}$$

The first term in Eq. (013) represents the amplitude of the incident cyclotron wave; the second, the contributions from the two loop drives. To maximize their effect, we take

$$\exp\ (2i\ \Omega d/c) = - 1 \tag{014}$$

so that the appropriate spacing of the loops is at odd quater wavelengths:

$$d = \frac{N\pi}{2}\, c/\Omega, \quad N = 1, 3, 5, 7, \ldots \tag{015}$$

Using Eqs. (07) through (010b) in Eq. (012) we find that

$$Z_1 = Z_o + \omega\alpha \tag{016}$$

with an amplification factor A calculated from Eq. (013):

$$A = 1 + \frac{\omega\alpha}{Z_o + i\omega L} \tag{017}$$

Growth Lengths for Discrete Loop Drives

We have seen that a pair of passive loops located an odd quarter cyclotron wavelength apart operates as an amplifier for the negative energy travelling cyclotron wave with an amplification factor given by Eq. (017), provided the loop impedances are chosen consonant with Eq. (016).

If, for the first pair of loop drives we choose

$$Z_o = \frac{1}{i\omega C} \tag{018}$$

where the capacitance C is chosen so that

$$\omega_o^2 \, LC = 1 \tag{019}$$

then the amplification factor is infinite (i.e. we obtain an oscillator or wave initiator). Such an LC circuit could easily be pumped up to high power levels using conventional RF drives. Furthermore, the total power dissipated in the first loop is zero (to the extent that the loop resistance is zero); i.e., only reactive power is required.

The second loop located appropriately downstream must have an external impedance

$$Z_1 = \frac{1}{i\omega C} + \omega\alpha \tag{020}$$

(i.e. an RC series network) and converts the initial standing wave set up by the first loop to the appropriate travelling wave.

Subsequent pairs of loops may then be located downstream of the first pair to act as amplifiers. There is no requirement on the spacing of the pairs of loops relative to each other, other than the fact that the

spacing must be sufficient so that the loops are not coupled by their mutual free space inductance.

If the impedances of the N^{TH} loop pair are, for example, chosen as

$$Z_{oN} = \frac{1}{i\omega C} + \frac{1}{2}\omega\alpha$$

$$Z_{1N} = \frac{1}{i\omega C} + \frac{3}{2}\omega\alpha \qquad (021)$$

and the pairs of loops are spaced roughly every cyclotron wavelength, then growth lengths $\mathcal{L}$ of the order of

$$\mathcal{L} \sim 2\pi c/\Omega \qquad (022)$$

are obtained.

On the other hand, if instead of operating at resonance, we set $C = 0$, then the growth length increases to

$$\mathcal{L} \sim \frac{2\pi c}{\Omega}\ \frac{L}{\alpha} \qquad (023)$$

Utilizing the value of α given in Eq. (03), we obtain

$$L \sim 2\pi a \left(\frac{c}{\Omega a} \right)^2 \frac{k_\perp^2 c^2}{\omega_p^2} \qquad (024)$$

and note that this growth length is of the same order of magnitude as the usual type resistive liner growth length (Ref. 1).

Suppression of m = 1 Kink Modes

It has been pointed out* that the high efficiency and strong coupling for the discrete, resonant loop drive system arise from the fact that magnetic coupling of the loops to the electron beam is being utilized, as opposed to electric field coupling for the usual resistive liner configurations.

Since the magnetic field of a loop drive is quite uniform for low frequencies (i.e. the field configuration is dominated by $m = 0$ contributions for $\omega a/c < 1$), coupling to the nonaxisymmetric resistive kink mode should not occur via magnetic coupling. Coupling can

*D. Brower, private communication.

occur through the electric fields as in the usual resistive liner configurations; however, these growth lengths would correspond to the usual resistive liner configurations and would be correspondingly much longer than the $m = 0$, magnetic coupling length.

A second attractive feature of using discrete loop drives is the stabilization of the hydrodynamic kink mode. An external conductor slotted in the streaming direction can be brought arbitrarily close to the loop drives without affecting their operation. This configuration should then stabilize the hydrodynamic kink instability by providing a good return current path in the beam direction (see Appendix I, Ref. 1).

Some Practical Considerations for Resonant Discrete Loop Drives

A possibly severe limiting feature of such loop drives is the presence of very high voltage levels across the loop input gap when very large amplitude cyclotron waves are grown, particularly if the loops are operated near resonance. The calculation of these voltage levels

is straightforward. From Eqs. (07) and (010a), the total current in loop $N = 0$ is calculated to be given by

$$I_o = \frac{i\,2\pi a\,\omega}{(Z_o + i\omega L)c} \tag{025}$$

with total gap voltage V_G given by $V_G = Z_o I_o$:

$$V_G = \frac{Z_o}{Z_o + i\omega L}\; i\,2\pi a\,\omega/c \tag{026}$$

Relating V_G to the total potential φ of the wave through the relations governing the cyclotron wave ($\Omega\varphi \sim k_\perp c A_r \sim k_\perp c A_\theta \sim k_\perp c$ for $|A_{\theta o}| = 1$), we obtain

$$|V_G/\varphi| = \frac{Z_o}{|Z_o + i\omega L|}\;\frac{2\pi\,\omega a}{c}\;\frac{\Omega}{k_\perp c} \tag{027}$$

where

$$k_\perp = 2.9/a.$$

Thus, operation at resonance and low value of resistance (e.g. $1/2\ \omega a$) in order to obtain high amplification factors per pair of loops may result in a voltage V_G exceeding

the potential of the cyclotron wave. For large amplitude cyclotron wave potentials, it may then become necessary to operate considerably off resonance to avoid high voltage arc-over problems. Such operation will of course increase the total growth length of the growth section.

A second consideration of the use of resonant discrete loop drives is the required ring-up time of the loops. Analysis presented in this appendix is for the steady state behavior. Care must be taken so that the Q of the resonant circuits is sufficiently low that they can reach steady state early in the electron beam pulse. The ring up time τ is given by

$$\tau = L/R \tag{028}$$

of the circuits. Typically L is of the order of a few tens of nH; and for amplication factors near 2, we would choose $R = 1/2\ \omega\alpha$, a value which is typically a few ohms. Thus,

$$\tau \sim 10 - 30 \text{ ns} \tag{029}$$

This is not a severe limitation for an Auto-Resonant Accelerator configuration, since e-beam pulse times of 100 to 200 ns are required by other constraints (i.e. total ion acceleration time requirements).

AD-A033 946 AUSTIN RESEARCH ASSOCIATES INC TEX F/G 20/7
CONCEPTUAL DESIGN OF AN AUTO-RESONANT ACCELERATOR EXPERIMENT.(U)
NOV 76 W E DRUMMOND, G I BOURIANOFF F29601-76-C-0046
UNCLASSIFIED ARA-224 AFWL-TR-76-152 NL

3 OF 4
AD A033946

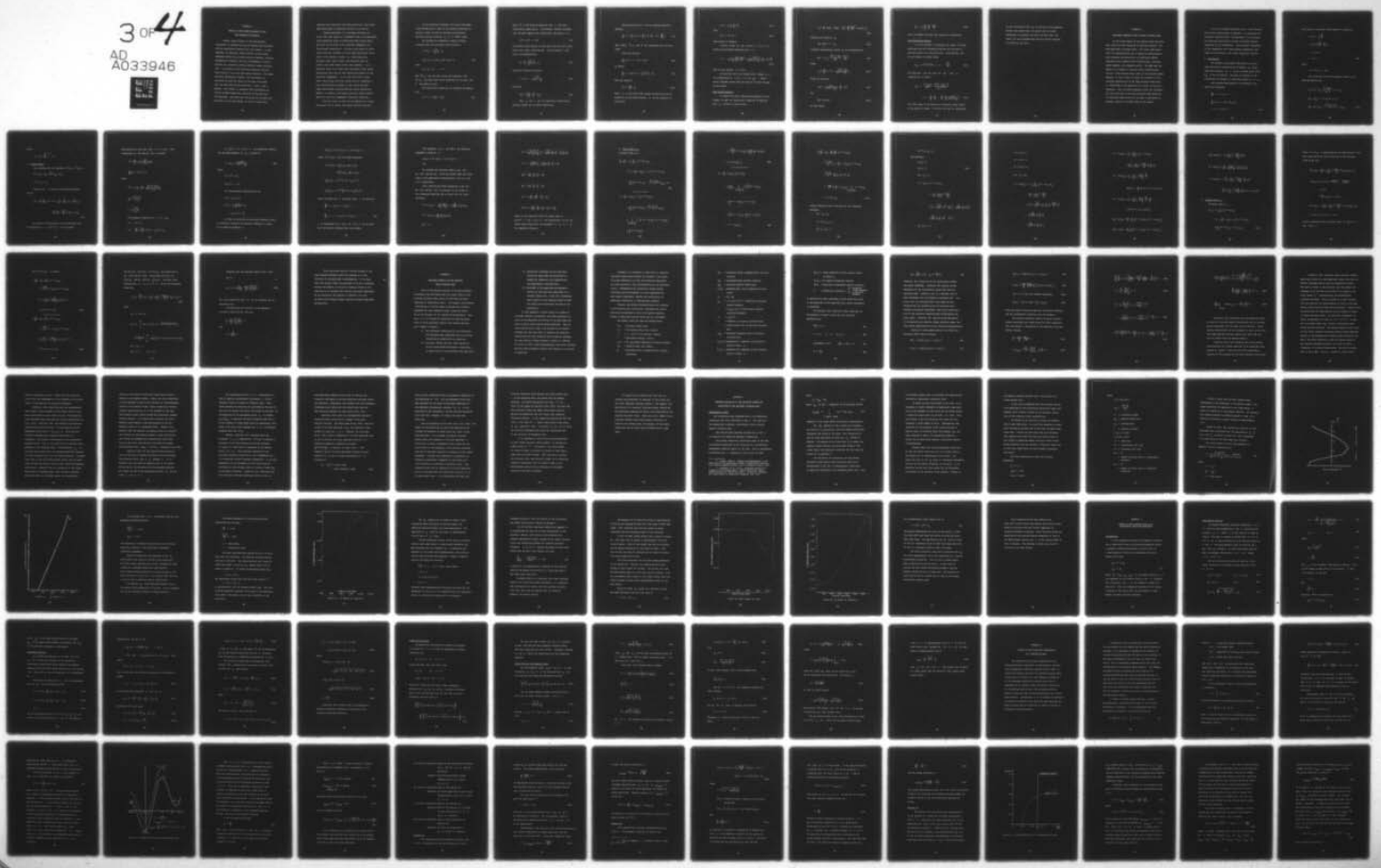

APPENDIX P

DETAILS OF WAVE ENERGY BALANCE IN THE AUTO-RESONANT ACCELERATOR

Overall energy balance in the Auto-Resonant Accelerator is governed by the wave energy flux relations and the conservation equation for total energy. In this appendix, the detailed, radial balance of wave energy exchanges between the electron parallel momentum, electron perpendicular momentum, and the electromagnetic field is derived for a spatially growing negative energy cyclotron wave. Integration of the resulting equations over the beam results in the usual wave energy equation. The radial equations demonstrate, however, that the energy is extracted not from the center of the beam, but rather near the outer edge of the beam where $J_1(k_\perp r)$ has a maximum. This effect is important when considering the virtual cathode formed upon injection of the beam into the waveguide; particles near the center of the beam have relatively little free energy, so that if energy were

required to be extracted from these particles, total field amplitudes might of necessity be held to low values.

Before proceeding, it is perhaps worthwhile to recall that wave energy is a quadratic form in the perturbed field quantities which is constructed from linear theory and which can be shown to be conserved independent of total energy conservation. As such, wave energy is calculated using only products of first order quantities (first order in the electric fields; i.e. those quantities available from linear theory) and therefore does not contain zero order times second order products. It is precisely these extra terms that distinguish total energy conservation from that of wave energy and renders the two equations independent. (It is also true that in some cases wave energy and total energy are not independent--e.g., nonrelativistic plasmas at rest, where the zero times second order contributions may vanish identically. However, in general, wave energy and total energy conservation do yield two independent constraint equations.)

With this point in mind, we now proceed to a direct calculation of the radial wave energy balance relations.

In the following treatment, the usual high gamma (ultra-relativistic) limit of the electron equations of motion is used, so that we consider the perturbed electron parallel velocity $\tilde{v}_z = 0$ to lowest order.

We consider an axisymmetric negative energy cyclotron wave with the basic wave structure:

$$\varphi = A_z = - \frac{k_\perp}{k_z c - \omega} A_r$$

$$iA_\theta = A_r \propto J_1(k_\perp r) \exp i(k_z z - \omega) \qquad \text{(P1)}$$

with

$$k_z = k_o - i\lambda \ , \quad \lambda > 0$$

Here $(\vec{k}, \omega)$ are the wave vector and frequency; with $(\vec{A}, \varphi)$, the usual four vector potential of the wave, and c, the speed of light.

For relativistic particles, we consider the expression

$$\langle \gamma^2 \rangle = 1 + \langle p_z^2 \rangle + \langle p_\perp^2 \rangle \qquad \text{(p2)}$$

where $\vec{p}$ is the particle momentum, and γ, the usual relativistic gamma factor. The brackets indicate averages over the fast temporal and longitudinal variations; i.e.,

$$\langle \varphi^2 \rangle = \varphi\varphi^* = |\varphi|^2 \tag{P3}$$

To calculate wave energy, we must pick only the first order times first order contributions. For the quantity $\langle p_\perp^2 \rangle$, this is straightforward:

$$p_\perp = \frac{e}{m} \frac{k_z c - \omega}{k_z c - \omega - \Omega} A_r \tag{P4}$$

using the dispersion relation

$$\omega = k_z c - \Omega \frac{k^2 c^2}{k^2 c^2 + \omega_p^2} \tag{P5}$$

we obtain

$$\langle p_\perp^2 \rangle = \frac{k^4 c^4}{\omega_p^2} \frac{e^2}{m^2} |A_r|^2 \tag{P6}$$

Here ω_p and Ω are the respective relativistic electron plasma and cyclotron frequencies.

The calculation of $\langle \gamma \rangle$ can be effected from the equation

$$\frac{d}{dt} \langle \gamma \rangle = \frac{e}{m} \langle E \cdot v \rangle = \frac{e}{m} \left[- \vec{v} \cdot \vec{\nabla} \varphi^* - \vec{v} \cdot \frac{\partial \vec{A}^*}{\partial t} \right] \qquad (P7)$$

Here, again, $\vec{v}$, φ, and $\vec{A}$ are calculated only to first order.

Using the relation

$$\frac{d}{dt} \langle \varphi^* \rangle = - v \cdot \nabla \varphi^* + i\omega \varphi^* \qquad (P8)$$

we obtain:

$$\frac{d}{dt} \langle \gamma + e/m \, \varphi^* \rangle = - \frac{e}{m} \frac{i\omega}{c} \langle \vec{v}_\perp \cdot \vec{A}_\perp \rangle \qquad (P9)$$

Here the quantity

$$\langle \varphi^* \rangle = \frac{\partial \varphi^*}{\partial r} \, \delta r \qquad (P10)$$

where δr is the first order radial variation and can be related to the perturbed density δn by the equation of continuity:

$$\delta n = - n_o \frac{1}{r} \frac{\partial}{\partial r} r \delta r \qquad \text{(P11)}$$

with

$$\Box \varphi = - 4\pi \, \delta n \, e \qquad \text{(P12)}$$

from Poisson's equation.

Finally, using Eq. (P4) (noting $v_\perp = p_\perp/\gamma$), we obtain the following expression for $\langle \gamma \rangle$:

$$\langle \gamma \rangle = - \frac{1}{4\pi \, n_o m} \left\{ \frac{k^2}{k_\perp^2} \left| \frac{\partial \varphi}{\partial r} \right|^2 + \frac{\omega_p^2 \, \omega\Omega}{n_o mc^2 \, |\omega - k_z c - \Omega|^2} \, |A_r|^2 \right\} \qquad \text{(P13)}$$

Here we have assumed $\omega^2 \ll k^2 c^2$.

We see that indeed the second order changes in $\langle \gamma \rangle$ are proportional to $J_1(k_\perp r)$ (i.e. A_1, $\partial_r \varphi$). Hence, energy transfer occurs near the edge of the beam and <u>not</u> at the origin.

<u>Wave Energy Equation</u>

To obtain the usual conservation equation of wave energy, we need the longitudinal component of Poynting flux S_z correct to second order:

$$S_z = \frac{c}{4\pi} (E_r B_\theta^* - E_\theta B_r^*) = \frac{c}{4\pi} \left[\frac{k^2}{k_\perp^2} \left| \frac{\partial \varphi}{\partial r} \right|^2 + 2\omega k_z |A_r|^2 \right] \tag{P14}$$

Defining the quantity W_z;

$$W_z \equiv n_o mc^2 \langle \gamma \rangle + S_z \tag{P15}$$

algebraic manipulation allows W_z to be expressed as

$$W_z = - \omega v_g \frac{(k^2c^2 + \omega_p^2)}{\omega_p^2 \Omega} \frac{|A_r|^2}{4\pi} \tag{P16}$$

where

$$v_g \equiv \frac{\partial \omega}{\partial k_z} = c \left[1 - \frac{2\omega_p^2 \Omega k_z c}{(k^2c^2 + \omega_p^2)^2} \right] \tag{P17}$$

Using the relation

$$|A_r|^2 = \frac{k^4 c^4}{(k^2c^2 + \omega_p^2)^2} \frac{\Omega^2}{k_\perp^2} |\varphi|^2 \tag{P18}$$

and

$$|E|^2 \cong k^2 |\varphi|^2 \tag{P19}$$

we then obtain

$$W_z = - v_g \frac{\omega\Omega}{\omega_p^2} \frac{k^2}{k_\perp^2} \frac{|E|^2}{4\pi} \qquad \text{(P20)}$$

which is indeed the usual wave energy flux expression.

Detailed Energy Balance

It is of interest to determine the amount of energy extracted from the streaming direction and utilized to grow and sustain the cyclotron wave. Utilizing Eq. (P2), we can compute to second order:

$$\langle p_z \rangle = \langle \sqrt{\gamma^2 - 1 - p_\perp^2} \cong \langle \gamma \rangle - \frac{\langle p_\perp^2 \rangle}{2\gamma} \qquad \text{(P21)}$$

Utilizing Eqs. (P6) and (P13) for $\langle p_\perp^2 \rangle$ and $\langle \gamma \rangle$, respectively, we obtain

$$\langle p_z \rangle = \frac{e^2 |A_r|^2}{m^2 c^2} \frac{(k^2c^2 + \omega_p^2)^2 k_\perp^2}{\omega_p^2 \Omega^2 \gamma k^2}$$

$$\times \left\{ - 1 - \frac{\omega\Omega}{\omega_p^2} \frac{k^2}{k_\perp^2} - \frac{k^2}{k_\perp^2} \frac{\Omega^2}{\omega_p^2} \left(\frac{k^2c^2}{k^2c^2 + \omega_p^2} \right)^2 \right\} \qquad \text{(P22)}$$

The three terms in the braces all represent energy drains on the parallel energy. The first term may be interpreted

as the contribution from $\langle p_z \rangle$ to the bare electromagnetic fields; the second term, the amount lost to growth mechanisms to establish the wave; and the third, the amount put into perpendicular particle motion required to constitute the wave.

APPENDIX Q

NONLINEAR FREQUENCY SHIFT OF BEAM CYCLOTRON MODE

In the linear theory of the electron beam cyclotron mode (which has been discussed in previous reports), the mode amplitude is assumed small. For finite mode amplitude, the nonlinearities may no longer be negligible, and they introduce the possibility of additional effects associated with resonant decay instabilities, nonlinear Landau damping, and frequency shifts. The mode does not appear to be subject to resonant decay instabilities; and for a cold electron beam, there is no nonlinear Landau damping. In this report, we focus our attention on the nonlinear modification of the beam cyclotron mode which is manifested in the appearance of a shift in the wave frequency. Such nonlinear frequency shifts may influence the time evolution of the beam cyclotron mode especially in situations where growth of the mode is determined by resonant coupling to another mode of the system.

It will be assumed throughout that a fluid description of the electron beam is adequate. In evaluating the nonlinear frequency shift, the procedure is to calculate the nonlinear generation of zeroth and second harmonic components of the fundamental. The nonlinear interaction of the fundamental with these harmonic components then leads to corrections to the linear dispersion relation.

A. Equilibrium

We consider a slab model equilibrium in which a cold relativistic electron beam of density N_o propagates with velocity $u_o \to c$ along a uniform guide field B_{oz} in the z-direction. The beam is infinite in the y-direction but bounded by conducting plates at $x = \pm a$.

The electron beam dynamics is described by the cold fluid equations:

$$\frac{\partial n}{\partial t} + \nabla \cdot n \underline{v} = 0$$

$$\frac{d}{dt} m \gamma \underline{v} = - e \underline{E} - \frac{e}{c} \underline{v} \times \underline{B}$$

$$\gamma = (1 - v^2/c^2)^{-1/2} \qquad \text{(Q 1)}$$

and closure is obtained through Maxwell's equations:

$$\nabla \times \underline{E} = -\frac{1}{c}\frac{\partial \underline{B}}{\partial t}$$

$$\nabla \times \underline{B} = \frac{1}{c}\frac{\partial \underline{E}}{\partial t} + \frac{4\pi}{c}\underline{J}$$

$$\nabla \cdot \underline{E} = 4\pi\rho$$

$$\nabla \cdot \underline{B} = 0 \qquad (Q2)$$

where

$$\rho = -en, \quad \underline{J} = -en\underline{v}$$

The velocities and electromagnetic fields of the beam equilibrium are:

$$\underline{v}_o = \left(0,\ v_{oy} = \frac{4\pi N_o ex}{B_{oz}\gamma_o^2}c \to 0,\ u_o\right)$$

$$\underline{E}_o = \left(E_{ox} = -4\pi N_o ex,\ 0,\ 0\right)$$

$$\underline{B}_o = \left(0,\ B_{oy} = -\frac{4\pi N_o e u_o x}{c},\ B_{oz}\right) \qquad (Q3)$$

where

$$\gamma_o = \left(1 - \frac{u_o^2}{c^2}\right)^{-1/2} \to \infty$$

B. Linear Theory

Let us define the new variables $A^{\pm}(\underline{r},t)$, $v^{\pm}(\underline{r},t)$:

$$A^{\pm} \equiv E_x \pm iE_y \pm \frac{iu_o}{c}(B_x \pm B_y)$$

$$v^{\pm} \equiv v_x \pm i\, v_y$$

From Eq. (Q2), we obtain the following equation for $A^{\pm}$:

$$\left(\nabla^2 - \frac{1}{c^2}\frac{\partial^2}{\partial t^2}\right) A^{\pm} = 4\pi \left(\frac{\partial}{\partial x} \pm \frac{i\partial}{\partial y}\right)\left(o - \frac{u_o}{c^2} J_z\right)$$

$$+ \frac{4\pi}{c^2}\left(\frac{\partial}{\partial t} + \frac{u_o \partial}{\partial z}\right)\left(J_x \pm i\, J_y\right) \qquad (Q\,4)$$

We restrict the discussion to perturbations with no variations in y $(\partial/\partial y = 0)$. If we consider

perturbations of the form $\exp(-i\omega t + i k_o z)$, then linearizing Eq. (Q1) and Eq. (Q4), we obtain

$$v^{\pm} = \frac{ie}{m\gamma_o} \frac{A^{\pm}}{(\omega - k_o u_o \pm \Omega)}$$

$$\frac{\partial^2}{\partial x^2} A^{\pm} + \varkappa^{\pm 2} A^{\pm} = 0$$

where

$$\varkappa^{\pm 2} = -k_o^2 + \frac{\omega^2}{c^2} - \frac{\omega_p^2 (\omega - k_o u_o)}{c^2 (\omega - k_o u_o \pm \Omega)}$$

$$\omega_p^2 = \frac{4\pi N_o e^2}{m \gamma_o}$$

$$\Omega = \frac{e B_o}{m \gamma_o c}$$

The boundary conditions at $x = \pm a$ are:

(1) $A^+ = A^-$

(2) $\frac{\partial A^+}{\partial x} + \frac{\partial A^-}{\partial x} = 8\pi [\rho - (u_o/c^2) J_z]$

If $k_o^2 c^2 > \omega^2$, $|\varkappa^- a| < 1$, the dispersion relation for the mode symmetric in E_z is given by

$$\omega = k_o u_o - \frac{\Omega k^2 c^2}{(k^2 c^2 + \omega_p^2)} \tag{Q5}$$

where

$$k^2 = \varkappa^{+2} + k_o^2$$

$$\tan \varkappa^+ a = - \varkappa^+ a$$

The corresponding eigenfunctions are:

$$A^+(x) = A_o \sin \varkappa^+ x$$

$$A^-(x) = A_o \frac{\sin \varkappa^+ a}{\sin \varkappa^- a} \sin \varkappa^- x$$

$$\approx A_o \sin \varkappa^+ a \cdot \frac{x}{a}$$

In order to calculate the nonlinear frequency shift, we therefore introduce the following expansion in terms of an ordering parameter ε:

$$A^{\pm}(\underline{r},t) = A^{(o)\pm}(\underline{r},t) + \epsilon\, A^{(1)\pm}(\underline{r},t) + \ldots$$

where $A^{(o)\pm}(\underline{r},t)$ are the linear solutions:

$$A^{(o)\pm}(\underline{r},t) = A_o^{\pm}(x,k_o)\ \exp(i\, k_o z)$$

$$+ A_o^{\pm *}(x,k_o)\ \exp(-\, i\, k_o\, z)$$

$$A_o^{+}(x,k_o) = \alpha\, e^{i\theta}\ \sin \varkappa^{+} x \equiv A_o \sin \varkappa^{+} x$$

$$A_o^{-}(x,k_o) = \alpha\, e^{i\theta}\ \frac{x}{a} \sin \varkappa^{+} a \equiv A_o\, \frac{x}{a} \sin \varkappa^{+} a$$

where the amplitude α and phase angle θ are given by

$$\frac{d\alpha}{dt} = \epsilon\, D_1(\alpha) + \epsilon^2\, D_2(\alpha) + \ldots$$

$$\frac{d\theta}{dt} = -\,\omega + \epsilon\, \Theta_1(\alpha) + \epsilon^2\, \Theta_2(\alpha) + \ldots \qquad (Q6)$$

ω is determined by Eq. (Q5), and $\varkappa^{+} a \approx 2$ for the mode with the smallest perpendicular wave number.

The variables n, $\underline{v}$, γ, $\underline{E}$, and B are similarly expanded in terms of ϵ:

$$n(\underline{r},t) = n^{(o)}(\underline{r},t) + \epsilon\, n^{(1)}(\underline{r},t) + \ldots$$

etc.

We consider the nonlinear terms in Eq. (Q1), Eq. (Q2), and Eq. (Q4), which are second order and third order in the amplitude of perturbations to be $0(\epsilon)$ and $0(\epsilon^2)$ respectively.

Thus, substituting these expansions in Eq. (Q1), Eq. (Q2), and Eq. (Q4), we generate to zero order in ϵ the linearized equations and we obtain for the linear solutions:

$$v^{(o)+}(x,k_o) = -\frac{ie}{m\gamma_o}\frac{k^2c^2}{\Omega\,\omega_p^2}\left(1 + \frac{\omega_p^2}{k^2c^2}\right) A_o^+(x,k_o)$$

$$v^{(o)-}(x,k_o) = \frac{ie}{m\gamma_o}\frac{1}{2\Omega}\, A_o^-(x,k_o)$$

$$v_z^{(o)} \to 0$$

$$n^{(o)} = \frac{e\,N_o\,k^2\,c^2}{2m\,\gamma_o\Omega^2\,\omega_p^2}\left[\left(1 + \frac{2\,\omega_p^2}{k^2c^2}\right)\frac{\partial}{\partial x}\,A_o^+ - \frac{1}{2}\,\frac{\partial}{\partial x}\,A_o^-\right]$$

$$\gamma^{(o)} = -\frac{e\,k^2x}{2m\,\Omega^2}\,A_o^+ - \frac{e}{2m\,\Omega^2}\,\frac{\partial}{\partial x}\,(A_o^+ + A_o^-)$$

$$E_z^{(o)} = \frac{ic}{2\Omega}\,\frac{\partial}{\partial x}\,(A_o^+ + A_o^-)$$

$$B_z^{(o)} = \frac{c}{2\Omega}\,\frac{\partial}{\partial x}\,(A_o^+ - A_o^-)$$

$$E^{(o)\pm} = \frac{c^2}{2\Omega^2}\,\frac{\partial^2}{\partial x^2}\,\{A_o^+ + A_o^-\}$$

$$B^{(o)\pm} = \pm\frac{ic^2}{2\Omega^2}\,\frac{\partial^2}{\partial x^2}\,(A_o^+ + A_o^-) \mp iA_o^\pm$$

where we have neglected terms of higher order in $\omega_p^2/k^2c^2 < 1$ and $1/\gamma_o^2 \ll 1$. For convenience, we will not always denote explicitly the arguments x, k_o, α, θ of the dependent variables.

C. First Order in ε

To first order in ε,

$$\left(\Theta_1 \frac{\partial}{\partial\theta} + D_1 \frac{\partial}{\partial\alpha}\right) v^{(o)\pm}(x, k_o)$$

$$+ \left[- \omega \frac{\partial}{\partial\theta} + ik_o u_o \mp i\Omega\right] v^{(1)\pm}(x, k_o)$$

$$+ \frac{e}{m\gamma_o}\left[A^{(1)\pm}(x, k_o) - \frac{v_z^{(1)}(x,k_o)}{c} B_{oy}\right] \approx 0 \qquad (Q7)$$

$$\left[- \omega \frac{\partial}{\partial\theta} + ik_z u_o \mp i\Omega\right] v^{(1)\pm}(x,k_z)$$

$$+ \frac{e}{m\gamma_o}\left[A^{(1)\pm}(x,k_z) - \frac{v_z^{(1)}(x,k_z)}{c} B_{oy}\right]$$

$$= \sum_{k_z=k_z'+k_z''} \left[- \frac{1}{2}\left\{v^{(o)+}(x,k_z') + v^{(o)-}(x,k_z')\right\}\right.$$

$$\times \frac{\partial}{\partial x} v^{(o)\pm}(x,k_z'')$$

$$- \left\{ \frac{ik_z u_o}{\gamma_o} \gamma^{(o)}(x,k_z') \mp \frac{ie}{m\gamma_o c} B_z^{(o)}(x,k_z') \right\}$$

$$\times v^{(o)\pm}(x,k_z'') \Big] \qquad (Q8)$$

$$\left(- \omega \frac{\partial}{\partial\theta} + ik_z u_o \right) v_z^{(1)}(x,k_z)$$

$$= \frac{e}{2m\gamma_o c} \sum_{k_z = k_z' + k_z''} \Big[\Big(\frac{u_o}{c} A^{(o)-}(x,k_z')$$

$$- \frac{i}{\gamma_o^2} B^{(o)-}(x,k_z') \Big) v^{(o)+}(x,k_z'')$$

$$+ \Big(\frac{u_o}{c} A^{(o)+}(x,k_z') + \frac{i}{\gamma_o^2} B^{(o)+}(x,k_z') \Big)$$

$$\times v^{(o)-}(x,k_z'') \Big] \qquad (Q9)$$

$$\left(\frac{\partial^2}{\partial x^2} - k_z^2 - \frac{\omega^2}{c^2} \frac{\partial^2}{\partial \theta^2} \right) A^{(1)\pm}(x,k_z)$$

$$+ \frac{4\pi\, eN_o}{c^2} \left[- \omega \frac{\partial}{\partial \theta} + i\, k_z u_o \right] v^{(1)\pm}(x,k_z)$$

$$- \frac{4\pi\, eu_o}{c^2} \frac{\partial}{\partial x} N_o\, v_z^{(1)}(x,\, k_z)$$

$$= - \frac{4\pi e}{c^2} \left(-\omega \frac{\partial}{\partial \theta} + i\, k_z u_o \right) \sum_{k_z = k_z' + k_z''} n^{(o)}(x,k_z')$$

$$\times\, v^{(o)\pm}(x,k_z'') \qquad \text{(Q10)}$$

Similar equations can be obtained for the remaining variables.

For $k_z = k_o$

$$v^{(1)\pm}(x,\, k_o) = 0$$

$$v_z^{(1)}(x,\, k_o) = 0$$

$$A^{(1)\pm}(x, k_o) = 0$$

and therefore

$$\Theta_1(\alpha) = 0$$

$$D_1(\alpha) = 0 \qquad \text{(Q11)}$$

For $k_z = 0$,

$$v^{(1)+}(x,0) = v^{(1)-*}(x,0)$$

$$= -\frac{i}{2\Omega}\left(\frac{e}{m\gamma_o\Omega}\right)^2 \frac{k^4c^4}{\omega_p^4}$$

$$\times \left[\left(1 + \frac{2\,\omega_p^2}{k^2c^2}\right) A_o^{+*} \frac{\partial}{\partial x} A_o^{+} - \frac{\omega_p^2}{2k^2c^2} \frac{\partial}{\partial x} A_o^{-*} A_o^{+}\right.$$

$$\left. - \frac{\omega_p^2}{k^2c^2} A_o^{+} \frac{\partial}{\partial x} (A_o^{+*} - A_o^{-*})\right]$$

$$v_z^{(1)}(x,0) = 0$$

$$n^{(1)}(x,0) = 0$$

$$\gamma^{(1)}(x,0) = 0$$

$$A^{(1)\pm}(x,0) = 0$$

For $k_z = 2k_o$

$$v^{(1)+}(x,2k_o) = i\left(\frac{e}{m\gamma_o\Omega}\right) A^{(1)+}(x, 2k_o)$$

$$- \frac{i}{2\Omega}\left(\frac{e}{m\gamma_o\Omega}\right)^2 \frac{k^4c^4}{\omega_p^4}$$

$$\times \left[\left(1 + \frac{7\,\omega_p^2}{k^2c^2}\right) A_o^+ \frac{\partial}{\partial x} A_o^+ + \frac{2\omega_p^2 x}{c^2} A_o^{+2}\right.$$

$$- \frac{1}{2}\frac{\omega_p^2}{k^2c^2} A_o^- \frac{\partial}{\partial x} A_o^+$$

$$\left. + \frac{\omega_p^2}{k^2c^2} A_o^+ \frac{\partial}{\partial x} A_o^- \right]$$

$$v^{(1)-}(x,2k_o) = \frac{i}{3}\left(\frac{e}{m\gamma_o\Omega}\right) A^{(1)-}(x,2k_o)$$

$$+ \frac{i}{12\Omega}\left(\frac{e}{m\gamma_o\Omega}\right)^2 \frac{k^2c^2}{\omega_p^2} A_o^+ \frac{\partial}{\partial x} A_o^-$$

$$A^{(1)+}(x,2k_o) = \frac{1}{4}\left(\frac{e}{m\gamma_o\Omega}\right) \frac{k^4c^2}{\Omega\,\omega_p^2} \frac{A_o^2}{\varkappa^+}$$

$$\times \left[\sin 2\varkappa^+x - \frac{x}{2a}\left(\sin 2\varkappa^+a + 2\varkappa^+a \cos 2\varkappa^+a\right)\right]$$

$$A^{(1)-}(x,2k_o) = \frac{1}{4}\left(\frac{e}{m\gamma_o\Omega}\right) \frac{k^4c^2}{\Omega\,\omega_p^2} \frac{A_o^2}{\varkappa^+} \frac{x}{2a}$$

$$\times \left[\sin 2\varkappa^+a - 2\varkappa^+a \cos 2\varkappa^+a\right]$$

$$E_z^{(1)}(x,2k_o) = \frac{ic}{4\Omega} \frac{\partial}{\partial x}\left[A^{(1)+}(x,2k_o) + A^{(1)-}(x,2k_o)\right]$$

$$B_z^{(1)}(x,2k_o) = \frac{c}{4\Omega} \frac{\partial}{\partial x}\left[A^{(1)+}(x,2k_o) - A^{(1)-}(x,2k_o)\right]$$

$$v_z^{(1)}(x,2k_o) = -\left(\frac{e}{m\gamma_o\Omega}\right)^2 \frac{k^2c}{4\omega_p^2} A_o^+ A_o^-$$

$$n^{(1)}(x,2k_o) = \frac{1}{16\pi} \frac{k^4c^4}{m\gamma_o\Omega^4\omega_p^2} \frac{\partial}{\partial x} A_o^+ \frac{\partial}{\partial x} A_o^+$$

$$\gamma^{(1)}(x,2k_o) = -\frac{\gamma_o}{8}\left(\frac{e}{m\gamma_o\Omega}\right)^2 \frac{k^4c^2}{\Omega^2\omega_p^2} \frac{\partial}{\partial x} xA_o^{+2}$$

$$-\frac{\gamma_o}{16}\left(\frac{e}{m\gamma_o\Omega}\right)^2 \frac{k^4c^2}{\Omega^2\omega_p^2} A_o^2\left[\cos 2\pi^+\pi - \cos 2\pi^+ a\right]$$

D. Second order in ϵ

To second order in ϵ,

$$\left[i\,\Theta_2 + D_2 \frac{\partial}{\partial\alpha}\right] v^{(o)\pm}(x,k_o)$$

$$+\left[-\omega\frac{\partial}{\partial\theta} + ik_o u_o \mp i\Omega\right] v^{(2)\pm}(x,k_o)$$

$$+\frac{e}{m\gamma_o} A^{(2)\pm}(x,k_o) = H^{\pm}(x,k_o) \qquad (Q12)$$

where $H^{\pm}(x,k_o)$ is determined by the substitution of the zero order and first order solutions in the nonlinear terms of Eq. (Q1) :

$$H^{+}(x,k_o) \approx \frac{\varkappa^{+2}}{4\Omega}\left(\frac{e}{m\gamma_o\Omega}\right)^3 \frac{k^4c^4}{\omega_p^4}\, h^{+}(x,k_o)\,|A_o|^2\, A_o$$

$$h^{+}(x,k_o) = \sin \varkappa^{+}x \left\{2 - \frac{\cos 2\varkappa^{+}a}{2} - \frac{\sin 2\varkappa^{+}a}{4\varkappa^{+}a}\right\}$$

$$- \sin 3\varkappa^{+}x$$

$$+ \frac{\varkappa^{+}x}{2}\,(\cos 3\varkappa^{+}x - \cos \varkappa^{+}x)$$

$$H^{-}(x,k_o) \approx -\frac{\varkappa^{+2}}{16\Omega}\left(\frac{e}{m\gamma_o\Omega}\right)^3 \frac{k^6c^6}{\omega_p^6}\, h^{-}(x,k_o)\,|A_o|^2\, A_o$$

$$h^{-}(x,k_o) = 3 \sin 3\varkappa^{+}x - \sin \varkappa^{+}x$$

we have neglected terms of higher order in $\omega_p^2/k^2c^2 < 1$ and $1/\gamma_o^2 \ll 1$.

For $A^{(2)\pm}(x,k_o)$, we obtain

$$\left(\frac{\partial^2}{\partial x^2} - k_o^2 + \frac{\omega^2}{c^2} \right) A^{(2)+}(x,k_o)$$

$$- i \frac{4\pi e N_o}{c^2} (\omega - k_o u_o) \, v^{(2)+}(x,k_o)$$

$$\approx - \left(\frac{e}{m\gamma_o \Omega} \right)^2 \frac{k^6 c^4}{8\Omega^2 \omega_p^4} A_o |A_o|^2 \, \varkappa^{+2}$$

$$\times \left[\sin 3\varkappa^+ x + \sin \varkappa^+ x \right] \qquad \text{(Q13)}$$

$$\left(\frac{\partial^2}{\partial x^2} - k_o^2 + \frac{\omega^2}{c^2} \right) A^{(2)-}(x,k_o)$$

$$- i \frac{4\pi e N_o}{c^2} (\omega - k_o u_o) \, v^{(2)-}(x,k_o)$$

$$\approx \left(\frac{e}{m\gamma_o \Omega} \right)^2 \frac{k^6 c^4}{16 \, \Omega^2 \omega_p^4} A_o \, |A_o|^2 \, \varkappa^{+2}$$

$$\times \left[3 \sin 3\varkappa^+ x - \sin \varkappa^+ x \right] \qquad \text{(Q14)}$$

We solve Eq. (Q12) for $v^{(2)\pm}(x,k_o)$ and substitute in Eq. (Q13) and Eq. (Q14). We multiply Eq. (Q13) by $A_o^+(x,k_o)$ and Eq. (Q14) by $A_o^-(x,k_o)$, and after integrating from $x = -a$ to $x = +a$, we sum the resulting equations:

$$\left[- \Theta_2 + \frac{iD_2}{\alpha} \right] g_1 + \frac{1}{4\Omega} \left(\frac{e}{m\gamma_o \Omega} \right)^2 \frac{k^2 c^2 \varkappa^+}{\omega_p^2 a} |A_o|^2 g_o = 0 \tag{Q15}$$

where

$$g_1 = 1 + \cos^2 \varkappa^+ a$$

$$g_o = \varkappa^+ \int_{-a}^{+a} dx \sin \varkappa^+ x \left[h^+(x) - \frac{(\sin 3\varkappa^+ x + \sin \varkappa^+ x)}{2} \right]$$

$$+ \frac{\varkappa^+ \sin \varkappa^+ a}{8} \int_{-a}^{+a} dx \frac{x}{a} \left[h^-(x) + 2\left(3 \sin 3\varkappa^+ x - \sin \varkappa^+ x\right) \right]$$

For $\varkappa^+ a \approx 2$

$g_o \approx 3.73$, $g_1 \approx 1.17$

Equating real and imaginary parts of Eq. (Q15),

$$D_2 = 0$$

$$\Theta_2 = \delta\omega \equiv \frac{g_o}{4\varkappa^+ a g_1} \frac{k^2c^2}{\omega_p^2} \left|\frac{e\varkappa^+ A_o}{m\gamma_o \Omega^2}\right|^2 \Omega \qquad \text{(Q16)}$$

Eq. (Q16) yields the shift $\delta\omega$ in the frequency due to nonlinearities.

The conditions for validity of the expansion utilized in deriving Eq. (Q16) are

$$\frac{1}{2} \frac{k^2c^2}{\omega_p^2} \left|\frac{e\varkappa^+ A_o}{m\gamma_o \Omega^2}\right| < 1$$

and

$$\delta\omega < \frac{\omega_p^2}{k^2c^2} \Omega$$

This calculation does not include changes in the time averaged variables which are produced by a time variation in the amplitude of perturbation. It is clear that such changes cannot be neglected if we are to properly discuss the effects of nonlinear frequency shifts on the evolution of an unstable wave growing from small amplitudes. We are continuing the analysis to determine the role of these time averaged changes induced by growing amplitude perturbations.

APPENDIX R

NONLINEAR EFFECTS FOR THE ELECTRON BEAM CYCLOTRON MODE

Much of the previous analysis of the Auto-Resonant Accelerator has been based upon the linear theory of the electron cyclotron mode, which is valid when the mode amplitude is sufficiently small. For example, the detailed investigation of various means of growing the cyclotron eigenmode has been conducted within linearized theory, as has the analysis of ion loading and acceleration. However, it is of interest to determine the mode amplitude level at which nonlinear effects first become important for a number of reasons:

(1) The successful functioning of the accelerator for nonlinear wave amplitudes has not yet been theoretically established (or disproven).

(2) Nonlinear effects may well cause saturation of the linear growth mechanisms, establishing an upper bound to the achievable mode amplitude.

(3) Theoretical knowledge of such nonlinear saturation amplitudes and mechanisms is needed for comparison with computational and experimental investigations.

(4) Knowledge of the magnitude and parameter scaling of nonlinear mode amplitudes is a valuable design tool, since this information bears heavily on the required length of both the growth and acceleration sections of the accelerator.

In this appendix, a brief survey of a number of nonlinear effects is presented, and rough estimates are given of the magnitude and scaling of the mode amplitude level at which these effects become important. Many of these effects may be seen to be related to one another. Although care has been taken to preserve the numerical coefficients for both Cartesian and cylindrical geometry, the very nature of these formulas is merely to indicate the level at which linear approximations lose their validity, and this occurs gradually rather than sharply as a function of amplitude.

Although it is possible in some cases to construct nonlinear theory which retains its validity to the point of growth saturation, so that the saturation amplitudes are known precisely, such investigations are not described herein. Consequently, the correlation between growth saturation and the breakdown of linear approximations must remain inferential, pending the accumulation of additional theoretical or computational evidence.

Finally, the effects discussed herein are confined to the electron-wave interaction; nonlinearities associated with ion dynamics or with a wave-growth inducing medium or additional driving fields are not considered.

The symbols which are used are defined below:

e, m = electron charge, mass

$\beta_o c$ = DC electron axial flow velocity

γ_o = $(1 - \beta_o^2)^{-1/2}$ = DC electron γ-factor

$\tilde{\gamma}$ = perturbed electron γ-factor

$n_o, \tilde{n}$ = DC, perturbed components of electron density

a, b = electron beam, wall radius

$\tilde{x}_\perp$ = perturbed radial (perpendicular) electron coordinate

$\tilde{\beta}_\perp c$ = perturbed radial (perpendicular) electron velocity

$\tilde{\beta}_z c$ = perturbed axial electron velocity

B_{oz} = external magnetic guide field

$k_\perp, k_z$ = perpendicular, axial components of wave vector

k^2 = $k_\perp^2 + k_z^2$

ω_p = $(4\pi\ n_o e^2/\gamma_o m)^{1/2}$ = relativistic electron plasma frequency

Ω = $(e\ B_{oz}/\gamma_o mc)$ = relativistic electron cyclotron frequency

$\delta\omega$ = $\Omega\ \omega_p^2/k^2c^2$

ω = frequency of electron cyclotron wave

Γ = linear growth rate of electron cyclotron wave

$\Delta\omega_{NL}$ = nonlinear frequency shift of electron cyclotron wave

$E_{o\perp}(x_\perp)$ = perpendicular component of DC electric field at radius $x_\perp$

$\tilde{E}_\perp(x_\perp)$ = perpendicular component of wave electric field at radius $x_\perp$

$\tilde{E}_z(x_\perp)$ = axial component of wave electric field at radius $x_\perp$

$\Phi_o(x_\perp)$ = DC electric potential function

$\tilde{\Phi}(x_\perp)$ = amplitude of perturbed electric potential

G = geometrical parameter = $\begin{cases} 1, \text{ cartesian (slab) geometry} \\ 2, \text{ cylindrical geometry} \end{cases}$

In addition, the above perturbed or wave quantities refer to the magnitude of the amplitude only; phase information is supressed.

The analysis which underlies these conditions of nonlinearity is based in part upon the following approximations:

$$\frac{b-a}{a} \ll 1 \qquad \text{(R1)}$$

$$\gamma_o \gg 1, \quad \beta \simeq 1, \quad \tilde{\beta}_z \ll 1 \qquad \text{(R2)}$$

axisymmetry, with $\tilde{E}_z(x_\perp) = \tilde{E}_z(-x_\perp)$ (R3)

$$\omega^2 \ll k_z^2 c^2 \qquad \text{(R4)}$$

$$k_z^2 + \frac{\omega_p^2}{2\,c^2} \ll k_\perp^2, \quad k_z\, a \simeq \frac{\Omega a}{c} \gg 1 \tag{R5}$$

Condition (R1) allows use of the analytically simple, one-region eigenmode. Condition (R2) implies strong decoupling of the longitudinal plasma mode from the cyclotron mode. Condition (R3) is a reminder that we have considered only the symmetric eigenfunctions. Condition (R4) for nonrelativistic wave speed is well satisfied for the proposed proof of principle Auto-Resonant Accelerator experiment, and allows simplification of the cyclotron eigenfunctions by decoupling the light modes. Condition (R5) implies strong decoupling of the positive and negative energy cyclotron modes, and also allows simplification of the cyclotron eigenfunctions.

Subject to these approximations, one finds the following radial mode structures:

$$\tilde{\Phi}(x_\perp) = \tilde{\Phi}(o)\left[J_o(k_\perp r)\,,\ \cos(k_\perp x_\perp)\right] \tag{R6}$$

$$\tilde{E}_\perp(x_\perp) = k_\perp \tilde{\Phi}(o)\left[J_1(k_\perp r)\,,\ \sin(k_\perp x_\perp)\right] \tag{R7}$$

$$\tilde{E}_z(x_\perp) = k_z \tilde{\Phi}(o)\left[J_o(k_\perp r),\ \cos(k_\perp x_\perp)\right] \tag{R8}$$

$$\tilde{x}_\perp(x_\perp) = \frac{k^2c^2}{\omega_p^2}\,\frac{e\tilde{\Phi}(o)}{\gamma_o mc^2}\,\frac{1}{k_\perp}\left[J_1(k_\perp r),\ \sin(k_\perp x_\perp)\right] \tag{R9}$$

$$k_\perp a \simeq 1 + G \quad \text{(for the broadest eigenmode)} \tag{R10}$$

$$\Phi_o(x_\perp) \simeq 2\pi e\, n_o\, x_\perp^2/G = \frac{1}{2}\, x_\perp\, E_{o\perp}(x_\perp) \tag{R11}$$

where the Bessel functions apply for cylindrical geometry and the trigonometric functions for slab geometry.

The various conditions wherein nonlinear effects become significant are listed below for ready comparison with one another; a discussion of the different nonlinear effects follows.

$$\frac{\tilde{n}}{n_o} \simeq \frac{k^2c^2}{\omega_p^2}\,\frac{e\tilde{\Phi}(o)}{\gamma_o mc^2} \geq 1 \tag{R12}$$

$$k_\perp\, \tilde{x}_{\perp max} \simeq \frac{k_\perp c\tilde{\beta}_\perp}{\Omega} \simeq \left|\frac{\partial \tilde{x}_\perp}{\partial x_\perp}\right|_o \simeq \frac{1}{G}\,\frac{\tilde{n}}{n_o} \geq 1 \tag{R13}$$

$$\frac{\tilde{E}_\perp(o)}{E_{o\perp}(a)} \simeq k_\perp a \frac{\tilde{E}_{\perp max}}{E_{o\perp}(a)} \simeq \frac{(k_\perp a)^2}{2G} \frac{\tilde{\Phi}(o)}{\Phi_o(a)} \simeq \frac{k_\perp^2}{k^2} \frac{\tilde{n}}{n_o} \gtrsim 1 \qquad \text{(R14)}$$

$$\tilde{\beta}_\perp \simeq \frac{k_z}{k_\perp} \left| \frac{\partial \tilde{x}_\perp}{\partial x_\perp} \right|_o \gtrsim 1 \qquad \text{(R15)}$$

$$\frac{\tilde{\gamma}}{\gamma_o} \simeq \tilde{\beta}_\perp \frac{E_{o\perp}(a)}{B_{oz}} \left[1 + \left(\frac{G^2 k_\perp a}{k^2 a^2} \right)^2 \right]^{1/2}$$

$$\simeq \left(\frac{\omega_p^2 a^2}{k_\perp a G^2 c^2} \right) \left[1 + \left(\frac{G^2 k_\perp a}{k^2 a^2} \right)^2 \right]^{1/2} \frac{\tilde{n}}{n_o} \gtrsim 1 \qquad \text{(R16)}$$

$$\frac{\delta_\gamma |\omega - k_z c \beta_z + \Omega|}{\delta\omega} \simeq \frac{k^2 c^2}{\omega_p^2} \frac{\tilde{\gamma}}{\gamma_o} \simeq \left[1 + \left(\frac{k^2 a^2}{G^2 k_\perp a} \right)^2 \right]^{1/2} \frac{\tilde{n}}{n_o} \gtrsim 1$$

(R17)

$$\frac{\delta_\beta \left|\omega - k_z c\beta_z + \Omega\right|}{\delta\omega} \simeq \frac{\left[1 + \left(\frac{\gamma_o \omega_p^2 a^2}{k_\perp a G^2 c^2}\right)^2\right]^{1/2}}{\gamma_o^2} \left(\frac{\tilde{n}}{n_o}\right)$$

$$+ \frac{k_z^2}{k^2} \frac{G^2 c^2}{2\omega_p^2 a^2} \left[\frac{k^2 a^2}{G^2 k_\perp a} \frac{\tilde{n}}{n_o}\right]^2 \geq 1 \qquad \text{(R18)}$$

$$\left.\frac{\Delta\omega_{NL}}{\Gamma}\right|_{slab} \simeq H(kc, \omega_p, \ldots) \frac{\delta\omega}{\Gamma} \left(\frac{\tilde{n}}{n_o}\right)^2 \geq 1 \qquad \text{(R19)}$$

Condition (R12) prescribes the wave amplitude level at which the electron density fluctuations due to the wave become comparable with the mean electron density. These density fluctuations will be strongest on axis, and at this wave amplitude the electron density will vary from near zero to around twice the ambient density.

Condition (R12) also indicates that these density nonlinearities will become important at an amplitude level smaller by ω_p^2/k^2c^2 from that for which longitudinal trapping of the electrons by the wave potential would occur.

Condition (R13) indicates three nonlinear effects where each occurs at a wave amplitude higher than that for density nonlinearities by only the geometrical factor. The first of these is the condition that the radial displacement of an electron by the wave be as large as the scale length $k_\perp^{-1}$ characterizing the perpendicular eigenmode structure. This is judged to be more accurate than the criterion for displacements as large as the beam radius, which requires higher wave amplitudes. Equation (R9) indicates that the displacements will be largest at about 0.8 times the beam radius. One physical consequence of radial displacements as large as $k_\perp^{-1} \simeq a/(1+G)$ is that wall collisions might occur unless a sufficiently wide vacuum gap was available. The second condition in Eq. 9r13) is that finite electron gyroradius effects become important because of the perpendicular kinetic energy excited by the wave. The third condition is that the radial motion of the electrons becomes nonlaminar by virtue of radial "crossings" of electron trajectories. This may be easily seen to occur when $|\partial \tilde{x}_\perp / \partial x_\perp|$ exceeds 1, which occurs

first for particles on axis. These last two conditions in Eq. (R13) are symptomatic of the breakdown of the fluid nature of the wave due to nonlinear turbulence.

Condition (R14) prescribes when the perpendicular wave electric field exceeds the self radial field of the beam, which tends to occur first on axis. This requires a wave amplitude larger than that for density nonlinearity by only $k^2/k_\perp^2$. Condition (R14) also reveals the connection between these various criteria of nonlinearity and the measurable ratios such as $\tilde{E}_{\perp max}/E_{o\perp}(a)$ which are conveniently extracted from computer simulations as a diagnostic. One physical consequence of the nonlinearity suggested by Eq. (R14) is the possibility of electron field emission at the conductor walls. The self-field $E_{o\perp}$ is typically much larger than the threshold amplitude required for field emission, but is in the wrong direction. One might think that if the wave fields became larger than the self-field and had the opposite radial sense, then field emission might result. However, this is a deception of the linear theory which is breaking down, since Poisson's equation shows that even for nonlinear waves, the electrostatic

portion of the electric field must always point toward a region of net negative charge. Hence, the only possibility of field emission is due to the inductive or electromagnetic portion of the electric field, which is small for nonrelativistic phase velocity, or to the presence of the ions whose density might locally exceed the nonlinearly reduced electron density. To quantify this criterion for field emission would require a detailed analysis of the ion dynamics, which is not presented herein. However, one suspects that the required ion density would be a significant fraction of the electron density, since the electron wave fields are geometrically reduced below their peak value at the walls, and the peak value does not exceed the self-field until $(\tilde{n}/n_b) \geq k^2a^2/k_\perp a$ according to Eq. (R14).

Condition (R15) for the radial electron oscillations in the wave to become relativistic will be stronger than condition (R13) only if k_z exceeds $k_\perp$. It is possible that this might be modestly true in the growth section and at the beginning of the accelerator section, but toward the end of the accelerator section k_z will be below $k_\perp$ and $\tilde{\beta}_\perp << 1$.

The significance of the $\tilde{\beta}_\perp \geq 1$ nonlinearity is that it implies a significant fluctuation $\tilde{\gamma}$ in the electron γ-factor as shown in condition (R16). This occurs because the electrons are perturbed by the wave to move with or against the radial self-field of the beam. At the beginning of the accelerator where $\tilde{\beta}_\perp$ is largest, $E_{o\perp}(a)/B_{oz}$ is smallest and may be somewhat less than 1. The net product of these terms yields an expression, also shown in Eq. (R16), which indicates that $\tilde{\gamma}/\gamma_o$ is generally somewhat less than $\tilde{n}/n_o$.

However, condition (R17) indicates that the variation $\tilde{\gamma}/\gamma_o$ is magnified by k^2c^2/ω_p^2 to produce a variation in the fluid electron cyclotron resonance $|\omega - k_z c\beta_z + \Omega|$ which may be comparable to its ambient value (i.e., $\delta\omega$). This nonlinear spreading of the cyclotron resonance occurs due to the γ-dependence of Ω; it is sometimes called "resonance broadening." It is also symptomatic of the breakdown of fluid theory and the conversion of the cyclotron mode to a kinetic regime due to nonlinear turbulence. Condition (R17) indicates that this nonlinear resonance broadening effect is felt at

wave amplitudes somewhat below those for density nonlinearity, and hence is the most sensitive nonlinear effect yet discussed. Experience would suggest that this resonance broadening would reduce the wave growth rate when the wave amplitude reaches the level given by Eq. (R17).

Condition (R18) gives the corresponding resonance broadening which occurs due to changes in the axial electron velocity. The first terms of Eq. (R18), which are linear in the wave amplitude $\tilde{n}/n_o$, are relatively unimportant as usual for $\gamma_o >> 1$. However, the last term of Eq. (R18), which is quadratic in the wave amplitude, may be seen to be more (or less) important than the $\tilde{\gamma}/\gamma$ resonance broadening, depending on whether $k_z^2 G^2 c^2 / 2k^2 \omega_p^2 a^2$ is greater (or less) than 1. This quadratic term in the wave amplitudes reflects the perturbation in $\tilde{\beta}_z$ due to linear perturbations in $\tilde{\beta}_\perp$, according to

$$\tilde{\beta}_z \simeq -\frac{1}{2}\tilde{\beta}_\perp^2 + \text{linear terms} + \text{other quadratic terms} \qquad \text{(R20)}$$

which follows immediately from a perturbation expansion of the definition of $\gamma(\beta)$. For the parameters which have been proposed for the proof of principle experiment on Auto-Resonant acceleration, assuming $k_z \sim k_\perp$ at the beginning of the accelerator, one may see that conditions (R17) and (R18) "trigger" at roughly the same wave amplitude.

With the exception of the final term in Eq. (R18), the effect of nonlinearities has only been explored so far through the retention of terms which are linear in the wave amplitude. In an attempt to examine nonlinear effects which are quadratic in the wave amplitude, a calculation is begun in Appendix Q which seeks the nonlinear shift in the frequency of the electron cyclotron wave due to nonlinear coupling to harmonics of the linear eigenmode. Although this calculation is presently incomplete as mentioned in Appendix Q, the result will scale generally as indicated in condition (R19). The frequency shift will be quadratic in the wave amplitude, and it is believed that the coefficient function H is at least order unity. It is speculated that when this

nonlinear frequency shift exceeds the linear growth rate Γ of the cyclotron wave, the growth will be strongly modified. For growth mechanisms such that $\Gamma \ll \delta\omega$, which is the regime of validity of Eq. (R19), one sees that this nonlinear effect may appear much sooner than the density nonlinearities and even sooner than resonance broadening effects. In the competition between Eq. (R17) and (R19), a low value of Γ favors (R19) while a high value of $k_z a$ favors Eq. (R17). Of course, if $k_z a$ is too large, the cyclotron eigenfunctions should be reevaluated due to the violation of assumption (R5).

It is important to notice that the mode amplitude at which these nonlinear effects appear is reduced for higher values of k^2. Consequently, one would expect the higher-k modes to saturate in growth at lower amplitudes than the lower-k modes. When exciting or growing the cyclotron wave, care should be taken (as in designing computer simulations) that the lowest k mode is not discriminated against by any frequency or wavenumber selection which may be imposed.

It should not be inferred that this list of electron nonlinearities is complete, or that there are not other important nonlinear effects. For example, the possibility of a nonlinear three-wave decay instability was previously examined and found to be disallowed by the coupling selection rules. There are also a number of ion nonlinear effects which could produce saturation of electron-ion instabilities, for example, at wave amplitudes which may be below those discussed here in some cases.

APPENDIX S

COMPUTER SIMULATION OF THE RESISTIVE GROWTH AND SATURATION OF THE ELECTRON CYCLOTRON MODE

Explanation of Code

The simulations were performed with a two dimensional simulation code fully described in Ref. 6. The code is a two dimensional Cartesian, relativistic, fully electromagnetic particle code.

The code has been modified as described in Ref. 7 to eliminate the numerical Cherenkov instability.

The primary additional modification made to the code as previously described is the inclusion of a nonisotropic, homogeneous resistive medium in the code. This is implemented by modifying the x component of the current as shown

---

6. Drobot, Adam T., "Theory and Experiments in the Simulation of Collisionless Plasmas" (unpublished dissertation, Fusion Research Center, Univ. of Texas at Austin, 1974).

7. Drummond, W. E., et al. "Turbulent Heating of Plasmas by High Energy Beam," Interim Scientific Report, AFOSR Contract No. F44620-72-C-0071. Arlington, Virginia: Air Force Office of Scientific Research, Aug. 1975.

below

$$J_x = J_{px} + \sigma E_x \tag{S1}$$

where J_{px} is the x component of the particle current

$$J_{px}(\underline{x}_m) = e \sum_{\ell} V_x(\ell)\, S(\underline{x}_\ell - \underline{x}_m) \tag{S2}$$

ℓ = part. index

computed in the normal manner by bilinear interpolation.

The σE_x addition to the current will simulate the action of a nonisotropic resistive medium distributed throughout the volume of the beam. This correction is made at every mesh point at which the J_x current is defined. The purpose of the correction is to render the negative energy electron cyclotron mode unstable. The linear theory and dispersion relations for this case are worked out in Appendix T.

The motivation for simulating the distributed resistivity case rather than having the resistivity concentrated in the wall is computational convenience. An additional motivation is an enhanced growth rate. This

will become evident when one considers the complications involved in simulating a resistive liner.

In order to solve the fields in the liner, it is necessary to either implement an appropriate jump condition at the boundary or else solve for the fields across a transition region which is of order c/σ wide. This would imply a very tiny Eulerian cell width and consequently a large number of cells. Implementing jump conditions at the boundary would involve putting in special logic to determine where the boundary lay, and then inserting a jump in the appropriate quantity. Either one of these would require a significant amount of reprograming.

Another reason for using distributed resistivity is that the growth rate turns out to be higher than if the resistivity is concentrated in the walls. The reason for this is the E_x field is a monotonic decreasing function of the radial coordinate in the walls. It is therefore evident that more energy will be dissipated the further in the resistive liner extends. Because of

the negative energy character wave, this results in a higher growth rate.

It may also be expected that the nonlinear saturation mechanism for the distributed resistivity model will probably give valuable insight to the nonlinear saturation of the resistive liner configuration.

The format of the runs was to allow the unstable wave to grow from noise. We could then determine at what level saturation occurred and if any other unstable waves would grow. Letting the wave grow from noise dictates long computer runs since the wave must grow by four to five orders of magnitude before nonlinear effects might become important and also because it typically takes 1500 to 2000 time steps before the wave becomes discernible from noise.

The first simulation run has the following parameters.

$$\Omega_o \Delta t = 0.3$$

$$\omega_{po} \Delta t = 0.122$$

$$4\pi\sigma\Delta t = 0.0500$$

where

$$\Omega_o = e B_x / me c$$

$$\omega_{po} = \frac{4\pi e n_e^2}{m_e}$$

e = electronic charge

B_x = applied guide field

m_e = electron mass

c = velocity of light

$c \Delta t/\Delta y = 0.350$

$c \Delta t/\Delta x = 0.477$

Δt = time step

Δx = longitudinal cell size

Δy = transverse cell size

$Nx = 40$

= number of active cells in longitudinal direction

$Ny = 13$

= number of active cells in transverse direction.

Figure S1 shows that the most unstable mode corresponds to one wavelength in the machine length. The graph represents the amplitude of the longitudinal E field as a function of longitudinal position. By comparing such graphs produced at different points in time, it is possible to calculate a phase velocity of approximately 0.1c.

Figure S2 shows E_x^2 plotted as a function of time. The growth rate associated with the amplitude of E_x is $3.01 \times 10^{-3} \Omega_o$ as shown in Figure S2. This corresponds to a growth rate of 379 time steps per e-folding.

The linear theory for this case presented in Appendix T gives a growth rate of

$$\Gamma = \frac{4\Omega\ \omega_p^2\ a^2/c^2}{|k_x^2\ a^2 + 4 + \omega_p^2\ a^2/c^2|^2} \quad \frac{1/2\ \omega\Omega}{\omega^2 + 1/4\ \Omega^2} \tag{S3}$$

where

$\Omega = \Omega_o/\gamma$

$\omega_p^2 = \omega_{po}^2/\gamma$

a = beam radius

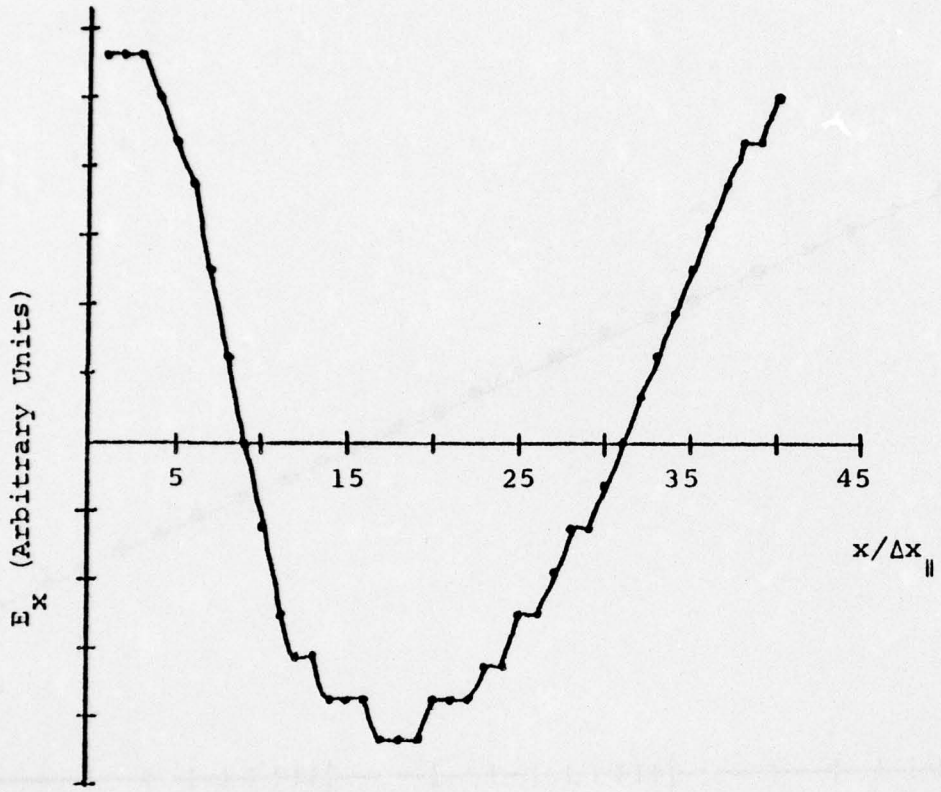

Figure 51. E_x vs. x at τ = 3200

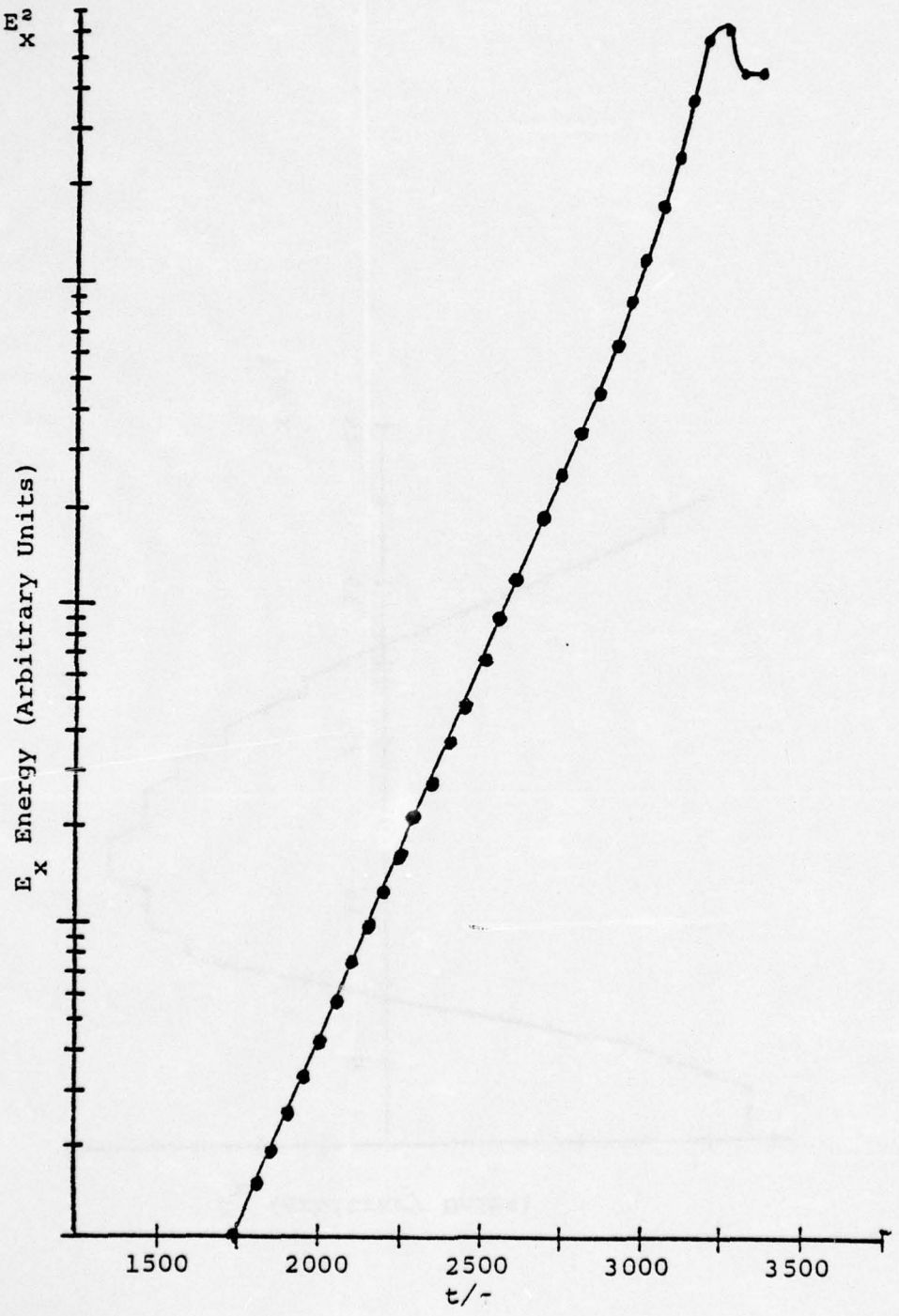

Figure S2. E_x Energy vs. t

If we assume that $\omega \ll \Omega$ and observe that for the parameters specified earlier

$$\frac{\omega_p^2 a^2}{c^2} = 1.711$$

$$K_x a = 1.39$$

the theoretical e-folding time turns out to be 429 time steps per e-folding. This constitutes reasonable theoretical agreement.

Figure S2 shows that the amplitude of the E_x field takes a dip close to the end of the simulation. The total energy (particle plus field) increases by about 4 parts in a thousand during this same interval. total energy had been constant to within one part in 10^4 until this point in the run, it is probable that this dip is due to loss of numerical energy conservation.

The maximum E_x field amplitude reaches 1/18 of the radial E field amplitude at its peak. This is probably too low for nonlinear effects to become important.

The plasma parameters of the second and third simulations are the same.

$$\frac{\Omega a}{c} = 1.85$$

$$\frac{\omega_p^2 a^2}{c^2} = 0.413$$

a = beam radius

c = velocity of light

The first simulation was carried out on a 15 by 42 mesh with 3174 particles. The beam was initially filled half way to the wall. The simulation was run a total of 10500 time steps. A plot of E_x energy versus time is shown in Figure S3. It yields an amplitude growth rate

$$\Gamma = 3.56 \times 10^{-3} \ \Omega$$

The approximate growth rate from the linear theory is

$$\Gamma = 1.86 \times 10^{-3} \ \Omega_o$$

or approximately half the observed growth rate. This constitutes reasonable agreement since some of the approximations made in the theory are not well satisfied in the simulation.

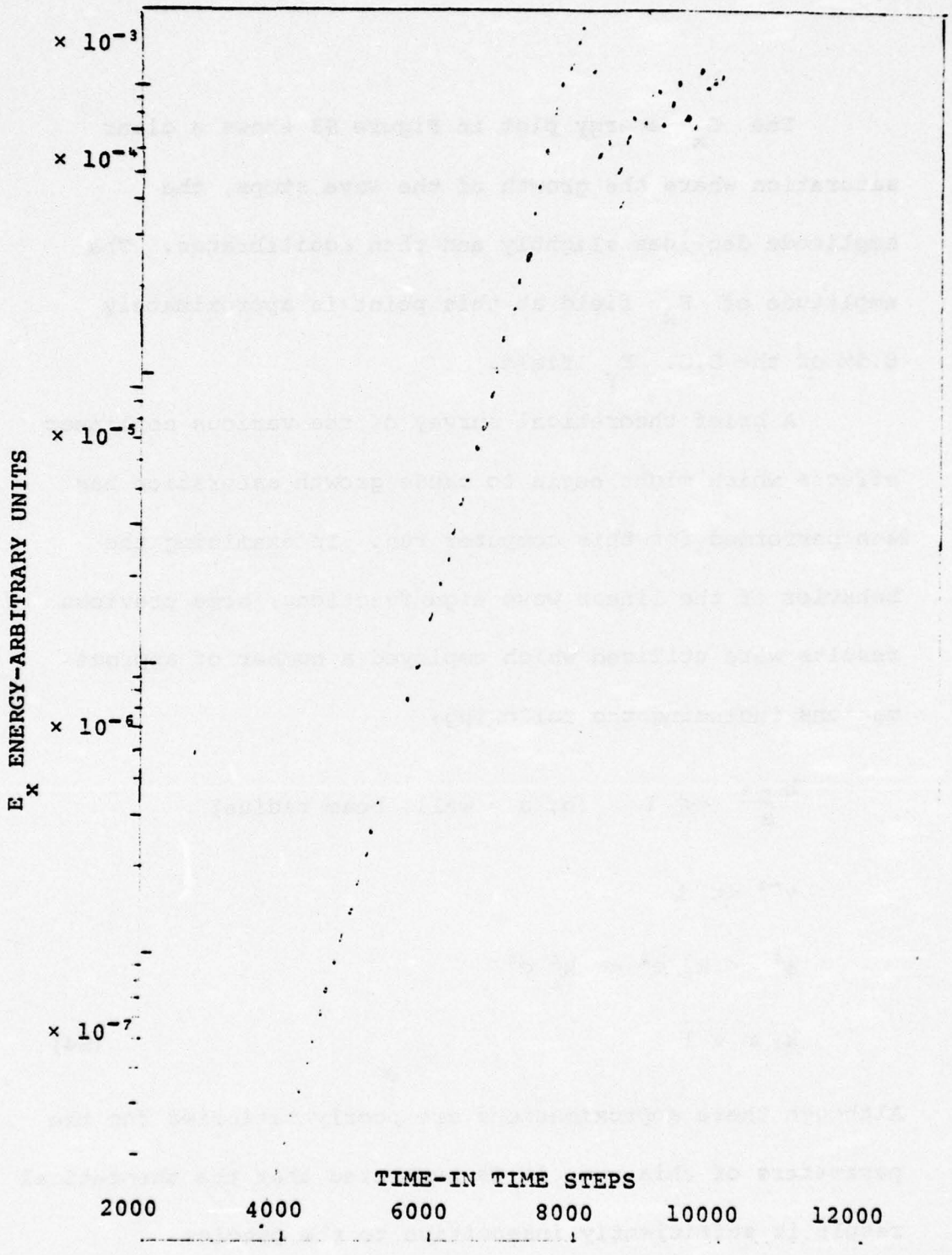

Figure S3. E_y Energy vs. Time-Run 1

The E_x energy plot in Figure S3 shows a clear saturation where the growth of the wave stops, the amplitude declines slightly and then equilibrates. The amplitude of E_x field at this point is approximately 8.5% of the D.C. E_y field.

A brief theoretical survey of the various nonlinear effects which might begin to cause growth saturation has been performed for this computer run. In examining the behavior of the linear wave eigenfunctions, some previous results were utilized which employed a number of approximations including the following:

$$\frac{b-a}{a} \ll 1 \quad (b, a = \text{wall, beam radius})$$

$$\gamma^{-2} \ll 1$$

$$\omega^2 \ll k_\parallel^2 c^2 \ll k_\perp^2 c^2$$

$$k_\parallel a \lesssim 1 \qquad \text{(S4)}$$

Although these approximations are poorly satisfied for the parameters of this run, it is suspected that the theoretical result is sufficiently insensitive to the precise

eigenmode structure that the results of the calculation may remain valid within a factor of perhaps 3.

One of the first nonlinear effects that appears to be encountered for this run is that fluctuations in the electron γ-factor, which occur as the electrons are radially perturbed to travel through the DC radial electric field, may effectively broaden the electron cyclotron resonance $|\omega - k_\parallel c\beta + \Omega|$ beyond the bounds of cold fluid theory when the wave field reaches the level

$$\frac{\tilde{E}_x}{E_{\perp DC}} \sim \frac{(k_\parallel a)(k_\perp a)}{k^4 a^4} \sim 0.04 \qquad (S5)$$

In addition, the perpendicular component of the electron velocity may become relativistic at a field amplitude a few times larger than this.

Although there is no certainty that these nonlinear effects will cause wave growth saturation, it is possible that saturation will result, and this provides an amplitude level which may be compared with the observed computer calculation results.

The momentum of the particles drops by approximately 9% during the time period from 4800 time steps to 8500 time steps. This indicates that the wave energy is being extracted from the streaming energy of the electrons.

A plot of total energy versus time is shown in Figure S4. The total loss of energy is approximately 5% of the initial energy. Some of this energy loss may be accounted for by energy dissipation in the resistive media. The rest of the loss must be accounted for in terms of truncation errors made by the code.

The third simulation had the same plasma parameters as the second run. However, the conducting walls were brought in much closer to the beam. The initial fill had the beam radius equal to 0.928 times the wall radius. This run corresponds more closely to the linear theory since the theory assumed the beam radius approximately equal to the wall radius.

Figure S5 shows E_x energy as a function of time. The amplitude growth rate for this case is

$$\Gamma = 4.66 \times 10^{-3}\ \Omega_o \qquad \text{(S6)}$$

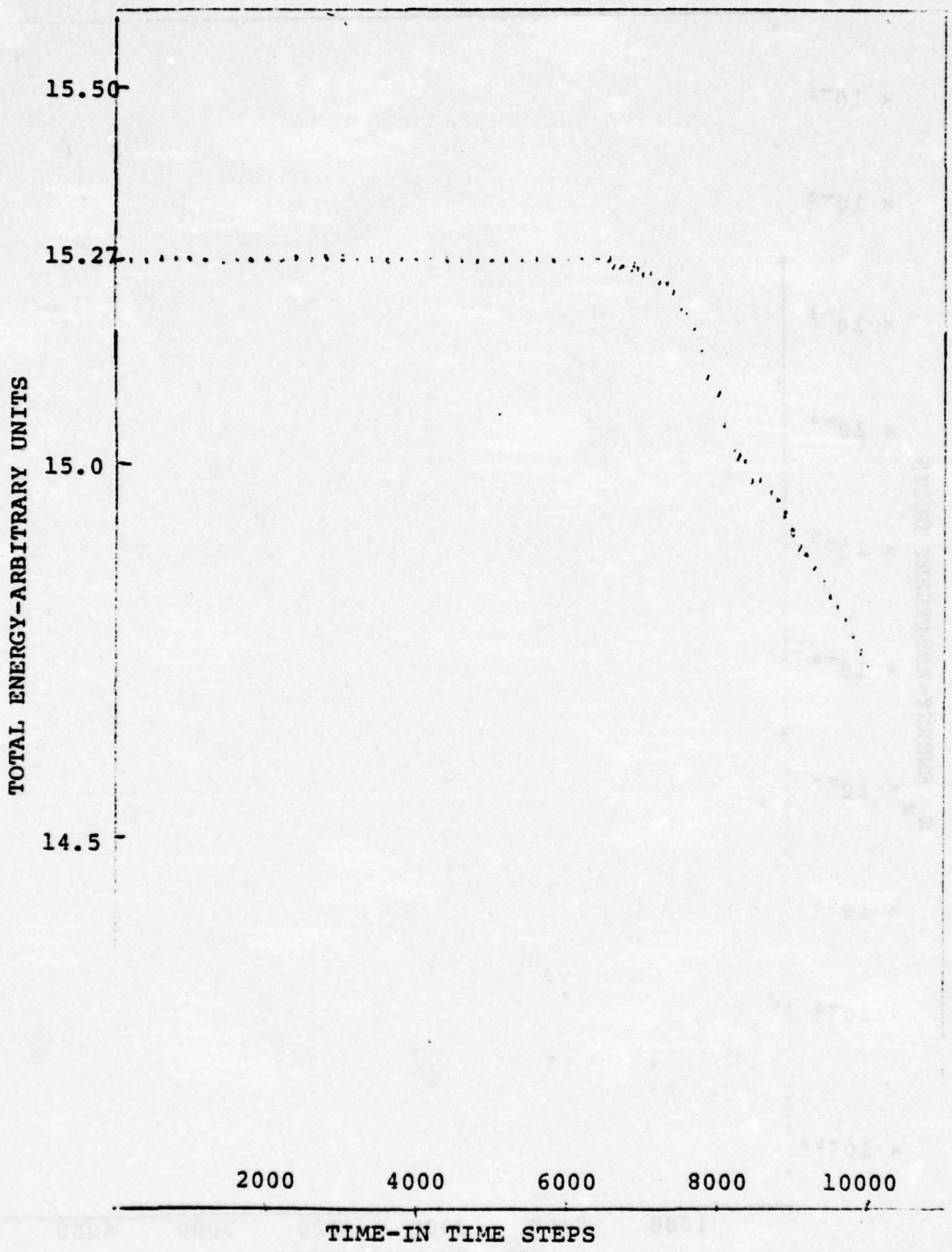

Figure S4. Total Energy vs. Time

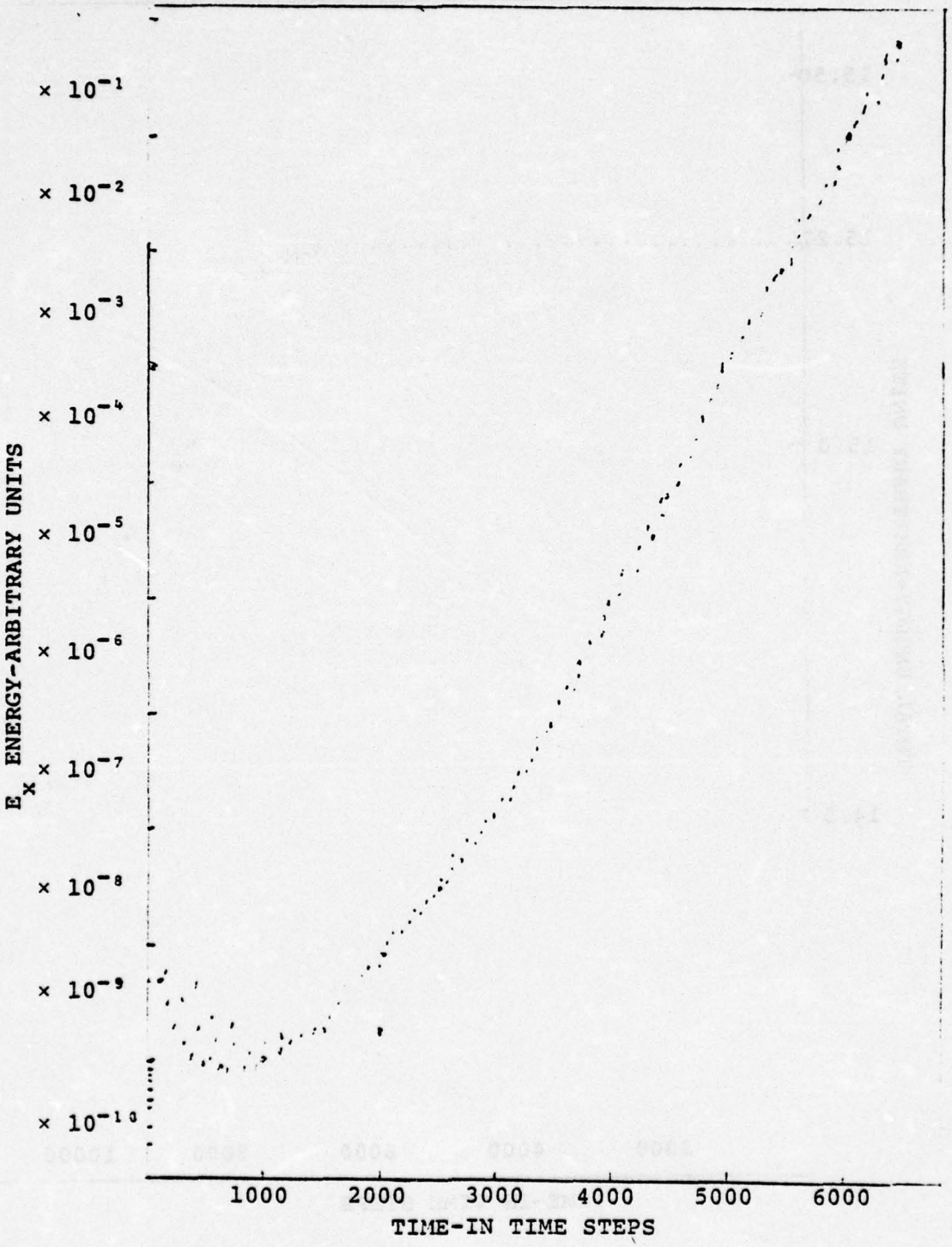

Figure S5. E_x Energy vs. Time-Run 2

The corresponding linear growth rate is

$$\Gamma = 2.03 \times 10^{-3}\ \Omega_o \qquad \text{(S7)}$$

The energy conservation for this run was within 0.7% for the first 4800 time steps and within 2.6% for the first 5600 time steps. The amplitude of the E_x field is 8.6% of the D.C. transverse field at 4800 time steps and 22.4% of the D.C. transverse field at 5600 time steps.

The three simulation runs tend to indicate that E_x can reach approximately 15% of the transverse D.C. electric field before saturation. This is with no effort being made to maximize saturation level. It must also be pointed out that energy conservation became a serious problem towards the end of these runs. The validity of these results can be trusted only as long as the energy conservation remains good.

Extra diagnostics have been added to the code which involve doing longitudinal fast Fourier transforms on selected field and current components at selected transverse locations. These show both phase and magnitude of the selected Fourier components so that we can deduce phase velocity and ω of the various modes we wish to analyze. This package involves using the FFT routines in the IMSL Library.

APPENDIX T

GROWTH OF THE CYCLOTRON WAVE BY AN ANISOTROPIC RESISTIVE BACKGROUND

Introduction

In this appendix we derive the dispersion relation for a relativistic slab of electrons propagating inside a perfectly conducting waveguide in which there is a guide magnetic field and an anisotropic resistive plasma which obeys

$$J_{px} = 0 = J_{py}$$

$$J_{pz} = \sigma E_z \tag{T1}$$

where $\vec{J}_p = (J_{px}, J_{py}, J_{pz})$ is the plasma current, E_z is the component of the electric field in the $+z$ (propagation) direction, and σ is the (constant) plasma conductivity. From this dispersion relation we will obtain estimates of the growth rate of the symmetric, lower Doppler shifted cyclotron eigenmode.

Equilibrium Solution

We choose rectangular Cartesian coordinates (x, y, z) with the beam propagating in the +z direction with velocity $v_z \simeq c$, where c is the velocity of light in vacuum. The beam is assumed to extend from $x = +a$ to $x = -a$ in x and is assumed to be of infinite extent in y and z. The guide magnetic field is given by $\vec{B}_g = B_o \hat{z}$ with B_o constant. We shall also assume that the beam is extremely relativistic, i.e. $\gamma >> 1$ where $\gamma \equiv (1 - v^2/c^2)^{-1/2}$.

For our equilibrium solution we take the "rigid rotor" solution to the Maxwell-Lorentz equation, which is ($c = 1$)

$$E_x = 4\pi \eta_o e x \qquad B_y = 4\pi \eta_o e v_z \tag{T2}$$

$$E_y = E_z = 0 \qquad B_x = 0 \tag{T3}$$

$$B_z = B_o \sqrt{1 - \frac{\omega_p^4 (a^2 - x^2)}{\Omega^2 \gamma^2}} \approx B_o \tag{T4}$$

$$v_y \cong - \frac{\omega_p^2}{\Omega\gamma^2} \frac{x}{\sqrt{1 - \frac{\omega_p^4 (a^2 - x^2)}{\Omega^2 \gamma^2}}} \ll 1 \qquad \text{(T5)}$$

$$v_z \simeq 1 \qquad v_x = 0 \qquad \text{(T6)}$$

where

$$\omega_p^2 \equiv \frac{4\pi \eta_o e^2}{m\gamma} \qquad \text{(T7)}$$

$$\Omega \equiv \frac{eB_o}{\gamma m} \qquad \text{(T8)}$$

and η_o is the (constant) beam particle density; (e/m) is the charge to mass ratio of the electron. In Eqs. (T2) through (T6) we take

$$\gamma >> 1 \qquad \text{(T9)}$$

and

$$\frac{\omega_p^2}{\Omega\gamma^2} \ll 1 \qquad \text{(T10)}$$

Condition (T10) is equivalent to

$$J_{KA} \ll 1.6 \, B_{KG}/a_{cm} \qquad \text{(T11)}$$

where J_{KA} is the beam current density in kiloamps, B_{KG} is the guide field strength in kilogauss and a_{cm} is the beam half thickness in centimeters.

Perturbed Solutions

We consider perturbation of the form $f(x) \exp(st + kz)$ which are solutions to the linearized relativistic pressureless fluid equations and Maxwell equation with zero order fields given by Eqs. (T2) through (T6). Note that we take all quantities to be independent of y.

Neglecting the equilibrium v_y and the diamagnetic term in B_z, the fluid equations give

$$(s + ik)\, \tilde{v}_x = \frac{e}{m\gamma} (\tilde{E}_x - \tilde{B}_y) + \Omega\, \tilde{v}_y \tag{T12}$$

$$(s + ik)\, \tilde{v}_y = \frac{e}{m\gamma} (\tilde{E}_y + \tilde{B}_x) - \Omega\, \tilde{v}_x \tag{T13}$$

$$\tilde{v}_z = 0 \tag{T14}$$

for the perturbed velocity field $\underline{\tilde{v}} = (\tilde{v}_x, \tilde{v}_y, \tilde{v}_z)$ in terms of the perturbed fields $\tilde{E}$ and $\tilde{B}$. The Maxwell

equations for $\underline{\tilde{E}}$ and $\underline{\tilde{B}}$ are

$$\nabla \cdot \underline{\tilde{E}} = 4\pi\, \tilde{\rho} - \frac{4\pi\, ik}{s}\, \sigma\, \tilde{E}_z \qquad \nabla \cdot \tilde{B} = 0$$

$$\nabla \cdot \tilde{E} = -\, s\tilde{B} \qquad \nabla \cdot \underline{B} = s\tilde{E} + 4\pi\, \tilde{J} + 4\pi\, \sigma\, E_z\, \hat{z} \qquad \text{(T15)}$$

where

$$\tilde{J} \equiv e\, \eta_o\, \tilde{v} + e\, \eta^2\, \underline{v}, \qquad \tilde{\rho} \equiv e\, \tilde{\eta}_o$$

and we have used the continuity equation for the resistive plasma

$$s\, \rho_p + \nabla \cdot J_p = s\, \rho_p + ik\, \sigma\, \tilde{E}_z = 0 \qquad \text{(T16)}$$

We now define two functions A_+ and A_- as

$$A_\pm \equiv \left(1 + \frac{ik}{s}\right)\left(\tilde{E}_x \pm i\tilde{E}_y\right) - \frac{1}{s}\, \partial_x\, \tilde{E}_z \qquad \text{(T17)}$$

Equations (T15) then imply

$$A_+ + A_- = 2\left(1 + \frac{ik}{s}\right)\tilde{E}_x - \frac{2}{s}\, \partial_x\, \tilde{E}_z \qquad \text{(T18)}$$

$$A_+ - A_- = 2i\, \tilde{E}_y\left(1 + \frac{ik}{s}\right) \qquad \text{(T19)}$$

$$\partial_x (A_+ + A_-) = -2(s + ik)\left(1 + \frac{4\pi\sigma}{s}\right)\tilde{E}_z \qquad \text{(T20)}$$

o that if A_+ and A_- are known, $\underline{\tilde{E}}$ may be determined and $\underline{\tilde{B}}$ may then be found from the curl $\tilde{E}$ equation. Thus the solution is completely determined by A_+ and A_-.

Now using the linearized fluid equations (T12) through (T14), together with the Maxwell equation (T15), we find that $A_\pm$ must satisfy

$$A_+'' = -\left(\frac{2\pi\sigma}{s} + 1\right)\xi_+^2 A_+ - \frac{2\pi\sigma}{s}\xi_-^2 A_- \qquad \text{(T21)}$$

$$A_-'' = -\frac{2\pi\sigma}{s}\xi_+^2 A_+ - \left(\frac{2\pi\sigma}{s} + 1\right)\xi_-^2 A_- \qquad \text{(T22)}$$

where

$$\xi_\pm^2 \equiv -s^2 - k^2 - \frac{\omega_p^2 (s + ik)}{(s + ik) \pm i\Omega} \qquad \text{(T23)}$$

The solution to Eqs. (T21) and (T22) is

$$A_- = A_1 \sin q_+ x + B_1 \cos q_+ x + A_2 \sin q_- x + B_2 \cos q_- x \qquad \text{(T24)}$$

$$A_+ = - A_1 \alpha_- \sin q_+ x - B_1 \alpha_- \cos q_+ x$$

$$- A_2 \alpha_+ \sin q_- x - B_2 \alpha_+ \cos q_- x \qquad \text{(T25)}$$

where

$$2b \xi_+^2 \alpha_\pm \equiv - (b+1)(\xi_+^2 - \xi_-^2)$$

$$\pm \sqrt{(b+1)^2 (\xi_+^2 - \xi_-^2) + 4b^2 \xi_+^2 \xi_-^2} \qquad \text{(T26)}$$

$$2 q_\pm^2 \equiv (b+1)(\xi_+^2 + \xi_-^2)$$

$$\pm \sqrt{(b+1)^2 (\xi_+^2 - \xi_-^2)^2 + 4b^2 \xi_+^2 \xi_-^2} \qquad \text{(T27)}$$

$$b \equiv \frac{2\pi\sigma}{s} \qquad \text{(T28)}$$

Equations (T24) through (T28) with appropriate boundary conditions determine the solution to the linearized perturbed equations.

Dispersion Relation

We assume that the perfectly conducting waveguide is located at $x = \pm a$ so that the appropriate boundary conditions are

$$E_z = E_y = 0 \quad \text{at} \quad x = \pm a$$

which from Eqs. (T19) and (T20) gives

$$A_+ = A_- \quad \text{at} \quad x = \pm a$$

$$\partial_x (A_+ + A_0) = 0 \quad \text{at} \quad x = \pm a$$

These four conditions give four linear homogeneous equations for A_1, A_2, B_1, and B_2. Setting the determinant of the coefficients equal to zero then gives the dispersion relation which is

$$\left(\frac{\alpha_+ + 1}{\alpha_+ \quad 1} q_+ a \cot q_+ a - \frac{\alpha_- + 1}{\alpha_- - 1} q_- a \cot q_- a \right)$$

$$\times \left(\frac{\alpha_+ + 1}{\alpha_+ - 1} q_+ a \tan q_+ a - \frac{\alpha_- + 1}{\alpha_- - 1} q_- a \tan q_- a \right) = 0 \tag{T29}$$

We note that had we taken $B_1 = B_2 = 0$ initially in Eqs. (T24) and (T25) the dispersion relation would have only contained the first factor. Similarly, setting $A_1 = A_2 = 0$ gives the second factor as the dispersion relation.

Growth Rate of the Symmetric Mode

For the symmetric mode, $E_z(x) = E_z(-x)$, so that we require $B_1 = B_2 = 0$ in the solutions for $A_\pm$. We thus have for this mode the dispersion relation

$$\frac{\alpha_+ + 1}{\alpha_+ - 1} q_+ a \cot q_+ a - \frac{\alpha_- - 1}{\alpha_- - 1} q_- a \cot q_- a = 0 \qquad \text{(T30)}$$

For the lower Doppler shifted cyclotron mode we have (for low phase velocity waves, $\omega/k \ll 1$)

$$\omega \simeq k - \Omega \frac{k_+^2 \xi_-^2}{k_+^2 \xi_-^2 + \omega_p^2} \qquad \text{(T31)}$$

Writing $\omega = \omega_o + i\Gamma$ with ω_o and Γ purely real we have

$$\omega_o \simeq k - \Omega \qquad \text{(T32)}$$

$$\Gamma = - \frac{2\Omega\ \omega_p^2}{|k^2+\xi_-^2 + \omega_p^2|^2}\ \xi_{-R}\ \xi_{-I} \tag{T33}$$

when ξ_{-R} and ξ_{-I} are the real and imaginary parts of ξ_- respectively. Thus to obtain the growth rate Γ we must solve Eq. (T30) for ξ_-.

Using Eqs. (T26) through (T28) we obtain

$$\alpha_+ \simeq \frac{-\ b}{1+b\ -\ (1+b)\ \xi_+^2/\xi_-^2\ -\ 2b\xi_+/\xi_-} \tag{T34}$$

$$\frac{\alpha_- + 1}{\alpha_- - 1} \simeq 1 \tag{T35}$$

$$q_i^2 \simeq \frac{(2b+1)\ \xi_+^2\ \xi_-^2}{b(\xi_+^2 + \xi_-^2) + \xi_+^2} \tag{T36}$$

$$q_+^2 \simeq \frac{(2b+1)\ \xi_+^2}{(b+1)\ -\ b\xi_+^2/\xi_-^2} \tag{T37}$$

for $\omega << k$. The dispersion relation thus becomes (taking $a = 1$),

$$q_+ \cot q_+ = - \left(1 + \frac{4\pi\sigma}{\omega_o}\right) q_- \cot q_o \qquad \text{(T38)}$$

with

$$q_+ \approx ik \qquad \text{(T39)}$$

$$q_-^2 \approx \frac{(2b + 1)\ \xi_+^2\ \xi_-^2}{b\xi_-^2 + \xi_+^2} \qquad \text{(T40)}$$

In Eqs. (T38) through (T40) we have assumed that

$$\left|\xi_+^2/\xi_-^2\right| \ll 1 \qquad \text{(T41)}$$

Now for $\sigma = 0$ $(b = 0)$ the dispersion relation Eq. (T38) becomes

$$q_+ \cot q_+ = - q_- \cot q_- \qquad \text{(T42)}$$

and for $ik \simeq q_+$ small in modulus, this implies

$$q_-(\sigma = 0) = 2 \qquad \text{(T43)}$$

Expanding q_- about the solution (T43) of (T42) we obtain

$$q_- \simeq 2 - \alpha \frac{(4\pi\sigma)^2}{\omega_o^2 + (4\pi\sigma)^2} - i\alpha \frac{4\pi\omega_o\sigma}{\omega_o^2 + (4\pi\sigma)^2} \qquad \text{(T44)}$$

where

$$\alpha \equiv \left. \frac{q_i \cot q_i}{\cot q_- - q_- \csc^2 q_i} \right|_{\sigma=0} \simeq 0.32$$

Using Eq. (T44), Eq. (T40) may be solved for ξ_-^2 for use in evaluating the growth rate. The result is

$$\xi_-^2 \approx \frac{4(1 - 2ib)}{1 + 4b^2} \qquad \text{(T45)}$$

so that we finally obtain

$$\Gamma \simeq \frac{4\Omega\,\omega_p^2}{|k^2 + 4 + \omega_p^2|^2} \cdot \frac{4\pi\,\omega_o\sigma}{\omega_o^2 + (4\pi\sigma)^2} \qquad \text{(T46)}$$

Note that Eq. (T44) implies $|\xi_-^2| < k^2$ for $k \leq 1$ as assumed in obtaining Eqs. (T38) through (T40).

Now the second factor in Eq. (T46) maximizes at a value of 0.5 for $\omega_o \simeq 4\pi\sigma$, while for low phase velocity waves

$(\omega/k \ll 1)$ Ω is approximately equal to k so that the first factor has a maximum for $\Omega/c \sim k \sim 1.15$. We then obtain a maximum growth rate of

$$\Gamma_{max} \simeq \frac{4}{50} \frac{\omega_p^2 a^2}{c^2} \frac{c}{a} \qquad \text{(T47)}$$

when $\omega_o \sim 4\pi\sigma$ and $\Omega a/c \sim 1$. This growth rate is about 2.5 times faster than the resistive liner growth rates found in Ref. 1.

APPENDIX U

A MODEL OF ION PICKUP AND ACCELERATION BY A TRAVELLING WAVE

The design which has been formulated for the proof-of-principle experiment on Auto-Resonant acceleration contemplates a puff-gas injector section (Ref. 1), wherein the subject ions will be created by primary beam ionization of a neutral gas, then trapped or picked up by the preformed travelling cyclotron wave which is supported by the electron beam, and finally carried out of the puff-gas section into the accelerator section where the wave and ions are accelerated above the initial wave velocity. Consequently it is of interest to determine the degree of precision with which the wave amplitude and phase velocity must be controlled in order to achieve an acceptable pickup efficiency.

In addition, since the puff-gas injector section will be between the wave growth and the wave acceleration sections, it is desirable to generalize the analysis to include the possibility that the wave is still growing, or has begun accelerating, when the ions are first introduced. Such a theoretical framework would also allow the consideration of alternative design options. For example, one might envision extending the wall flare of the acceleration section back into the puff-gas section, so that an axial DC electric field would be present there to help eject the ions out into the accelerator section. Then one could conceivably grow and/or accelerate the wave as necessary to pick up the ions in the beginning of the accelerator section.

In order to address these questions, a simple one-dimensional, nonrelativistic model of the ion-wave interaction is explored. It is hypothesized that the ion equation of motion in the axial direction is

$$\ddot{z} = \frac{e}{M} E(t) \sin k \left[z - \int_0^t d\tau \, v_\phi(\tau) \right] \qquad \text{(U1)}$$

where k = axial wave number, assumed constant

e, M = ion charge, mass

$E(t)$ = amplitude of the axial wave electric field

$v_\phi(t)$ = axial wave phase velocity

and $E(t)$ and $v_\phi(t)$ are presumed to be controlled externally, independent of the behavior of the ions. One seeks the ion motion, as it evolves from prescribed initial conditions subject to the prescribed functions $E(t)$, $v_\phi(t)$.

It is convenient to make a formal transformation of variables:

$$y \equiv z - \int_0^t d\tau\, v_\phi(t) + \pi \tag{U2}$$

whence one obtains the transformed equation of motion,

$$\ddot{y} = -\frac{e}{M} E(t) \sin ky - \dot{v}_\phi(t) \tag{U3}$$

Here y may be viewed as the ion coordinate relative to the travelling wave frame of reference. One may define a Hamiltonian function

$$H(y,\dot{y},t) = \frac{1}{2}\,\dot{y}^2 - \frac{e\,E(t)}{Mk}\,\cos ky + y\,\dot{v}_\phi(t) \qquad (U4)$$

which generates the equations of motion $\partial H/\partial\dot{y} = \dot{y}$, $\partial H/\partial y = -\ddot{y}$ so that

$$\frac{d}{dt}\,H(y,\dot{y},t) = \frac{\partial H}{\partial t} = -\frac{e\,\dot{E}(t)}{Mk}\,\cos ky + y\,\ddot{v}_\phi(t) \qquad (U5)$$

Therefore, when the wave amplitude E and the wave acceleration $A = \dot{v}_\phi$ are constant in time, it follows that $\dot{H} = 0$ so that $H(y, \dot{y})$ is a constant of the motion. This allows an immediate determination of the ion trajectory.

Furthermore, when E and A are not constant, but vary only slowly in time such that $\dot{E}$ and $\ddot{v}_\phi$ are small, it is possible to define a new quantity

$$J(H,t) = \oint dy\,\dot{y}[H, y, t] \qquad (U6)$$

which is adiabatically invariant and thus serves as an approximate constant of the motion to yield the ion

trajectories. In Eq. (U6), $\dot{y}(H, y, t)$ is obtained by inverting Eq. (U4) and t held fixed while $\oint dy$ is performed--between turning points or over a wave period.

For the case where E and A are constant in time, it is instructive to examine the function

$$V(y) = -\frac{eE}{Mk} \cos ky + Ay \qquad \text{(U7)}$$

where $H(y,\dot{y}) = \frac{1}{2}\dot{y}^2 + V(y)$. This potential function $V(y)$, which is a ramp-biased sinusoid, is depicted in Figure U1. It has relative maxima a bit to the right of odd multiples of π, and relative minima a bit to the left of even multiples of π. When E and A are constant, $H = \frac{1}{2}\dot{y}^2 + V(y)$ is a constant of the motion, so that a particle trajectory is characterized by a horizontal line on Figure U1 with the ordinate H. The particle motion is confined to that region of y-space where $H \geq V(y)$, with turning points y_T where $V(y_T) = H$. Given the initial conditions $(y, \dot{y})$ after which E, A are constant, the subsequent motion may be inferred immediately from inspection of H, V on Figure U1.

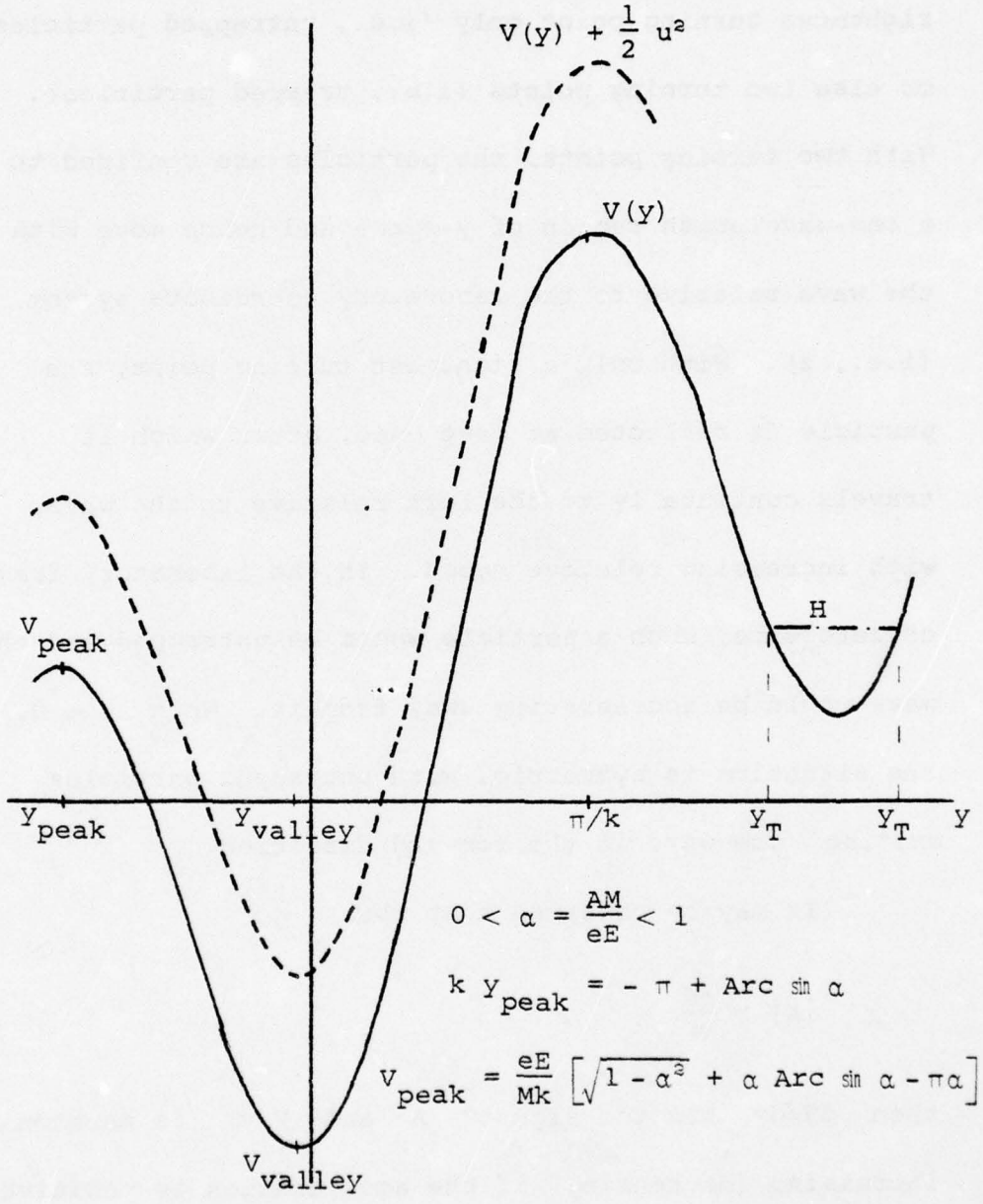

Figure U1. Potential Function of Accelerating Wave

When $A > 0$, all trajectories will have either a rightmost turning point only (i.e., untrapped particles) or else two turning points (i.e., trapped particles). With two turning points, the particles are confined to a one-wavelength region of y-space and hence move with the wave relative to the laboratory coordinate system (i.e., z). With only a rightmost turning point, the particle is reflected at most once, after which it travels continually to the left relative to the wave, with increasing relative speed. In the laboratory frame of reference, such a particle would be untrapped and the wave would be accelerating away from it. When $A < 0$, the situation is symmetric, with untrapped particles exiting the wave in the forward direction.

It may be observed that when

$$|A| > \frac{eE}{M} \tag{U8}$$

then dV/dy has the sign of A and $V(y)$ is monotonic increasing (decreasing) if the acceleration is positive (negative). In this case, there exist no particles trapped in the wave.

When $0 < A < eE/M$, so that the wave is forward accelerating at a moderate rate, the extrema of $V(y)$ occur at

$$ky_{peak} = -\pi + \text{Arc sin } (AM/eE) \tag{U9}$$

$$ky_{valley} = -\text{Arc sin } (AM/eE) \tag{U10}$$

(modulo 2π)

and those particles initially located in the range

$$y_{peak} \leq y_o \leq y_{peak} + 2\pi/k \tag{U11}$$

will be trapped for which

$$H(y_o, \dot{y}_o) \leq V(y_{peak}) = \frac{1}{k}\left[\sqrt{\left(\frac{eE}{M}\right)^2 - A^2} - A\left(\pi - \text{Arc sin } \frac{AM}{eE}\right)\right] \tag{U12}$$

It is instructive to consider the following series of problems, which provide some insight as to the properties of wave amplitude and acceleration which are commensurate with a high ion pickup efficiency:

(a) Initial conditions--particles are distributed uniformly in z; $|\dot{y}| = |\dot{z} - v_\phi| = u$ for all particles;

dynamics--the field amplitude is grown suddenly from 0 to E, while $\dot{v}_\phi = A = 0$.

(b) Initial conditions--same as for problem (a);

dynamics--the field amplitude is grown slowly (adiabatically) from 0 to E, while $\dot{v}_\phi = A = 0$.

(c) Initial conditions--same as for problem (a);

dynamics--same as for problem (a), followed by wave acceleration at $\dot{v}_\phi = A$, while E = constant.

(d) Initial conditions--same as final conditions of problem (b);

dynamics--the wave is accelerated at $\dot{v}_\phi = A$, while E = constant.

Problem (a)

This problem has been considered previously (Ref. 1, p. 308) in computing the pickup efficiency of a wave

travelling at constant amplitude through the puff gas section. The sudden approximation, which requires

$$\frac{2\pi}{ku}\ \frac{\dot{E}(t)}{E(t)} >> 1 \qquad \text{(U13)}$$

is appropriate since the wave is initially written at the fast electron velocity, and is at full strength when an ion is first born to see it.

For the initial conditions of this problem, the particle Hamiltonian is

$$H = \frac{1}{2}\, u^2 + V(y_o) \qquad \text{(U14)}$$

which is a curve shifted upward from $V(y_o)$ by $\frac{1}{2}\, u^2$, as indicated in Figure U1. For this problem, there is the additional simplification that $A = 0$ so that $V(y)$ is not ramp-biased.

Inserting Eq. (U14) into Eq. (U12) allows calculation of the initial coordinates of trapped particles, and for particles in the range (U11), those are trapped for which

$$k\,|y_{o\ \text{trapped}}| < 2\,\text{Arc}\cos\sqrt{\frac{kMu^2}{4eE}} \qquad \text{(U15)}$$

so that the pickup efficiency is

$$\epsilon_{pickup} = \frac{2}{\pi} \text{Arc } \cos \sqrt{\frac{kMu^2}{4eE}} \qquad \text{(U16)}$$

For this sudden growth problem, there will always be some untrapped particles near $y_o = \pm \pi/k$, so $\epsilon_{pickup} < 1$. However, the larger the field amplitude, the larger the pickup efficiency. Marginal pickup (i.e., $\epsilon_{pickup} \geq 0$) occurs for

$$\frac{1}{2} u^2 \leq 2 \frac{eE}{Mk} = V(y_{peak}) - V(y_{valley}) \qquad \text{(U17)}$$

and there is no pickup at all for smaller values of E/u^2 which violate Eq. (U17)

Problem (b)

This problem has also been considered previously (Ref. 8). The adiabatic invariant is found to be

---

9. See for example, J. R. Thompson, Phys. Fluids 14, 1532 (1971).

$$J(H,t) = J(\varkappa,t) = \frac{4}{\pi}\sqrt{\frac{eE(t)}{Mk}}\left\{\varkappa E_2(\varkappa^{-1})\ S(\varkappa - 1)\right.$$

$$\left. + \left[E_2(\varkappa) - (1-\varkappa^2)K(\varkappa)\right]S(1-\varkappa)\right\} \tag{U18}$$

where

$$\varkappa \equiv \sqrt{\frac{1}{2}\left(1 + \frac{H}{eE(t)/Mk}\right)}$$

K, E_2 = complete elliptic integrals of the first, second kind

$S(x) = \frac{1}{2} + \frac{1}{2}$ sign (x) = unit step function

and

$$\frac{2\pi}{ku}\ \frac{\dot{E}(t)}{E(t)} \ll 1 \tag{U19}$$

is required to validate the assumption of adiabaticity. Since J is an adiabatic invariant for all particles, and they all have the same value of $H = \frac{1}{2}u^2$ initially, it follows that all particles will have the same

$H(t)$ [and $\varkappa(t)$] at future times. If the amplitude growth is halted when $E(t) = E$, with the acceleration A remaining zero, the final value of H or $\varkappa$ may be determined from the J-invariance equation,

$$J(H,t) = J(\varkappa,t) = J_{initial} = u \tag{U20}$$

From Figure U1 with $\dot{v}_\phi = A = 0$, or from Eq. (U4) one may note that marginal trapping occurs for

$$\varkappa \simeq 1$$

$$H \simeq \frac{eE}{Mk} \tag{U21}$$

Particles remain untrapped for larger values of $\varkappa$, H, and the particle trajectories in $(y,\dot{y})$ phase space-determined from Eq. (U4) with H = constant are unbounded in y. Likewise, for $-(eE/Mk) < H < (eE/Mk)$ or $0 < \varkappa < 1$, the particles are trapped and their trajectories are closed bounded contours in phase space. From Eqs. (U18), (U20) and (U21), one finds that marginal trapping occurs when

$$\frac{eE}{Mk} \approx \frac{\pi^2}{16} u^2 \qquad \text{(U22)}$$

and the pickup efficiency is

$$\epsilon_{pickup} = S\left[\frac{eE}{Mk\,u^2} - \frac{\pi^2}{16}\right] \qquad \text{(U23)}$$

The pickup efficiencies of Eqs. (U16) and (U23) are plotted in Figure U2 to illustrate the difference between sudden and adiabatic growth in the field amplitude required for pickup.

Problem (c)

The analysis of this problem can proceed exactly as for problem (a), except for the minor complication that $A \neq 0$. Equation (U14) again describes the initial conditions for $H(y_o)$, with $V(y_o)$ given by Eq. (U7) and illustrated on Figure U1. Condition (U12) defines which particles will be trapped in the accelerating wave, and it has the simple graphical interpretation of selecting those particles for which the $H(y_o)$ contour falls below

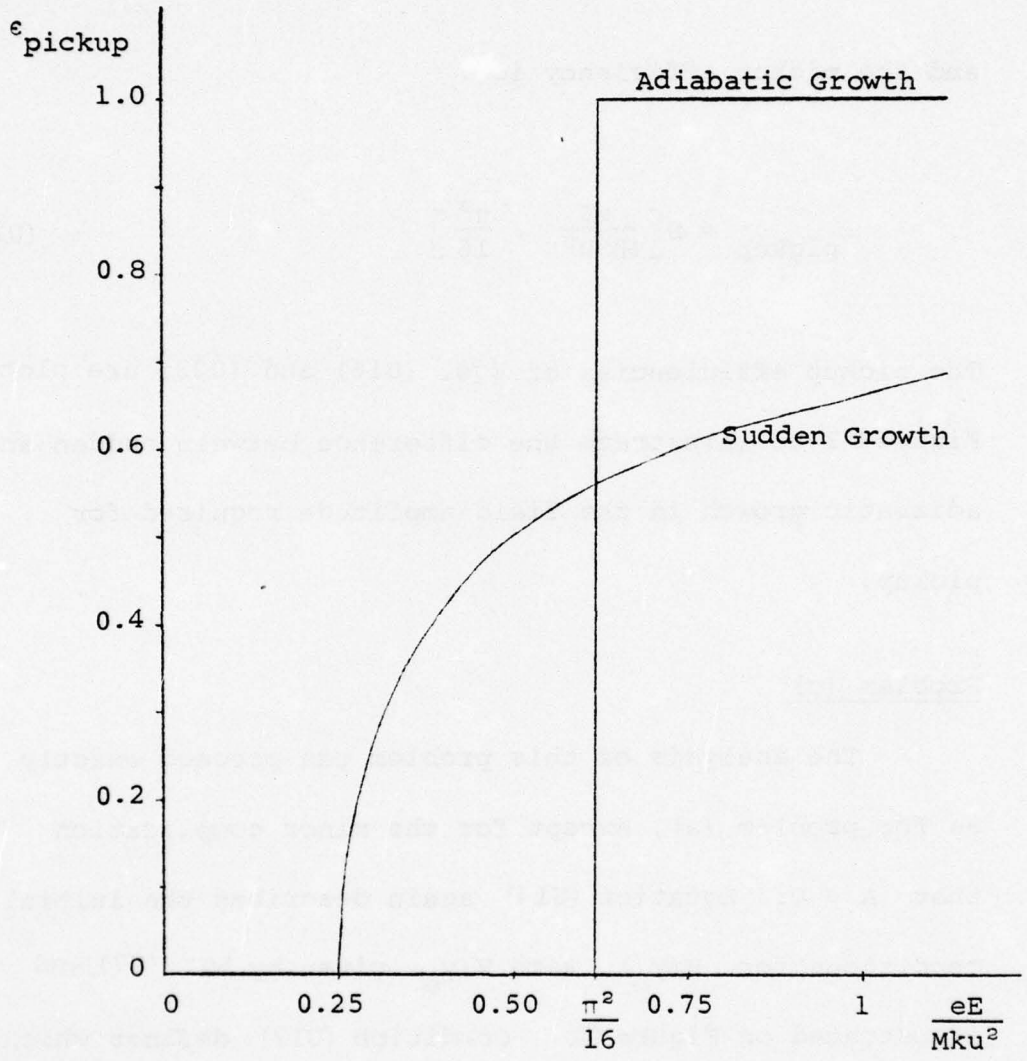

Figure U2. Pickup Efficiency in a Nonaccelerating Wave

the leftmost peak of $V(y_o)$ which occurs at $y_o = y_{peak}$, given by Eq. (U9). Without loss of generality, consideration may be restricted to the coordinate range Eq. (U11), since the trapping condition (U12) will be unaltered for any other wavelength range.

Condition (U17) of problem (a) for marginal pickup has the following obvious geometrical generalization when $A \neq 0$:

$$\frac{1}{2} u^2 \leq V_{peak} - V_{valley} = \frac{2eE}{Mk} G\left(\frac{AM}{eE}\right) \tag{U24}$$

where

$$G(\alpha) = \sqrt{1 - \alpha^2} + \alpha \operatorname{Arc\,sin} \alpha - \frac{\pi}{2} \alpha \tag{U25}$$

and the equality in Eq. (U24) implies $\varepsilon_{pickup} \approx 0$ while the inequality in Eq. (U24) is necessary for $\varepsilon_{pickup} > 0$. Since $G(\alpha)$ falls from 1 to 0 as $\alpha = AM/eE$ increases from 0 to 1, it is obvious that larger accelerations reduce the allowable speed of particles that may be picked up with a given wave amplitude, and condition (U8) continues to be necessary for any pickup whatever.

Furthermore, since $G < 1$, Eq. (U24) is more difficult to satisfy than Eq. (U17). This means that if no particles are trapped prior to wave acceleration, none can be trapped afterward without additional growth in the wave amplitude. That is, if the particles are initially travelling faster than the wave, and the wave is slowly accelerated to a higher velocity than the particles start with, then no particles can be picked up by the wave--no matter how slowly the acceleration is accomplished. .The wave will accelerate right through the mean particle speed without picking up any particles.

Given that condition (U24) is satisfied, then the trapped particle coordinates may again be determined by inserting Eq. (U14) into Eq. (U12) to obtain

$$\alpha\, ky - \cos ky = \sqrt{1-\alpha^2} + \alpha \operatorname{Arc}\sin \alpha - \pi\alpha - \frac{Mku^2}{2eE} \tag{U26}$$

where $\alpha = AM/eE$. Equation (U26) will have two solutions for y, which we designate y_{min} and y_{max}, where $y_{peak} < y_{min} < y_{valley}$ and $y_{valley} < y_{max} < y_{peak} + \frac{2\pi}{k}$.

Those particles initially in the range Eq. (U11) will be trapped for which $y_{min} \leq y_{o\ trapped} \leq y_{max}$, so that the pickup efficiency is given by

$$\epsilon_{pickup} = \frac{k(y_{max} - y_{min})}{2\pi} \tag{U27}$$

As in problem (a), because of the sudded growth in amplitude, there will always be some untrapped particles near $y_o \geq y_{peak}$ no matter how large eE/Mku^2 is, although the number of such untrapped particles approaches zero as eE/Mku^2 increases. In addition, because of the finite wave acceleration, there will always be some untrapped particles near $y_o \leq y_{peak}$ $\left(\text{equivalently } y_o \leq y_{peak} + \frac{2\pi}{k} \text{ in range (U11)}\right)$, and the number of these untrapped particles remains finite even when Mku^2/eE approaches zero. One may show that the limiting fraction of untrapped particles obeys

$$\alpha(2\pi - 2\pi\ \epsilon_{lost} + \sin 2\pi\ \epsilon_{lost}) = 2\sqrt{1 - \alpha^2}\ \sin^2 \pi\ \epsilon_{lost} \tag{U28}$$

whose bounding solutions are

AD-A033 946 AUSTIN RESEARCH ASSOCIATES INC TEX F/G 20/7
CONCEPTUAL DESIGN OF AN AUTO-RESONANT ACCELERATOR EXPERIMENT.(U)
NOV 76 W E DRUMMOND, G I BOURIANOFF F29601-76-C-0046
UNCLASSIFIED ARA-224 AFWL-TR-76-152 NL

4 OF 4
AD A033946

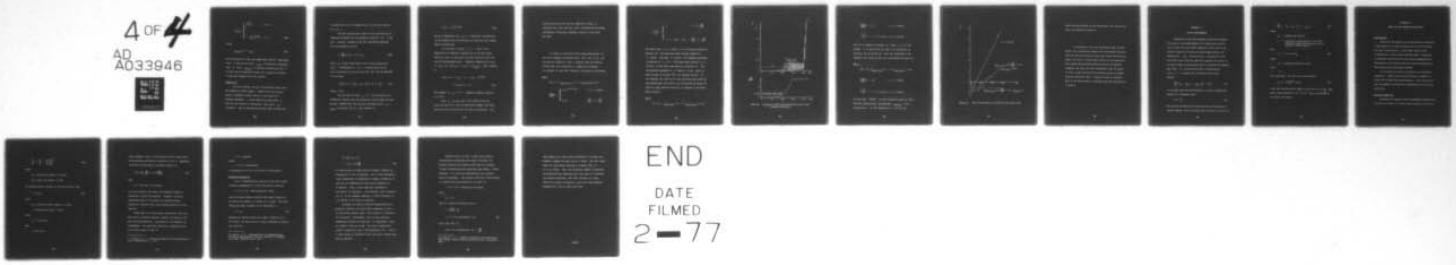

END

DATE FILMED 2-77

$$\epsilon_{lost} \simeq \begin{cases} \sqrt{\alpha/\pi} & , \quad \alpha \ll 1 \\ 1 - \frac{3}{2\pi}\sqrt{1-\alpha^2} & , \quad \alpha \simeq 1 \end{cases} \tag{U29}$$

where

$$\epsilon_{pickup} \leq 1 - \epsilon_{lost} \tag{U30}$$

and the equality in Eq. (U30) applies when Mku^2/eE approaches zero. It may be seen that ϵ_{lost} is monotonic increasing with α, while ϵ_{pickup} is monotonic decreasing with α, so that wave acceleration always has a negative influence on particle trapping for this problem.

Problem (d)

For this problem, the wave acceleration begins when the adiabatic growth ceases. Suppose that this initial phase of adiabatic growth results in the particle's trapping parameter $\varkappa$ being reduced to some value $\varkappa_o$ when the wave growth is terminated. This value $\varkappa_o = \varkappa_o(eE/Mku^2)$ may be determined from Eqs. (U18) and (U20), and

the particles will be trapped prior to wave acceleration if $\varkappa_o < 1$.

The wave acceleration phase of this problem may be examined as before via the potential function $V(y)$ in Eq. (U7). However, instead of Eq. (U14), the initial conditions for this problem are that

$$H = \frac{eE}{Mk}\left(2\,\varkappa_o^2 - 1\right) + A\,y_o \qquad \text{(U31)}$$

which is a linear ramp rather than a curve paralleling $V(y_o)$. Furthermore, if $\varkappa_o < 1$ the particles do not exist throughout the entire range Eq. (J11), but are restricted to the range

$$-\frac{1}{k}\,\text{Arc}\cos\left(1 - 2\varkappa_o^2\right) < y_o < \frac{1}{k}\,\text{Arc}\cos\left(1 - 2\varkappa_o^2\right) \qquad \text{(U32)}$$

modulo $2\pi/k$.

For the case in which $\varkappa_o > 1$, the possibility of subsequent trapping may be examined by inserting Eq. (U31) into Eq. (U12). However, even for the most favorable point $y_o = y_{peak}$, one finds that Eq. (U12) reduces to

$$2\,\kappa_o^2 - 1 \overset{?}{\leq} \sqrt{1-\alpha^2} \qquad \text{(U33)}$$

which is impossible for $\kappa_o > 1$. Therefore, no particles can be trapped after acceleration if they were not trapped before acceleration.

For the case in which $\kappa_o < 1$, there is the possibility of complete trapping due to the restricted range Eq. (U32) of particles confined initially below the lip of the potential wells. Complete trapping will occur if $H[y_o = k^{-1}\ \text{Arc}\cos(1 - 2\,\kappa_o^2)\,] < V(y_{peak})$, which reduces to

$$\alpha\ \text{Arc}\cos(1 - 2\,\kappa_o^2) - (1 - 2\,\kappa_o^2) \leq \sqrt{1-\alpha^2}$$

$$+\ \alpha\ \text{Arc}\sin\alpha - \pi\alpha \qquad \text{(U34)}$$

For example, if $\kappa_o \simeq 2^{-1/2}$, complete trapping requires $\alpha \leq 0.217$.

When κ_o is less than 1 but greater yhan the value for which Eq. (U34) is marginally obeyed, then some particles will be spilled by the wave acceleration. The

pickup efficiency may then be computed as before by inserting Eq. (U31) into Eq. (U12), and solving for the initial coordinates of marginal trapping, subject to the range Eq. (U32).

In order to illustrate these ideas graphically, as well as to examine situations where $\dot{E}(t)$ and $\dot{v}_\phi(t)$ are arbitrarily varying in time, a computer code was written to solve Eq. (U1) numerically. Examples of problems (a) through (d) have been computed, including the following:

Run 1

$$@\ t = 0,\quad \dot{z}_{particles} = 0;\ 0 < Z_{particles} < 2\pi/k$$

$$\frac{eE(t)}{Mku^2} = \begin{cases} 0.01\ e^{0.04\ kut} & ,\ 0 < t < 146/ku \\ 3.438 & ,\ \frac{146}{ku} < t < \frac{300}{ku} \end{cases}$$

$$\frac{v_\phi(t)}{u} = \begin{cases} 1 & , \quad 0 < t < \dfrac{200}{ku} \\ 1 + 0.7\,(kut - 200) & , \quad \dfrac{200}{ku} < t < \dfrac{300}{ku} \end{cases}$$

The phase from $0 < t < 146/ku$ is the adiabatic growth of problem (b). The particles first become trapped at $t \approx 103/ku$, and when $t = 146/ku$, the trapping parameter is reduced to $\varkappa \simeq 2^{-1/2}$. The phase from $(200/ku) < t < (300/ku)$ is the wave acceleration of problem (d). The acceleration parameter is $\alpha = MA/eE \simeq 0.204$, which is small enough to satisfy (U34) for complete pickup. In the computer run, each of 20 test particles was picked up and accelerated; the results are illustrated in Figure U3, where the mean particle velocity is compared to the wave phase velocity.

Run 2

$$@\ t = 0, \quad \dot{z}_{particles} = 0; \quad 0 < z_{particles} < 2\pi/k$$

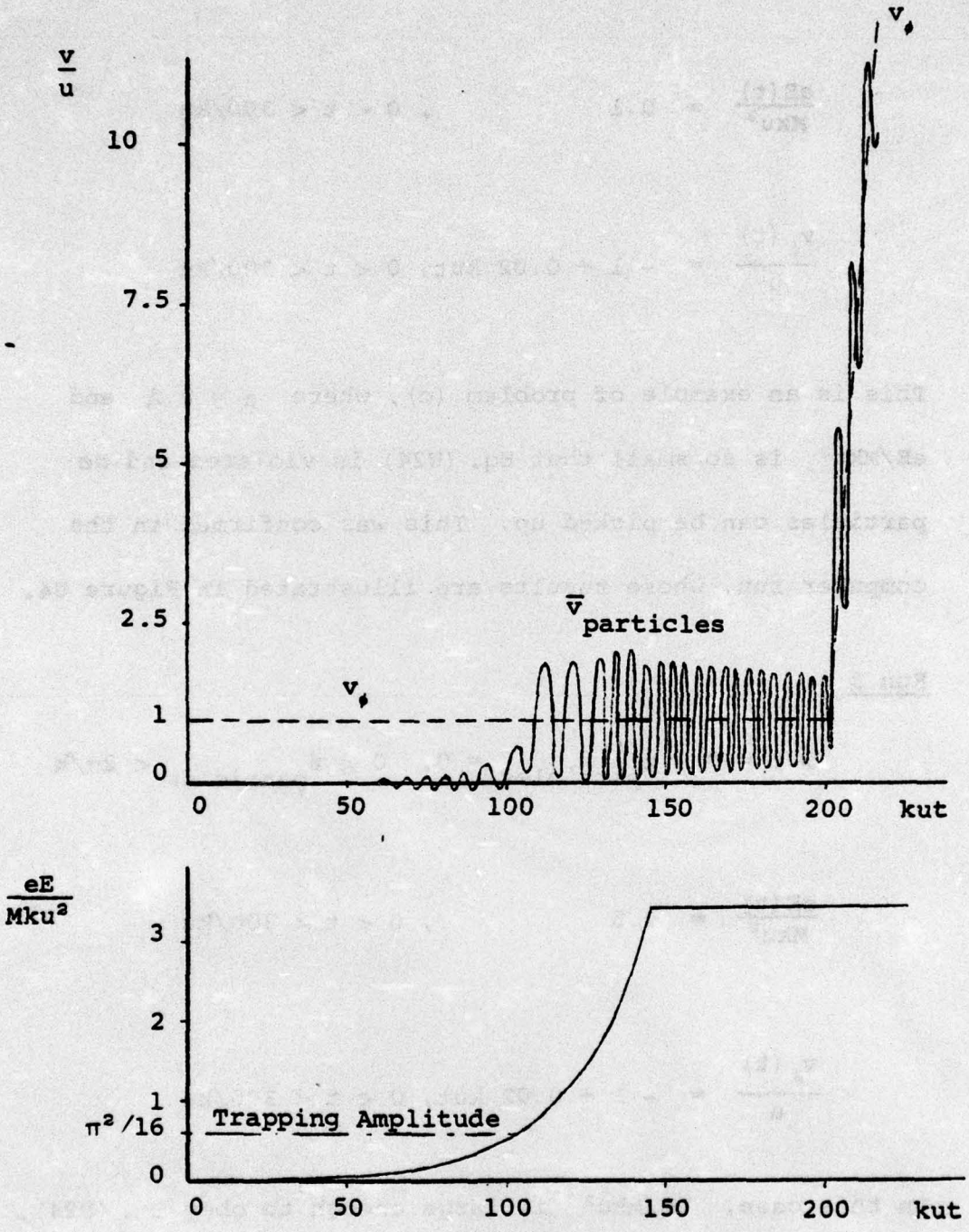

Figure U3. Adiabatic Growth and Acceleration with 100% Trapping Efficiency

$$\frac{eE(t)}{Mku^2} = 0.1 \qquad , 0 < t < 300/ku$$

$$\frac{v_\phi(t)}{u} = -1 + 0.02\ kut, \quad 0 < t < 300/ku$$

This is an example of problem (c), where $\alpha = 0.2$, and eE/Mku^2 is so small that Eq. (U24) is violated and no particles can be picked up. This was confirmed in the computer run, whose results are illustrated in Figure U4.

Run 3

$$@\ t = 0, \quad \dot{z}_{particles} = 0, \quad 0 < z_{particles} < 2\pi/k$$

$$\frac{eE(t)}{Mku^2} = 0.5 \qquad , 0 < t < 300/ku$$

$$\frac{v_\phi(t)}{u} = -1 + 0.02\ kut, \quad 0 < t < 300/ku$$

In this case, eE/Mku^2 is large enough to obey Eq. (U24). From Eqs. (U26) and (U27), one finds that $\epsilon_{pickup} \simeq 0.46$ theoretically. In the computer run, 9 of 20 test

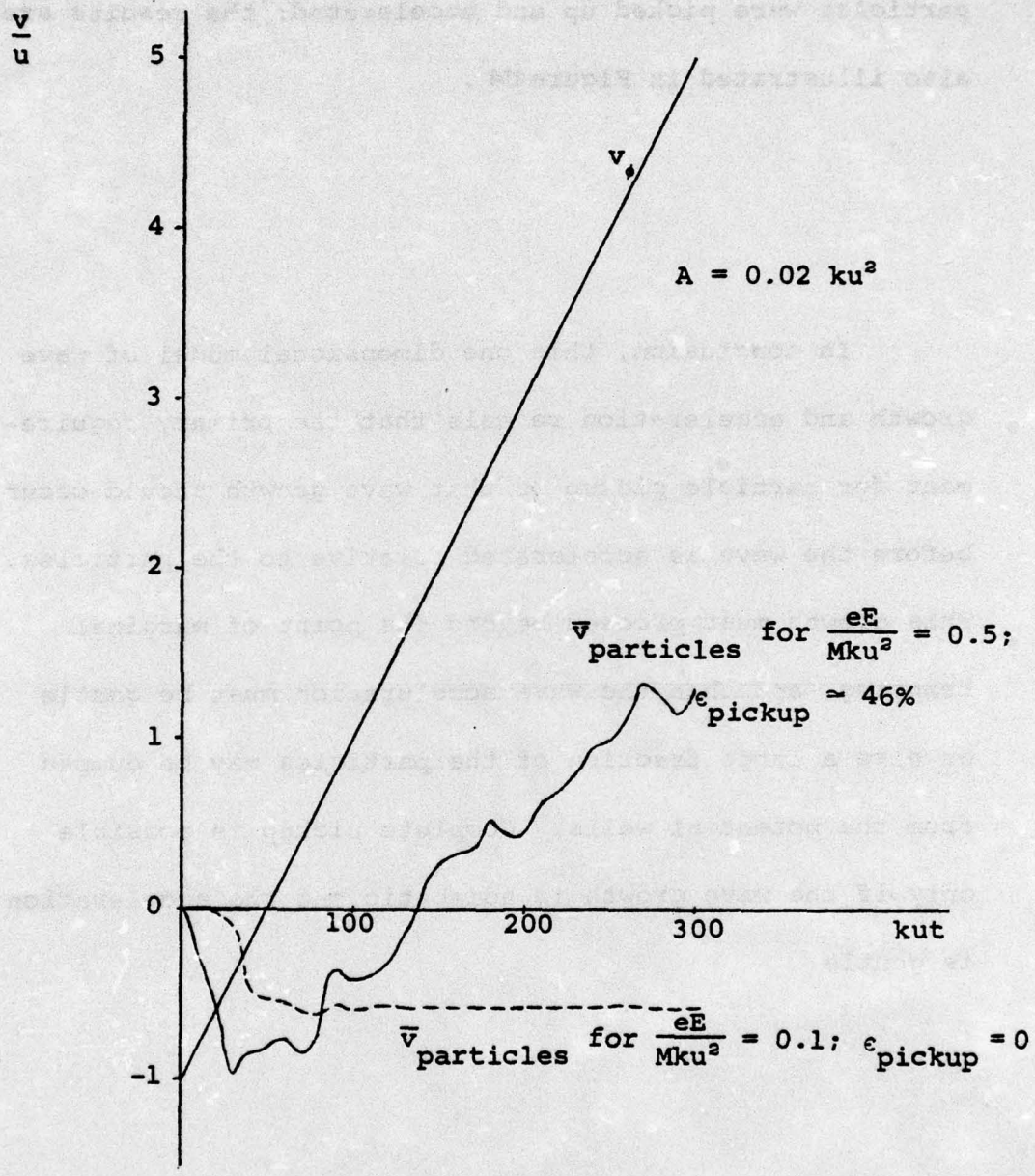

Figure U4. Wave Acceleration at Constant Field Amplitude

particles were picked up and accelerated; the results are also illustrated in Figure U4 .

In conclusion, this one dimensional model of wave growth and acceleration reveals that the primary requirement for particle pickup is that wave growth should occur before the wave is accelerated relative to the particles. This growth must proceed beyond the point of marginal trapping, and then the wave acceleration must be gentle or else a large fraction of the particles may be dumped from the potential wells. Complete pickup is possible only if the wave growth is adiabatic and the acceleration is gentle.

APPENDIX V

VACUUM REQUIREMENTS

Operation of the Auto-Resonant Accelerator depends initially on the establishment of a rigid rotor equilibrium in which the net radial expansion forces due to the electron beams self-fields and centrifugal effects are balanced by a $v_\theta B_z$ restoring term. Derivation of the self-field force term has generally assumed that there is no space charge neutralization due to ionization of ambient gas atoms. If a uniform fractional neutralization, $n_+/n_b = f$, is assumed then self-field force term becomes

$$\frac{|e|}{m_o}(E_r - v_z B_\theta) \simeq \omega_{po}^2 \left(\frac{1}{\gamma^2} - f\right)\frac{r}{2} \qquad (V1)$$

It is clear that for neutralization to be an unimportant effect it is necessary that

$$f \ll \frac{1}{\gamma^2} \qquad (V2)$$

The rate of neutralization build-up due to ionization of neutral ambient ions by primary beam electrons is given by

$$\frac{df}{dt} = (n_a - n_+)\,\sigma\, v_z \simeq n_a\,\sigma\, c \qquad \text{(V3)}$$

where

n_a = ambient gas density

σ = ionization cross-section $\simeq 10^{-18}\,cm^2$ (assuming oxygen and nitrogen are the dominant atomic species).

Also

$$n_a \simeq 3.5 \times 10^{16} P_a \qquad \text{(V4)}$$

where

P_a = ambient pressure in torr.

Using

$\gamma \simeq 7$

then using Eqs. (V2) and (V4) there obtains

$$P_a \ll \frac{2 \times 10^{-5}}{t}\ (\text{torr}) \qquad \text{(V5)}$$

Since the electron pulse length is 200 nsec (0.2 μsec) long, then a base pressure of 10^{-6} to 10^{-5} torr is adequate in the drift tube region.

APPENDIX W

BEAM DUMP AND RADIATION SHIELDING

Introduction

There are two aspects to be considered in designing a beam dump for 3.0 MeV electrons and/or 30 MeV protons. The first consideration is beam dump survival when irradiated by a high fluence electron beam. The second is personnel shielding from high energy bremsstrahlung generated by the electron beam and neutrons generated by the collectively accelerated protons.

In this section these two aspects are considered separately. Based upon survival criteria, graphite is chosen as the best beam dump material. This choice also has the benefit of minimizing bremsstrahlung and neutron production.

Material Selection

Assuming the electron beam is expanded adiabatically, the ratio of final to initial current density is given by

$$\frac{J_f}{J_i} = \frac{B_i}{B_f} \simeq \left(\frac{E_i}{E_f}\right)^{1/2} \qquad \text{(W1)}$$

where

E_i = initial ion energy $\simeq$ 0.25 MeV

E_f = final ion energy = 30 MeV

The energy fluence incident on the beam stop is then

$$\varphi = J_f E_e \tau \qquad \text{(W2)}$$

where

E_e = electron kinetic energy = 3.0 MeV

τ = beam pulse length $\simeq$ 300 ns

Since

$J_i \simeq 9.55$ kA/cm^2

then

$\varphi \simeq 785$ J/cm^2

Using Spencers (Ref. 9) calculation for the energy deposition profile produced by electrons in low Z materials, the ratio of peak dose to incident fluence is

$$D/\varphi = \frac{1}{E_o} \frac{dE}{dx} J \simeq 0.9 \frac{J/gm}{J/cm^2} \qquad (W3)$$

Then

$$D \simeq 712 \text{ J/gm} = 170 \text{ cal/gm}$$

For most elements this amount of deposited energy is sufficient to melt the material. Further, the short deposition time of the energy will produce thermo-mechanical stresses which could produce spalling of the material.

Based upon its low Gruneisen coefficient and high dose level to produce melting, graphite is chosen as the best beam dump material. Specifically, ATJ graphite is recommended. The thickness required to completely stop the electron beam is (Ref. 9)

---

9 . Spencer, L. B., "Energy Dissipation by Fast Electrons," N.B.S. Monograph No. 1, 1959.

$t \simeq 1.7$ gms/cm^2

Using

$\rho = 2.0$ ($\pm$ 10%) gms/cm^3

a thickness of 0.85 cm (0.354 inch) is sufficient.

Radiation Production

The 0° bremsstrahlung radiation yield from a gold convertor bombarded by 3.0 MeV electrons is (Ref.10)

$Y = 2.5 \times 10^4$ Rads/coulomb @ 1 meter

Since the yield scales linearly with atomic charge (Z), the value for carbon is a factor of 13 lower. The total charge per pulse incident on the beam dump is

$$Q = I_o \tau \qquad \text{(W4)}$$

Assuming the machine fires once every 5 minutes (Δt = 1/12 hour), the dose rate at 1 meter (assuming no shielding) would be

---

10, Martin, T. H., "Determination of Bremsstrahlung Production Efficiencies from Data Obtained on PHERMEX at 27 MeV," AFWL TR 73-65, 1973.

$$\dot{D} = \frac{1}{13} Y I_o \tau/\Delta t$$

$$\simeq 2.25 \times 10^6 \frac{mR}{Hr} \qquad (W5)$$

To reduce this to a safe level of roughly 2 mR/Hr, an attenuation of 10^5 is required. For 3.0 MeV bremsstrahlung, attenuation is dominated by Compton scattering so that for all materials the 10th value thickness is 60 gms/cm^2. Thus, a total material thickness of 300 gms/cm^2 is required. Since concrete, with a density of 2.4, is the cheapest approach, a total thickness of 1.25 meters ($\approx$ 49 inch) is required.

Although the angular yield of bremsstrahlung is primarily forward, the large angle component is still 1 to 10% of the forward yield. Thus nearly 4π shielding is called for. Fortunately, this is only required immediately around the beam dump. It represents a cube of roughly 8 feet on a side. The floor loading produced is roughly 8.3 psi (1,200 pounds/sq. ft.). Use of a steel pallet to distribute this load over a larger area may be required.

Assuming that a 30 amp, 30 MeV proton beam is collectively accelerated once every 5 minutes, the protons striking the graphite beam stop will undergo nuclear interactions which generate high energy (> 1 MeV) neutrons. To a very good approximation the neutron yield is isotropic. The neutron yield for 30 MeV protons on graphite has been measured to be (Ref. 11)

$$Y \sim 4\pi \times 10^{10} \text{ neutrons}/\mu C \text{ of protons}$$

Since

$$Q \sim 6\ \mu C$$

then at 1 meter the neutron flux is

$$\varphi = \frac{YQ}{4\pi R^2} \frac{1}{\Delta t}$$

$$\simeq 7 \times 10^7 \text{ neutrons/cm}^2 \cdot \text{Hr} \qquad \text{(W6)}$$

Given that (Ref. 11)

$$2.88 \times 10^4 \text{ neutrons/cm}^2 \cdot \text{Hr} = 1 \frac{\text{mR}}{\text{Hr}}$$

---

11. Burrill, E. A., "Neutron Production and Protection," HVEC Report, High Voltage Engineering Corp., Burlington, Mass.

then roughly four 10th value thicknesses of concrete are needed to reduce the dose rate to 2 mR/Hr. The 10th value layer for high energy neutrons is roughly (Ref. 11) 10 to 12 inches. Thus, the shielding needed to attenuate the bremsstrahlung generated will also serve to attenuate the neutrons produced. Note that concrete is a good choice for neutron attenuation, since the radio-isotopes created have a fairly short half-life.